Light Emission and Ultrafast Carrier Dynamics in III-V Semiconductors from First Principles

Thesis by
Vatsal A Jhalani

In Partial Fulfillment of the Requirements for the
Degree of
Doctor of Philosophy

Caltech

CALIFORNIA INSTITUTE OF TECHNOLOGY
Pasadena, California

2019
Defended May 31, 2019

ACKNOWLEDGEMENTS

I feel quite fortunate to be able to say that my graduate experience at Caltech has been the best chapter of my life so far, and I would like to acknowledge the people without whom this would not be the case.

First and foremost, I want to thank Marco Bernardi for being a wonderful advisor. Being his first student has truly been a pleasure and a privilege. I am grateful for the diverse knowledge in the areas of materials science and physics that he has shared with me, for his advice on all matters that concern a Ph.D. student, no matter how large or small, and for his unwavering attention to detail, which has made me a better scientist and more confident communicator.

I would like to thank the Resnick Institute for Sustainability, Heidi Rusina, and especially director Neil Fromer for not only providing me with fellowship support to freely conduct research, but also for giving invaluable mentorship, advice, and guidance. I want to thank my collaborators in Italy, including Davide Sangalli for indispensible discussion, and Maurizia Palummo for the pleasure of a very fruitful collaboration and summer visit to the group in University of Rome − a period of time that is a highlight of my graduate career. I want to thank I-Te Lu, who has been my always patient office-mate and conference roommate since we both first started our Ph.D. journey, Jin-Jian Zhou, an incredibly hardworking post-doc from whom I have learned so much, Hsiao-Yi Chen for fruitful collaboration, and the other members of the Bernardi group. I want to thank Caltech Reslife, including Deans Nye and Green, Felicia Hunt, Vanessa Tejada, as well as the members of Ricketts Hovse, for making my tenure as an undergraduate RA at Caltech a pleasurable and enriching experience. The Caltech Applied Physics and Materials Science department and the campus community at large has been a warm and welcoming place since I step foot on campus, and that is more than partially due to Christy Jenstad and Jennifer Blankenship, who work tirelessly to ensure our needs our met and the atmosphere is pleasant.

I want to thank my friends at Caltech, in Los Angeles, and elsewhere for their support, and whose company is one of the reasons this experience was

so enriching. I am incredibly grateful for the people I met, the friendships I grew, and the memories I made during my time here. Lastly, I want to thank my family. I especially want to thank my mom Alpana, and my sister Kopal, for being my biggest fans and for their absolutely unconditional support and love, without which I would not have reached where I have.

ABSTRACT

The III-V semiconductors are a broad class of technologically important materials which have seen immense research interest in academia and industry due to their electronic, optoelectronic, and photovoltaic properties. In particular, GaN and the III-nitride family of wide bandgap semiconductors have emerged as promising candidates for the next generation of high-efficiency power electronics and light-emitting devices. Their device operation and macroscopic properties are governed by the dynamics of charge carriers and their microscopic scattering processes. Near room temperature, the carriers are scattered by lattice vibrations (phonons) at ultrafast timescales of order fs−ps. Microscopic understanding of carrier dynamics is challenging due to both the ultrafast time scale at play and to the presence of defects, interfaces, and impurities affecting transport and spectroscopy measurements. Typical theoretical treatments of carrier dynamics and light emission employ empirical models to interpret and fit experimental results. Over the last few years, so-called first-principles (or "*ab initio*") methods to accurately compute ultrafast carrier dynamics, transport, and light emission have seen a rapid rise. These approaches do not employ parameters from experiments, and using only the structure of the material as input, together with quantum mechanics and condensed matter theory, are enabling accurate predictions of carrier dynamics in a wide range of materials and are shedding light on microscopic details such as which electronic states, phonon modes and dissipative processes are responsible for the observed charge transport and light emission properties.

Here, we present first-principles calculations of different aspects of ultrafast carrier dynamics and light emission in III-V semiconductors of technological relevance, focusing on GaN, a key material for solid-state light emission technology. We first present a study of the ultrafast nonequilibrium dynamics of excited (so-called "hot") carriers in GaN, with a focus on electron-phonon scattering and the nanometer scale transport of carriers in GaN light emitting devices (LEDs). Using cutting-edge first-principles methods developed in this work, we find an asymmetry between the time scale of hot electron and hole thermalization which provides a possible explanation on a major open problem in the efficiency and energy losses of GaN LEDs. We then develop

and apply a new rigorous first-principles approach for computing light emission and the radiative recombination lifetimes in bulk crystals, nanomaterials and isolated systems. Our approach is based on the Bethe-Salpeter equation (BSE), and it accurately includes excitons, namely electron-hole states bound by the Coulomb interaction that play a key role in light-matter interactions. Using this method, we carry out benchmark calculations of radiative lifetimes in GaAs and GaN. In GaN, our computed radiative lifetimes are in excellent agreement with experiment (within a factor of two), and our calculations further highlight the importance of including excitonic effects and spin-orbit coupling to obtain accurate radiative. We also employ a model to account for exciton thermal dissociation at high temperature, finding excellent agreement with spectroscopic measurements. Lastly, we discuss ongoing work on computing the intrinsic (phonon-limited) mobility in bulk GaN from first principles, focusing on efforts to include piezoelectric electron-phonon interactions, which are important for acoustic phonon modes in GaN. We compute the electron and hole mobilities in GaN and obtain excellent agreement with experiment. Our calculations shed light on which phonon modes scatter the carriers, providing new microscopic insight into charge carrier dynamics in GaN and related III-V semiconductors.

PUBLISHED CONTENT AND CONTRIBUTIONS

[1]V. A. Jhalani, J.-J. Zhou, and M. Bernardi, "Intrinsic carrier mobilities in GaN from first principles", *In Preparation.*,
V.A.J. contributed to conceiving the project and desiging the research, carried out the calculations, and analyzed the data and wrote the manuscript together with the co-authors.

[2]H.-Y. Chen, V. A. Jhalani, M. Palummo, and M. Bernardi, "Ab initio calculations of exciton radiative lifetimes in bulk crystals, nanostructures and molecules", *Submitted.* arXiv preprint arXiv:1901.08747 (2019),
V.A.J. carried out the calculations and contributed to writing the manuscript.

[3]V. A. Jhalani, H.-Y. Chen, M. Palummo, and M. Bernardi, "First-principles exciton radiative lifetimes in bulk GaN", *Submitted.* (2019),
V.A.J. participated in the conception and design of the research, contributed to developing code, carried out the calculations, and wrote the manuscript.

[4]V. A. Jhalani, J.-J. Zhou, and M. Bernardi, "Ultrafast hot carrier dynamics in GaN and its impact on the efficiency droop", Nano Lett. **17**, 5012–5019 (2017), DOI: 10.1021/acs.nanolett.7b02212.
V.A.J. contributed to conceiving the project, contributed to developing the code, carried out the calculations, analyzed the data, and wrote the manuscript together with the co-authors.

TABLE OF CONTENTS

LIST OF ILLUSTRATIONS

Chapter 1

INTRODUCTION

1.1 III-V and III-Nitride Semiconductor Materials and Devices

The last few decades have seen a rising global need for the development and commercialization of technologies which can convert and harness energy efficiently. The looming crisis of depleting fossil fuel resources, the necessity of reducing greenhouse gas emissions to combat climate change, and the fierce economic incentive for reducing costs have been a driving engine for innovation in renewable energy and related materials technology. Over the course of the last few decades, binary compound semiconductors composed of a group III and group V element, also known as III-V semiconductors, have seen intense research interest both in academia and in industry due to their broad and versatile electronic and optical properties. The III-V semiconductors are at the basis of technologies with profound societal impact, including the laser, solid-state lighting, and efficient solar cells. While this class of compounds encompasses a broad range of materials, much of the work has focused on a more restricted family of III-V semiconductors, including GaAs, GaP, and InP, among others. It was not until recently that the III-nitride semiconductors (GaN, InN, AlN) have become the subject of intense research. In particular, GaN and its alloys (e.g., $Ga_xAl_{1-x}N$ and $Ga_xIn_{1-x}N$) exhibit a wide direct band gap that can be tuned by alloying from sub-visible to UV energies. The III-nitrides also posses strong chemical bonds and high melting tempertures which makes them well suited for high temperature operation and high power electronics and optoelectronics [1].

Consequently, GaN and other III-nitride materials are prime candidates for next-generation optoelectronic and energy devices. GaN appears as a strong candidate to replace Si in wide band gap power electronics for use in smart electric grids which can efficiently convert and transmit solar and wind power, and for motor drives in future clean electric vehicles [2, 3]. Most notably, GaN has emerged as one of the key materials for efficient solid-state light emitting technology following the invention of GaN-based blue and green light-emitting diodes (LED) in 1995 [4], whose scientific and technological merits were rec-

ognized with the 2014 Nobel Prize for Physics.

The reason for this recognition is not hard to see. Before GaN, the only available high-luminosity LEDs available emitted in the red part of the visible spectrum. The advent of GaN-based ultraviolet, blue, and green emitters allows, in conjunction with phosphors to down-convert light to red and yellow, for generation of light with a wide range of wavelengths. Semiconductors able to generate light with a broad spectrum are highly desirable for efficiently producing white light [5]. White-light sources based on LEDs have yet to realize their full potential for positively impacting energy consumption, the environment, and the health of individuals. In year 2009, roughly twenty two percent of the energy generated by the United States was used for lighting applications [5]. It is estimated that if all conventional white-light sources were converted to the more energy-efficient LED technology, energy consumption could be reduced by approximately 1 petawatt-hour per year. This amount of energy is equivalent to roughly 230 500-MW coal power plants, which collectively generate 200 million tons of greenhouse gas emissions and can potentially save $\sim$ \$100B annually [6]. This estimate does not even take into account the health benefits and impacts of numerous other applications of LED technology considered outside of conventional lighting, such as in displays, agriculture, automotive lighting, and many more. Needless to say, there is massive interest in improving the cost-efficiency of LEDs, as widespread utilization of the technology has large potential positive impact.

1.2   GaN LEDs and their Charge Carrier Dynamics

At its core, the operation of an LED is quite simple. Generation of light in a semiconducting material like GaN is possible by injecting electrons into the conduction band of the material and providing unfilled electronic states (so-called "holes") in the lower-energy valence band; the electrons can lose energy by filling the hole states, producing a photon with energy corresponding to the energy gap between the valence and conduction states, which is roughly 3.45 eV in GaN, corresponding to the near ultraviolet. An LED consists of three stacked layers of materials. The bottom and top layers provide, respectively, a high concentration of electrons and holes. An example of top and bottom layers are n-type GaN doped with Si and and a p-type GaN doped

with Mg. These materials sandwich an active layer consisting of alternating larger and smaller band gap materials (such as GaN and InGaN, respectively) with a nanometer scale thickness, creating a series of quantum wells that spatially trap electrons and holes, allowing them to recombine and produce light. This electron-hole recombination in small volumes of a semiconductor is much more efficient than conventional light emission in an incandescent light bulb, which relies on black body radiation from heating [5–7]. A schematic of an LED device structure and the basis of its operation is shown in Fig. 1.1 in the middle and right panels. Multiple factors affect the efficiency and thus ultimately the cost of an LED, such as conversion efficiency of phosphors, internal reflection of photons at interfaces of materials with air, and degradation over time from generated heat. However, the consensus is that the key figure of merit is the quantum efficiency (QE) of the device, defined as the number of photons produced per electron-hole pair injected. A significant portion of LED research in academia and industry is aimed at improving the QE by ensuring that more electrons and holes become trapped in the quantum wells, and that a greater fraction of those recombinations are radiative, namely that light (as opposed to heat) is emitted as a result of the electron-hole recombination [5, 6].

Macroscopic properties such as the QE of an LED are intimately tied to the dynamics of the charge carriers (electrons and holes) in the active layer semiconductor and the microscopic processes that govern them. As such, gaining a complete understanding of these processes is crucial from a device design perspective. Material properties and parameters essential to device performance and efficiency, such as quantities describing carrier transport and recombination, in bulk GaN are not completely understood. Furthermore, there are critically important open problems in device design, which have their origins in carrier dynamics. One such mystery is the LED efficiency droop, the phenomenon in which the QE appears to decrease when operating the LED at higher currents [8]. Efficiency droop is a major roadblock for solid-state lighting because high operating currents are key to lowering the initial price barrier [6]. However, the microscopic origin of efficiency droop, among other open problems, are under debated [8, 9].

Microscopic understanding of carrier dynamics is challenging to obtain because carrier dynamics are regulated by ultrafast carrier scattering processes
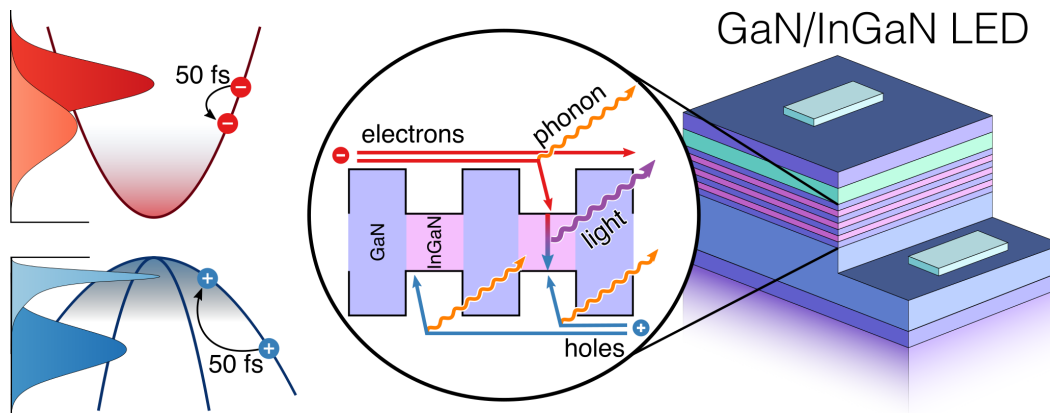
Figure 1.1: **Schematic of carrier dynamics in a GaN-based LED. Left:** Schematic GaN bandstructure and ultrafast relaxation of hot electrons and holes via electron-phonon scattering. **Middle:** Schematic band diagram of an LED active layer quantum well structure and carrier dynamics within, where the vertical dimension represents energy, and horizontal represents spatial coordinate along the active layer. The shaded regions represent the band gaps of the alternating materials. Electrons and holes enter the active region, lose excess energy via scattering with phonons, become spatially confined, and then recombine to produce light. **Right:** Schematic of an LED device. Reproduced with permission from Ref. [7].

that occur over femtosecond to picosecond timescales [10]. These processes include scattering with phonons, impurities, interfaces, and other carriers, and govern properties such as the carrier mobility, relaxation times, and mean free paths [11–13]. In particular, the electron-phonon (e-ph) interaction, namely the coupling between carriers and atomic lattice vibrations, plays a dominant role on transport near room temperature in relatively pure materials [13, 14]. It is also the dominant mechanism regulating the rate of energy loss (or "cooling") of excited carriers within a few eV of the band edges, a scenario of relevance for carriers injected at LED heterojunctions. The excited (so-called "hot") carriers rapidly lose their excess energy with respect to the band edges at a rate on the order of femtoseconds, dissipating heat by phonon emission through e-ph coupling, as shown in the left and middle panels of Fig. 1.1.

Once relaxed to the band edges, the carriers recombine to emit light, a process that occurs over longer timescales of pico- to nanoseconds [12]. Prior to recombination, carriers form electron-hole pairs bound by the screened Coulomb interaction. These bound electron-hole pairs are known as excitons, which can

be seen as neutral quasiparticale excitations with their own wavefunctions and energy spectrum distinct from those of the electron and hole. Excitons are key in the radiative processes of a semiconductor, which can be seen as exciton recombination events resulting in photon emission [15]. The radiative processes compete with non-radiative recombination channels, such as defect-induced recombination and Auger scattering, which are a source of energy inefficiency in LED devices as they result in heat generation [12, 16, 17].

Experimentally determining intrinsic properties and parameters of ultrafast dynamics can be challenging. For example, there is a wide range of ultrafast spectroscopy techniques, and their results in GaN samples prepared in different laboratories exhibit a wide range of values. The time scale of hot electron cooling has been measured by several authors without a clear consensus, while the difficulty of growing high quality p-doped samples of GaN has limited measurements of hot hole cooling times (see Chapter 2). Similarly, the intrinsic rate of exciton radiative recombination can be investigated with a range of techniques. Transient photoluminescence (PL) is perhaps the most widely used method to measure radiative lifetimes, but the apparent decay rate of the PL can be the result of multiple competing processes, including exciton trapping at defects and exciton-phonon scattering, rather than an intrinsic exciton recombination rate. Excitons can also dissociate at high temperature, making the observed time-dependent PL signal even more challenging to interpret [16] (see Chapter 4).

Typical theoretical treatments for predicting carrier dynamics and light emission employ empirical models to interpret and qualitatively reproduce experimental observations. Among other limitations, they make assumptions on the nature of certain interaction, and neglect others altogether. For example, in polar materials like III-V and III-nitride semiconductors, empirical models for the e-ph interaction assume the polar longitudinal optical phonon mode dominates the phonon scattering processes [18], neglecting the contribution of other modes in carrier relaxation. Similarly, theoretical approaches for radiative recombination, especially in bulk materials, treat electrons and holes as independent, without taking into account the Coulomb interaction between them and the formation of excitons [12, 19].

1.3 First-Principles Computational Methods

To overcome the limitations of experiment and empirical theoretical treatments, a substantial field has formed focused on the application and development of computational techniques to compute materials properties starting from first principles, or "*ab initio*". These methods employ quantum mechanics and use only the material's atomic crystal structure as input. The resulting calculations are free of fitted parameters, but typically require substantial computational resources, specialized codes and numerical technique, and a steep learning curve. Powerful methods for computing ultrafast dynamics and light emission in materials from first principles have been developed in the last few years. Much of the work in the Bernardi group is focused on the development, advancement, and application of these techniques. There are countless resources introducing the first-principles methods employed in this work and a detailed discussion is beyond the scope of this thesis. We will breifly outline some of the methods used in this work and provide resources for further reading. The relevant computational details will be discussed in connection with each result presented in the following chapters.

First-principles calculations are typically rooted in the formalism known as density functional theory (DFT), in which Schrodinger's equation is recast in terms of a functional of a single quantity, the charge density, to compute ground-state properties of a many-body system. In Kohn-Sham (KS) DFT, the intractable many-electron Schrodinger equation is replaced with a more practical set of independent particle equations where all many-body effects are contained in the exchange-correlation functional, which is not known exactly but for which approximations can be constructed. A variety of widely used "flavors" of DFT, or approximate exchange-correlation functionals, are available, and a choice must be made balancing accuracy and computational cost. The calculations in this work employ either the local density approximation (LDA) or the general gradient approximation (GGA). By self-consistently solving the system of independent particle equations and minimizing the KS energy with respect to the density, one can obtain ground state properties such as equilibrium crystal structure, mechanical properties, and most notably the ground state single-particle approximate electronic wavefunctions and band structure. Further information on DFT theory and its technical and practical aspects can be found in Refs. [20–23].

Lattice dynamical properties, including the latice vibrations (and their quanta, the phonons) can be obtained using density functional perturbation theory (DFPT), via the linear response of the DFT energy with respect to lattice perturbations [24]. When implemented in the plane-wave pseudopotential method, DFPT offers many advantages over other methods (such as finite-displacement) for computing phonons in crystalline solids, including calculation of phonon perturbation potentials (the effect of the phonon on the crystal lattice potential seen by electrons) and phonon energies and eigenvectors at arbitrary wavevector in the Brillouin zone using just a single unit cell of the material in the calculation. The perturbation potentials from DFPT can be combined with the electronic wavefunctions from DFT to obtain e-ph matrix elements encoding the coupling of different electronic states due to phonons [13, 25].

The e-ph matrix elements form the basic building blocks for calculating a host of many-body phenomena, including phonon and electron self-energies, temperature renormalization of the electronic bandstructure, and carrier lifetimes. Carrier e-ph scattering rates can then obtained within the framework of many-body perturbation theory as the imaginary part of the lowest order electron self-energy, which is equivalent to Fermi's golden rule [13, 14]. The carrier scattering rates and e-ph coupling elements can be used within the framework of the Boltzmann transport equation (BTE), a semiclassical approach for computing the flow of electron and phonon occupations in phase space. The BTE in its most general form is a complicated set of partial differential equations coupling electron and phonon dynamics. However, with certain approximations and simplifications, it can be made numerically tractable to obtain transport properties from first principles, such as carrier mobilities and real-time dynamics of excited carriers, as is done in this work [13, 14]. As we discuss in the following chapters, while tractable, these calculations are challenging and computationally expensive as they require advanced interpolation and Brillouin zone sampling techniques to efficiently integrate up to 10^9 e-ph coupling elements.

To obtain first-principles excited state properties such as optical spectra and excitonic states, one must go beyond the ground-state formalism of DFT.

While different options exist depending on the nature of the system, for solid-state materials the GW-Bethe-Salpeter equation (GW-BSE) framework is widely employed [26, 27]. The GW method is a practical approach for computing the electron self-energy within many-body perturbation theory from the one-particle Green's function [14]. In this work, it is mainly used to correct the DFT exchange-correlation interactions and obtain accurate electronic band-structures. For optical properties and electron-hole excitations, techniques beyond the one-particle Green's function are needed. Starting from the two-body Green's function one can construct a two-particle BSE Hamiltonian that includes electron-hole interactions, and solve the resulting eigenvalue problem in the electron-hole transition basis. This approach provides accurate exciton wavefunctions and energies. One limitation is that fully diagonalizing the BSE Hamiltonian can be an extremely challenging computational task, as the size of the matrix depends on the number of electron-hole transition pairs at each sampled **k**-point in reciprocal space. Iterative methods that avoid full matrix diagonalization are much faster and can be used to obtain accurate optical spectra without explicitly computing the exciton wavefunctions [28]. Radiative properties such as exciton radiative recombination lifetimes can be computed using Fermi's golden rule, however these do require the exciton wave-functions [29]. While less challenging for lower-dimensional (0D, 1D, and 2D) systems in which fewer **k**-points are needed to sample the Brillouin zone, fully solving the BSE for bulk III-V semiconductors, requires sampling transitions on fine **k**-point grids near the direct gap in the three-dimensional reciprocal space, resulting in very large BSE matrices.

1.4 Thesis Outline

The research presented in this thesis focuses on investigating ultrafast carrier dynamics and light emission using first principles computational methods in GaN and related III-V semiconductors.

Chapter 2 discusses a study of ultrafast hot carrier dynamics in GaN from first principles, with a focus on e-ph scattering and the cooling and nanoscale dynamics of hot carriers. We find that e-ph scattering is significantly faster for holes compared to electrons, and that for hot carriers with an initial $0.5 - 1$ eV excess energy, holes take a significantly shorter time (~ 0.1 ps) to relax to the

band edge compared to electrons, which take ~ 1 ps. The asymmetry in the hot carrier dynamics is shown to originate from the valence band degeneracy, the heavier effective mass of holes compared to electrons, and the details of the coupling to different phonon modes in the valence and conduction bands. We show that the slow cooling of hot electrons and their long ballistic mean free paths (over 3 nm) are a possible cause of efficiency droop in GaN light emitting diodes. Taken together, the work sheds light on the ultrafast dynamics of hot carriers in GaN and the nanoscale origin of efficiency droop. Details on the cutting-edge computational methods employed to investigate e-ph scattering and dynamics are discussed in the Methods section (Section 2.6). These include adding a long-range correction to the e-ph interactions to account for longitudinal optical modes in polar materials, and an implementation of a numerical real-time solver for the BTE to simulate electron dynamics.

Chapters 3 and 4 focus on method development and calculation of exciton radiative recombination and light emission in bulk III-V semiconductors. Light absorption (including excitonic effects) has been studied extensively using first-principles calculations, but methods for computing radiative recombination and light emission are still under development, and a rigorous approach for excitonic radiative recombination in bulk materials has not existed until now. In Chapter 3 we show a unified first-principles approach for computing exciton radiative recombination based on the BSE method in materials ranging from bulk crystals to nanostructures and molecules. We derive the rate of exciton radiative recombination in bulk crystals, isolated systems, and in one- and two-dimensional materials, using Fermi's golden rule within the BSE approach, including thermal and dimensionality effects. We present benchmark calculations of radiative lifetimes in a GaAs crystal. Our work provides a general method for studying exciton recombination and light emission in bulk, nanostructured and molecular materials from first principles.

In Chapter 4 the BSE-based formalism presented in the previous chapter is extended to anisotropic bulk materials and applied to GaN for the first time. We present first principles calculations of radiative lifetimes in bulk GaN as a function of temperature, and obtain results in very good agreement with experiment. We discuss the importance of including spin-orbit coupling and excitonic effects for obtaining accurate intrinsic radiative lifetimes in GaN. We

also discuss a model for accounting for thermal exciton dissociation, and compare its results to temperature-dependent spectroscopic measurements. Combined with the work presented in Chapter 3, our results provide an approach for computing exciton dynamics and radiative properties in bulk anisotropic materials, including key materials for LED technology such as the wurtzite III-nitrides.

In Chapter 5, we return to e-ph scattering and carrier transport and discuss ongoing work on computing the carrier mobility in bulk GaN from first principles. Using a combination of the BTE within the relaxation-time approximation and first-principles temperature- and state-dependent scattering rates, we compute mobilities for temperatures between 200-500 K for both electrons and holes. We compare our in-plane mobilities with previous Hall mobility experiments and find very good agreement. However, we focus on the proper inclusion of piezoelectric e-ph interactions in the interpolation of the e-ph coupling elements, a technical challenge that has not yet been tackled but that is of prime importance for studying charge transport in piezoelectric materials, such as GaN. Ongoing efforts to include the piezoelectric interactions and improve the related interpolation of the e-ph matrix elements are discussed..

References

[1]P. Ruterana, M. Albrecht, and J. Neugebauer, *Nitride semiconductors: handbook on materials and devices* (John Wiley & Sons, 2003).

[2]H. Okumura, "A roadmap for future wide bandgap semiconductor power electronics", MRS Bull. **40**, 439–444 (2015).

[3]S. Dimitrijev, J. Han, H. A. Moghadam, and A. Aminbeidokhti, "Power-switching applications beyond silicon: status and future prospects of SiC and GaN devices", MRS Bull. **40**, 399–405 (2015).

[4]S. Nakamura, M. Senoh, N. Iwasa, and S.-i. Nagahama, "High-brightness ingan blue, green and yellow light-emitting diodes with quantum well structures", Jpn. J. Appl. Phys. **34**, L797 (1995).

[5]S. Pimputkar, J. S. Speck, S. P. DenBaars, and S. Nakamura, "Prospects for LED lighting", Nat. Photon. **3**, 180–182 (2009).

[6]M. R. Krames, O. B. Shchekin, R. Mueller-Mach, G. O. Mueller, L. Zhou, G. Harbers, and M. G. Craford, "Status and future of high-power light-emitting diodes for solid-state lighting", J. Disp. Technol. **3**, 160–175 (2007).

[7]V. A. Jhalani, J.-J. Zhou, and M. Bernardi, "Ultrafast hot carrier dynamics in GaN and its impact on the efficiency droop", Nano Lett. **17**, 5012–5019 (2017),

[8]G. Verzellesi, D. Saguatti, M. Meneghini, F. Bertazzi, M. Goano, G. Meneghesso, and E. Zanoni, "Efficiency droop in InGaN/GaN blue light-emitting diodes: Physical mechanisms and remedies", J. Appl. Phys. **114**, 071101 (2013).

[9]J. Zhang, D. Zhang, D. Ye, C. Xu, and M. Huang, "Efficiency droop in III-nitride LEDs", in *Optoelectronics - materials and devices*, edited by S. L. Pyshkin and J. Ballato (Intech, 2015).

[10]M. Bernardi and J. C. Grossman, "Computer calculations across time and length scales in photovoltaic solar cells", Energ. Environ. Sci. **9**, 2197–2218 (2016).

[11]J. M. Ziman, *Electrons and phonons: the theory of transport phenomena in solids* (Oxford university press, 1960).

[12]B. K. Ridley, *Quantum processes in semiconductors* (Oxford University Press, 2013).

[13]M. Bernardi, "First-principles dynamics of electrons and phonons", Eur. Phys. J. B **89**, 239 (2016).

[14]G. D. Mahan, *Condensed matter in a nutshell* (Princeton University Press, 2010).

[15]R. S. Knox, *Theory of excitons (solid state phys. suppl. 5)*, Vol. 5 (Academic, 1963).

[16]J. P. Wolfe, "Thermodynamics of excitons in semiconductors", Phys. Today **35**, 46–54 (1982).

[17]E. Kioupakis, Q. Yan, D. Steiauf, and C. G. Van de Walle, "Temperature and carrier-density dependence of auger and radiative recombination in nitride optoelectronic devices", New J. Phys. **15**, 125006 (2013).

[18]H. Fröhlich, "Electrons in lattice fields", Adv. Phys. **3**, 325–361 (1954).

[19]P. T. Landsberg, *Recombination in semiconductors* (Cambridge University Press, 1992).

[20]J. P. Perdew, "Climbing the ladder of density functional approximations", MRS Bull. **38**, 743–750 (2013).

[21]A. E. Mattsson, P. A. Schultz, M. P. Desjarlais, T. R. Mattsson, and K. Leung, "Designing meaningful density functional theory calculations in materials science—a primer", Model. Simul. Mater. Sc. **13**, R1–R31 (2004).

[22]F. Giustino, *Materials modelling using density functional theory: properties and predictions* (Oxford University Press, 2014).

[23]R. M. Martin, *Electronic structrure: basic theory and practial methods* (Cambridge University Press, 2008).

[24]S. Baroni, S. de Gironcoli, A. Dal Corso, and P. Giannozzi, "Phonons and related crystal properties from density-functional perturbation theory", Rev. Mod. Phys. **73**, 515–562 (2001).

[25]F. Giustino, "Electron-phonon interactions from first principles", Rev. Mod. Phys. **89**, 015003 (2017).

[26]R. M. Martin, L. Reining, and D. M. Ceperley, *Interacting electrons* (Cambridge University Press, 2016).

[27]M. Rohlfing and S. G. Louie, "Electron-hole excitations and optical spectra from first principles", Phys. Rev. B **62**, 4927–4944 (2000).

[28]A. Marini, C. Hogan, M. Grüning, and D. Varsano, "Yambo: an ab initio tool for excited state calculations", Comput. Phys. Commun. **180**, 1392–1403 (2009).

[29]C. D. Spataru, S. Ismail-Beigi, R. B. Capaz, and S. G. Louie, "Theory and ab initio calculation of radiative lifetime of excitons in semiconducting carbon nanotubes", Phys. Rev. Lett. **95**, 247402 (2005).

Chapter 2

ULTRAFAST HOT CARRIER DYNAMICS IN GALLIUM NITRIDE AND THE IMPACT ON LED EFFICIENCY DROOP

The content of this chapter is taken from the following published work:

[1]V. A. Jhalani, J.-J. Zhou, and M. Bernardi, "Ultrafast hot carrier dynamics in GaN and its impact on the efficiency droop", Nano Lett. **17**, 5012–5019 (2017).

2.1 Introduction

As we established above, wurtzite GaN has emerged as a promising material whose technological benefits are driving intense research in industry and academia. Yet, material properties essential for device performance and energy efficiency are not completely understood in GaN and remain the subject of debate. Carrier transport and ultrafast dynamics are regulated by a range of scattering processes; among these the electron-phonon (e-ph) interactions [1, 2] play a dominant role on transport and dynamics near room temperature in relatively pure materials. Furthemore, it also regulates the energy loss (or "cooling") of excited carriers injected at heterojunctions, a scenario of relevance in GaN light emitting diodes. Hot carriers (HCs) are also central in degradation and current leakage in GaN transistors for power electronics [3, 4], and set the operational basis for hot electron transistors [5].

Microscopic understanding of HC dynamics is challenging in GaN since experimental results are modulated by defects and interfaces, and are typically interpreted with empirical models [6–12]. For example, hot electron cooling times measured by different groups range over two orders of magnitude [6, 8–13], and reports of hot hole dynamics are scarce [7]. Previous first-principles calculations on GaN have focused on Auger recombination [14, 15] and its role as a possible cause of efficiency droop, though other mechanisms have been proposed [16], including HC effects and electron leakage. These processes have seen less extensive theoretical treatment compared to Auger recombination, leaving simplified models to guide device design.

Prior to this work, we developed first-principles calculations of carrier dynamics [2] that can obtain carrier mobility [17, 18], ultrafast dynamics [19–22], HC relaxation times [19, 20] and ballistic mean free paths [19, 21] in excellent agreement with experiment. These approaches are free of empirical parameters and use the structure of the material as the only input. In particular, we recently developed a method [18] to accurately compute the e-ph relaxation times (RTs), namely the average time between e-ph collisions, in polar materials, as is needed for GaN. These approaches are extended in this work to investigate HC dynamics in GaN from first principles.

Here, we compute the e-ph RTs over a wide energy range, and study the cooling of HCs by numerically solving the time-dependent electron Boltzmann transport equation (BTE). Both the RTs and the simulated ultrafast dynamics reveal a large asymmetry between the hot electron and hole dynamics, with hot holes relaxing to the band edges significantly faster than hot electrons. The origin of this asymmetry, the role of different phonon modes and the limitations and failure of phenomenological models are analyzed in detail. We additionally find significantly longer mean free paths (MFPs) for electrons compared to holes, with implications for GaN devices. We show that the slow cooling rate of hot electrons can lead to inefficient light emission at high current, thus demonstrating that the nanoscale dynamics of HCs play a key role in LED efficiency droop.

2.2 Electron-Phonon Scattering in GaN

In polar materials like GaN, empirical models typically assume that polar optical phonons − and in particular, the longitudinal optical (LO) mode in GaN − dominate carrier scattering due to their long-range interactions with carriers. The empirical Fröhlich model [23] for the LO mode predicts an e-ph coupling matrix element $g_F(q) = i/q[(e^2 \hbar \omega_0 \epsilon_{\mathrm{ph}}^{-1})/(2V)]^{1/2}$, where V is the volume, q is the magnitude of the phonon wavevector $\mathbf{q}$, $\hbar \omega_0$ the LO phonon energy, and $\epsilon_{\mathrm{ph}}^{-1} = \epsilon_\infty^{-1} - \epsilon_0^{-1}$ the phonon contribution to the dielectric screening, with ϵ_∞ and ϵ_0 the high- and low-frequency dielectric constants, respectively. The intra-valley e-ph scattering rate $\Gamma_\mathbf{k}$ (where $\mathbf{k}$ is the electron crystal momentum) due to the empirical Fröhlich coupling g_F can be obtained analytically

for carriers in a spherical parabolic band with effective mass m^* and energy $E_{\mathbf{k}} = \hbar^2 k^2 / 2m^*$ [1, 24]:

$$\Gamma_{\mathbf{k}} = \tau_0^{-1} \left(\frac{E_{\mathbf{k}}}{\hbar \omega_0} \right)^{-\frac{1}{2}} \left[N_0 \sinh^{-1} \left(\frac{E_{\mathbf{k}}}{\hbar \omega_0} \right)^{\frac{1}{2}} + (N_0 + 1) \sinh^{-1} \left(\frac{E_{\mathbf{k}}}{\hbar \omega_0} - 1 \right)^{\frac{1}{2}} \right] \quad (2.1)$$

where N_0 is the Bose-Einstein occupation factor for LO phonons and $\tau_0^{-1} = \epsilon_p^{-1}[(e^2 \omega_0)/(2\pi \hbar)] \cdot [m^*/(2\hbar \omega_0)]^{1/2}$ is the inverse Fröhlich time. In this work, the rate in Eq. 2.1 is used to compare the widely employed Fröhlich empirical model with our first-principles results.

Following an approach we recently developed [18], we combine density functional theory (DFT) [25], density functional perturbation theory (DFPT) [26] and *ab initio* Fröhlich [27] calculations to compute the short- and long-range contributions to the e-ph coupling matrix elements, which are then interpolated on fine Brillouin zone (BZ) grids to converge the e-ph scattering rates $\Gamma_{n\mathbf{k}}$ for each electronic band n and crystal momentum $\mathbf{k}$ (see Computational Methods, Section 2.6). For the polar LO mode scattering, our *ab initio* Fröhlich calculations [27] differ in important ways from the empirical Fröhlich model as they include Born effective charges and anisotropic dielectric tensors, both computed with DFPT, and account for the electronic bandstructure and phonon dispersions (see Section 2.6). Here and in the following, the carrier excess energies are defined as the energy above the conduction band minimum (CBM) for the electrons, and the energy below the valence band maximum (VBM) for the holes.

The scattering rates and their inverse, the e-ph RTs $\tau_{n\mathbf{k}} = \Gamma_{n\mathbf{k}}^{-1}$, contain rich microscopic information on the carrier dynamics. The bandstructure near the band edges, a schematic for which is given for reference in the inset of Fig. 2.1A, crucially determines the e-ph scattering rates. While the conduction band exhibits a single parabolic valley at Γ, the valence band edge consists of a light-hole and two heavy-hole bands with anisotropic effective masses and degeneracy along the $\Gamma - A$ direction. Fig. 2.1A shows our computed e-ph scattering rates of electrons and holes with energies within 5 eV of the band edges. Both the total scattering rate contributed by all phonons and the LO mode contribution alone are shown; the empirical Fröhlich rate of Eq. 2.1, computed using parameters from the literature [28, 29], is also given for comparison. The
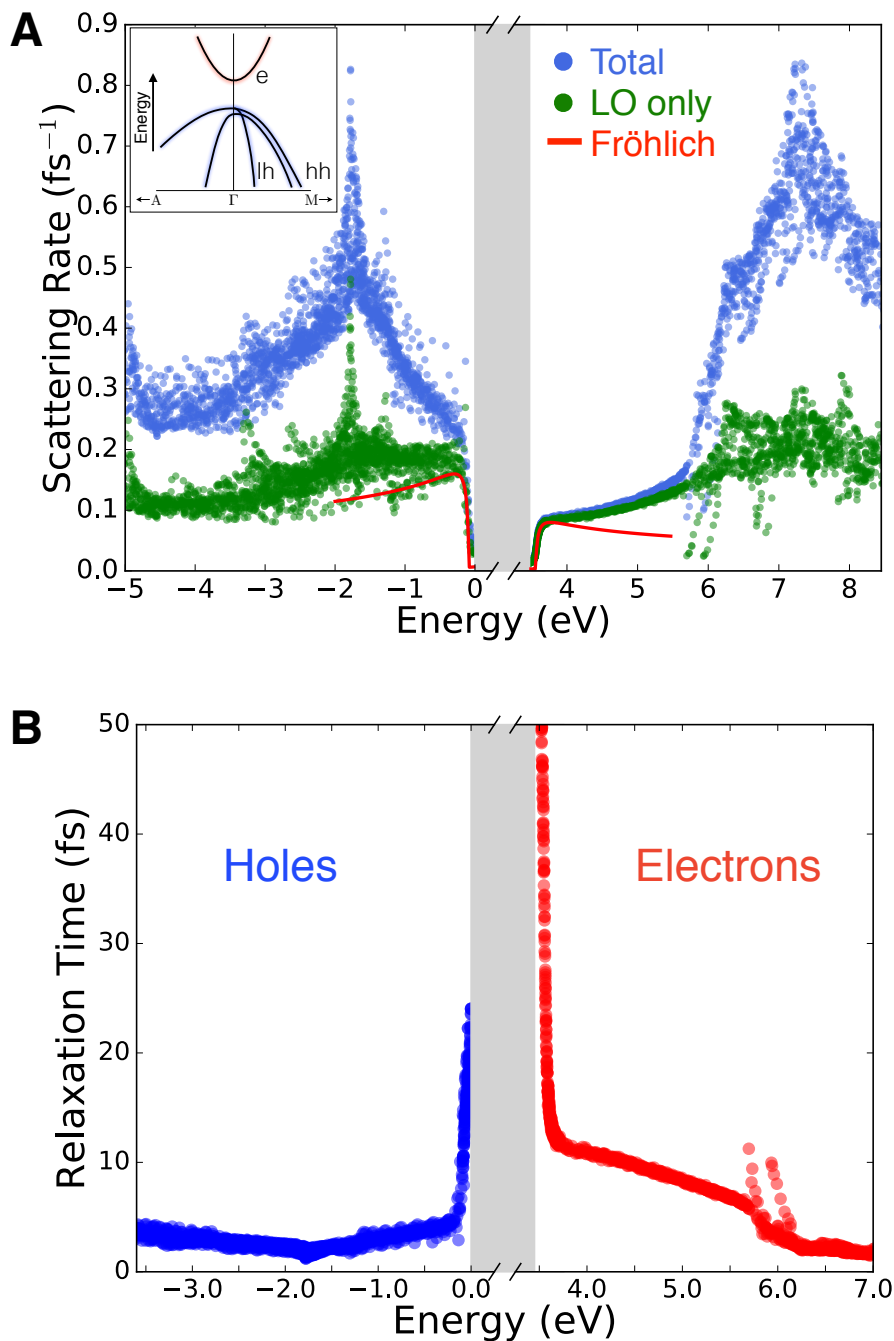
Figure 2.1: **First-principles e-ph scattering rates and relaxation times.**
(**A**) e-ph scattering rates in GaN at 300 K, for electrons and holes with energies within 5 eV of the band edges. Both the LO contribution and the total rate due to all phonon modes are shown. The red lines are the empirical Fröhlich scattering rates (see Eq. 2.1). A schematic of the bandstructure of GaN near the band edges is shown in the inset. (**B**) The e-ph relaxation times, defined as the inverse of the total scattering rates in (**A**). The zero of the energy axis is the valence band maximum, and the band gap is shown as a shaded area.

full mode-resolved scattering rates are shown in Fig. 2.5 of the Supplementary Materials (Section 2.7). For both electrons and holes, the scattering rate in Fig. 2.1A is very small within an LO phonon energy ($\hbar\omega_0 \approx 100$ meV) of the band edges, since the dominant process in this energy range is LO phonon absorption. The scattering rate increases rapidly up to $\sim$150 meV excess energy due to an increase in the phase space for LO phonon emission above $\hbar\omega_0$. The trend at low energy in the conduction band is consistent with the conventional picture, with LO mode emission dominating intra-valley scattering in the conduction valley at Γ, roughly up to 2 eV above the CBM. At higher energy in the conduction band, the total and LO mode electron scattering rates differ substantially due to inter-band scattering mediated by all phonon modes in roughly equal measure (see Fig. 2.5).

In the valence band, due to the presence of multiple bands at Γ, both intra-valley and inter-valley small-$\mathbf{q}$ transitions are possible within $\sim$1 eV of the VBM, thus resulting in a higher LO scattering rate (by roughly a factor of two) than in the conduction band within 1 eV of the CBM. The LO contribution becomes roughly constant at hole excess energies greater than $\sim$0.2 eV. Different from the conduction band where LO phonon emission is the only active process, the total scattering rate keeps increasing for holes with excess energy above 0.2 eV due to intra-valley and inter-valley scattering contributed, in roughly equal measure, by all acoustic and optical phonon modes (see Fig. 2.5). Within 2 eV of the band edges, the DOS in the valence band is greater than in the conduction band due to the presence of multiple valence bands and to the higher effective masses of holes compared to electrons. These effects result in scattering from phonon modes other than the LO becoming important at lower excess energies in the valence band due to a greater phase space for large-$\mathbf{q}$ scattering. Overall, the stronger LO polar and non-polar contributions in the valence band result in significantly higher scattering rates for holes compared to electrons within 2 eV of the band edges. This asymmetry has important consequences for carrier dynamics.

The empirical Fröhlich model shows two major limitations in reproducing the first-principles trends (see Fig. 2.1A). The empirical and first-principles rates exhibit opposite trends at excess energies greater than $\sim$150 meV. For energies where the LO phonon emission rate is roughly constant, the discrepancy

of the empirical Fröhlich rate is as large as $30-50\%$ for both electrons and holes. Note that first-principles calculations include all phonon modes on the same footing at all energies, while empirical e-ph calculations would account for modes other than the LO through mode-specific empirical deformation potentials [24]. Traditionally employed empirical models are thus inadequate to compute the e-ph scattering rates due to all phonon modes over a wide energy range, as is done here, and the first-principles approach is necessary.

As a consequence of the scattering rate asymmetry, the computed e-ph RTs (see Fig. 2.1B) of holes are overall significantly shorter than the RTs of electrons. Within 2 eV of the band edges, the electron RTs range between $10-50$ fs, while the hole RTs are of order $3-20$ fs. The electron RT above the threshold for LO phonon emission in the conduction band is $\sim$12 fs, in very good agreement with the LO phonon emission time of 16 fs recently measured for electrons by Suntrup *et al.* [13]. The detailed energy dependence of the RTs and scattering rates reported here is valuable for GaN device design.

2.3   Origin of the Carrier Relaxation Asymmetry in GaN

We address the question of whether the asymmetry between the electron and hole scattering rates found here is a mere consequence of the heavier effective mass of holes compared to electrons in GaN. In doing so, we develop an intuition for the origin of this asymmetry by analyzing separately the polar and non-polar e-ph scattering contributions. As noted above, the two sources of e-ph scattering are the long-range interaction from the LO polar mode and the short-range interactions from all other non-polar phonons. Because e-ph processes are determined by the e-ph coupling strength and the phase space available for scattering (see Section 2.6, Eq. 2.3), the non-polar scattering rate $\Gamma^{(\mathrm{NP})}$ approximately follows the same energy trend as the electronic DOS, $D(E)$, multiplied by an average e-ph coupling strength $\langle g^2 \rangle$, so that $\Gamma^{(\mathrm{NP})}(E) \propto \langle g^2 \rangle D(E)$. On the other hand, due to the long-range electrostatic nature of the polar interaction, the strength of LO coupling is insensitive to the specific electronic states involved in the scattering process. The LO mode polar coupling behaves as $|g^{LO}(q)|^2 \sim 1/q^2$ at small phonon wavevector q, resulting in much stronger LO scattering for small-$\mathbf{q}$ transitions. Due to this particular phonon wavevector dependence, the scattering rate $\Gamma^{(\mathrm{P})}$ due to the
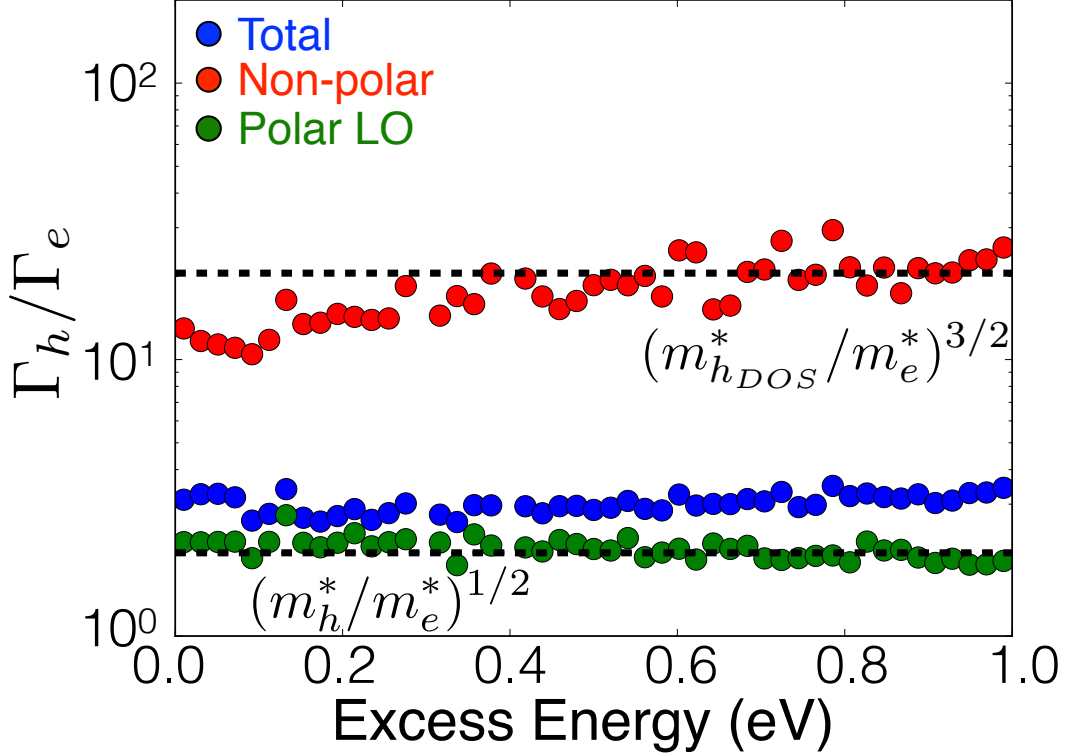
Figure 2.2: **Origin of the scattering rate asymmetry.** Ratio of the Brillouin zone averaged e-ph scattering rates of holes (Γ_h) to those of electrons (Γ_e) as a function of carrier excess energy. The zeros of the excess energy are the conduction and valence band edges for electrons and holes, respectively. The data points are computed using rates due to polar LO phonons (green), nonpolar phonons (red), and all phonon modes (blue). The dashed lines indicate the ratios $(m_h^*/m_e^*)^{1/2}$ and $(m_{h_{DOS}}^*/m_e^*)^{3/2}$ discussed in the text.

polar LO mode approaches the band edge with a constant trend in energy, as opposed to being proportional to the DOS as in the non-polar case. In the empirical Fröhlich formula (see Eq. 2.1), the polar scattering rate behaves as a simple function of the effective mass, $\Gamma^{(P)} \propto (m^*)^{1/2}$.

To quantify the scattering rate asymmetry, we compute in Fig. 2.2 the ratio of the BZ averaged scattering rate of holes (Γ_h) to that of electrons (Γ_e). The ratio Γ_h/Γ_e is shown for the average total, polar and non-polar scattering rates as a function of excess energy. For the LO polar contribution, the ratio closely matches the result expected based on the empirical Fröhlich model (see Eq. 2.1), namely, $\Gamma_h^{(P)}/\Gamma_e^{(P)} \approx (m_h^*/m_e^*)^{1/2}$, where m_h^* is the experimental hole effective mass [28]. The agreement between the empirical and *ab initio* ratios

of LO mode scattering rates indicates that the heavier hole effective mass is the main source of the LO polar scattering asymmetry, and that the empirical and *ab initio* treatments roughly factor out in the polar scattering rate ratio when a single m_h^* value is employed as a proxy of the multiple hole bands.

Since the non-polar scattering rate is proportional to the DOS, the ratio between the *ab initio* non-polar scattering rates is compared in Fig. 2.2 with a heuristic DOS ratio. Since the DOS of a parabolic band is proportional to $(m^*)^{3/2}$ [30], we expect that the ratio of the non-polar scattering rates at low energy is approximately $\Gamma_h^{(\mathrm{NP})}/\Gamma_e^{(\mathrm{NP})} \approx (m_{h_{DOS}}^*/m_e^*)^{3/2}$, where $m_{h_{DOS}}^*$ is the hole DOS effective mass [29]. The *ab initio* and DOS-based empirical non-polar ratios are in reasonable agreement. However, the inaccuracy of approximating multiple valence bands with a single DOS effective mass for holes, combined with the stronger average e-ph coupling strength for electrons (see Fig. 2.6 and Section 2.7A in the Supplementary Materials), both push the ratio below the heuristic prediction, with an energy-dependent discrepancy. Therefore, the ratio between the non-polar scattering rates cannot be accurately estimated without detailed knowledge of the bandstructure and e-ph coupling strengths.

Finally, since the total scattering rate is determined by the sum of the polar and non-polar contributions, the ratio between the *total* scattering rates of holes and electrons cannot be estimated by a simple heuristic model based on the effective masses. The average *ab initio* ratio between the total scattering rates found here is $\Gamma_h/\Gamma_e \approx 3$ within 1 eV of the band edges, and is bracketed by the non-polar and polar ratios. Detailed first-principles calculations, as employed here, are necessary to quantify this asymmetry in the scattering rates.

2.4   Real-time Hot Carrier Dynamics.

Simulating the HC dynamics in real time further highlights the different behavior of electrons and holes in GaN. To this end, we carry out numerical simulations of the dynamics of hot electron and hole populations injected in GaN with a range of initial excess energies. To represent the injected carriers, we employ narrow Gaussians distributions centered at the initial excess energy, and solve the electron BTE [1] in real time fully *ab initio* [2], using
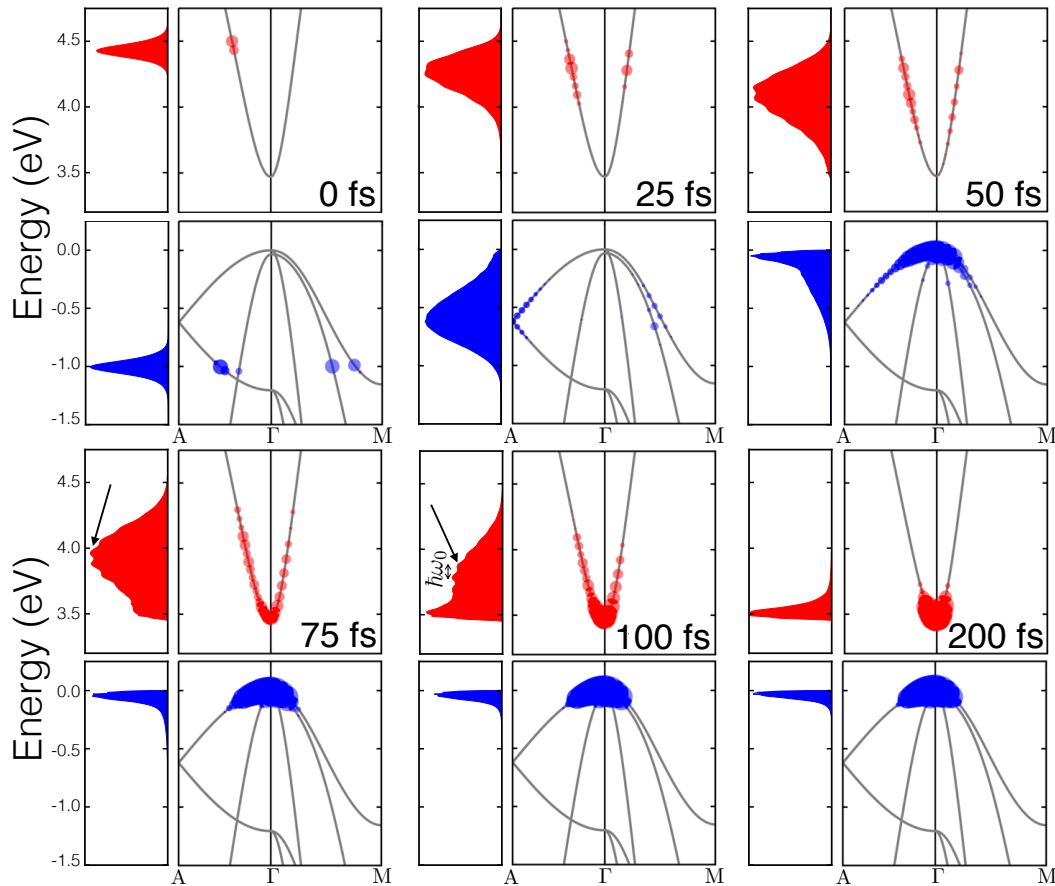
Figure 2.3: **Ultrafast dynamics of hot carriers in GaN.** Hot electrons (blue) and holes (red) are injected with a 1 eV excess energy with respect to the band edges, as modeled by creating initial Gaussian carrier distributions with a small energy width. The occupations $f_{n\mathbf{k}}$ for electrons and $1 - f_{n\mathbf{k}}$ for holes are shown at various times in the square panels along the A−Γ−M line of the Brillouin zone, with the point size proportional to the logarithm of the occupations. Left of each occupation panel we plot the average carrier concentrations (in arbitrary units) as a function of energy. The fluctuations in the electron concentration are indicated with an arrow in the 75 fs and 100 fs frames, along with their spacing of $\hbar\omega_0 \approx 100$ meV.

first-principles e-ph matrix elements, bandstructures and phonon dispersions (see Section 2.6). The carrier occupations are time-stepped using a 4th-order Runge-Kutta algorithm, while the phonon occupations are kept at 300 K, so that hot phonon effects are neglected.

Fig. 2.3 shows the time evolution of the electron and hole populations after injection with a 1 eV initial excess energy. At each time step, we analyze

both the carrier occupations ($f_{n\mathbf{k}}$ for electrons and $1-f_{n\mathbf{k}}$ for holes) along the A$-\Gamma-$M line of the BZ and the carrier concentrations as a function of energy, $\overline{f}(E)$, obtained by integrating the occupations at each energy over the BZ (see Section 2.6). Following HC generation, the electron and hole distributions broaden in energy and approach a Fermi-Dirac-like shape as they shift toward lower excess energies, eventually reaching the band edges. Both electrons and holes ultimately thermalize to a 300 K Fermi-Dirac distribution in equilibrium with the phonons, thus reaching the correct long-time limit for our simulations.

We find that while holes reach the band edges and cool in $\sim$80 fs, electrons are still far from equilibrium at the same time. Electron cooling is roughly five times slower, with electrons relaxing to the band edges in $\sim$200 fs after injection, and fully thermalizing to the 300 K equilibrium distribution in 400 fs. Interestingly, the dominant LO phonon emission for electrons results in distribution fluctuations at energies spaced apart by $\hbar\omega_0 \approx 100$ meV. These "wiggles" in the distributions are seen most clearly for electrons in the 75 fs and 100 fs panels in Fig. 2.3. The same simulation carried out for an initial carrier excess energy of 0.5 eV (see Fig. 2.7 in Section 2.7) shows even more pronounced fluctuations in the electron population. The asymmetry found here in the time scale for hot electron and hole cooling has not been reported previously, and is distinct from the transport asymmetry [16] due to the different effective masses and mobilities of electrons and holes.

Comparing our real-time dynamics with experiments is not straightforward, and should be done keeping in mind that our results pertain to the low carrier concentration regime. Several ultrafast pump-probe experiments have been carried out in GaN, but due to the high HC concentrations reached in some of these measurements, hot phonon effects become relevant as the emitted phonons re-excite the carriers, thus slowing down HC cooling compared to the low carrier concentration regime studied here. For example, Ye *et al.* [6] measured hot electron cooling in n-doped GaN. They concluded that LO emission is the dominant mechanism for hot electron cooling, consistent with our findings. They extracted a 0.2 ps LO emission time from their measurements, and observed that this value is significantly longer than the $\sim$10 fs empirical Fröhlich RT; this discrepancy is attributed in their work to hot phonon effects resulting from the high carrier density. In a subsequent work, the same au-

thors measured the cooling of hot holes in p-doped GaN [7]. They found that the hot hole data is difficult to fit with an LO phonon emission model because of the complexity of the valence band. We argue that the reason for this discrepancy, as shown in our work, is the significant scattering by phonon modes other than the LO in the valence band, even at low excess energy. While differences in the electron and hole dynamics are not discussed by Ye *et al.* [7], note that in their work the details of the early time evolution cannot be seen due to the 100 fs duration of the pump pulse, which sets the time resolution of the measurement. Our data provides evidence for an asymmetry between the electron and hole cooling times and mechanisms, which should be observable in new experiments with ~10 fs resolution.
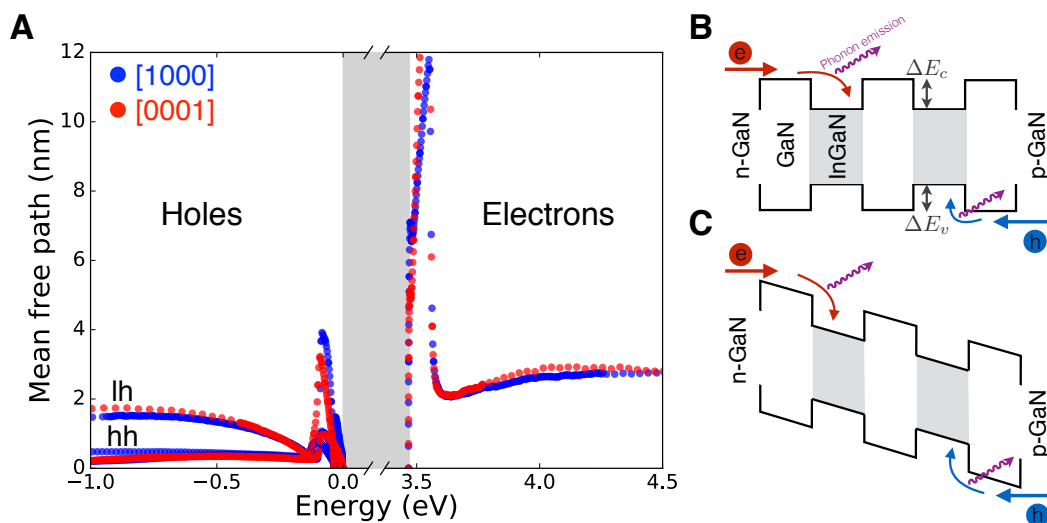
Figure 2.4: **Role of hot carriers in efficiency droop.** (**A**) Mean free paths, computed using calculated band velocities and e-ph relaxation times, along two crystal directions in GaN. The c-axis direction is labeled as [0001] and the in-plane direction as [1000]. For holes, the lower mean free path branch is due to the heavy-hole (hh) band, and the upper branch to the light-hole (lh) bands. The zero of the energy axis is the valence band maximum, and the band gap is shown with a shaded area. (**B**)-(**C**) Schematic band diagram of the active region of a InGaN/GaN LED. Shown are the stacked quantum wells, both without and with a driving electric field, in (**B**) and (**C**) respectively. The valence and conduction band offsets, ΔE_v and ΔE_c, are also indicated.

2.5 Role of Hot Carriers in LED Efficiency Droop.

We analyze the role of HCs in GaN LED devices. GaN and III-nitride LEDs are bipolar devices that emit light as a result of the recombination of electrons and holes in quantum well (QW) active layers [31, 32]. A key figure of merit in LEDs is the external quantum efficiency (EQE), defined as the ratio of generated photons per electron-hole pair introduced at the contacts. One of the main barriers toward commercialization of GaN LEDs is efficiency droop, a decay of the EQE at high driving current. Almost all GaN LEDs exhibit a maximum EQE at low current densities, with the EQE rapidly decreasing above the optimal current [16].

In a typical GaN LED design [31], electrons and holes are injected at the opposite ends of an active region that contains multiple InGaN QWs and has the bandstructure shown schematically in Fig. 2.4B. The multi-QW active region typically consists of up to 10 periods of a $\sim$3 nm thick $In_xGa_{1-x}N$ QW followed by an undoped $\sim$10 nm GaN spacer [16], a structure designed to maximize carrier confinement and recombination in the light emitting InGaN QWs. Due to the band offsets at the GaN/InGaN interface, electrons and holes are hot when injected into the QW, and need to cool to the band edges to emit light efficiently. The excess energy of the HCs at injection in the QW depends on the band offsets ΔE_c for electrons and ΔE_v for holes (see Fig. 2.4B), which are typically of order 0.5 eV for InGaN/GaN devices.

Carriers injected into the active region scatter with phonons, and after several phonon emission events lose enough energy to be confined in the QW by the band offset potential, following which the carriers cool to the QW band edges and recombine to emit light. The e-ph mean free paths (MFPs) $L_{n\mathbf{k}}$ characterize the average length traveled between phonon emission events by carriers moving in the direction $\hat{\mathbf{k}}$ in band n (here, the top valence bands for holes and bottom conduction band for electrons). The MFPs are obtained here as $L_{n\mathbf{k}} = v_{n\mathbf{k}}\tau_{n\mathbf{k}}$, using Wannier-interpolated band velocities $v_{n\mathbf{k}}$ [33, 34] and the e-ph relaxation times $\tau_{n\mathbf{k}}$ given in Fig. 2.1B. Fig. 2.4A shows the computed e-ph MFPs for carriers moving along the c-axis [0001] and in-plane [1000] directions in GaN, for energies within 1 eV of the band edges, which are typical for carrier injection in GaN LEDs. The slow hot electron cooling via LO emission results in relatively long electron MFPs ranging from 10 nm near

the CBM to 3 nm between 0.25−1 eV above the CBM. For comparison, the hole MFPs are much shorter, ∼3 nm close to the VBM and only 0.5 nm for the heavy-hole and 1.5 nm for the light-hole bands between 0.25−1 eV below the VBM. Note that these MFPs are lower bounds that pertain to the low carrier concentration regime, and that hot phonon effects can increase these values at high carrier concentration, especially for electrons where the only active e-ph scattering mechanism is LO phonon emission.

Since the typical QW thickness is ∼3 nm, the longer electron MFPs indicate that electrons need to cross on average several QWs before cooling to the band edge, while holes can cool effectively within a single QW. A fact relevant for droop is that as the current is increased, the driving electric field increases and further tilts the band edges in the active region, resulting in the tilted staircase potential shown in Fig. 2.4C. For typical LEDs operated at droop regime currents, using the devices in Ref. [35] as an example, the driving voltage is roughly 5 V. Assuming that ∼3 V fall over a roughly 150 nm thick undoped active region, the resulting active region electric field is of order 2×10^5 V/cm. For electrons losing an LO phonon energy of ∼100 meV as they travel a 3 nm MFP length, the cooling rate is of order 100 meV over 3 nm, and thus roughly 3×10^5 eV/cm. Droop thus occurs in a regime where the band tilting and the electron cooling rate are comparable, so that electrons cannot cool effectively against the tilted band edges. In this scenario, electrons that do not cool in the QW are swept by the electric field into the next QW, until a fraction of electrons leaks out of the active region without recombining radiatively, leading to a decreased EQE at high current as observed in efficiency droop. Our analysis highlights that HC cooling, and in particular the slow LO phonon emission rate of hot electrons occurring over lengths comparable with the QW thickness, can be an important factor determining efficiency droop.

The mitigation of droop seen experimentally by increasing the QW thickness [36] and number of QWs in the active region [35] is consistent with our findings. In our model of hot electron leakage, increasing the QW thickness or the total active region thickness will improve HC cooling and decrease the probability of electrons overflying the QWs, thus increasing the EQE. Interestingly, the above reports attribute the droop mitigation primarily to reduced Auger recombination rather than HC effects. While Auger processes may play

a role in droop, experimental evidence for Auger recombination in GaN LEDs is still scarce [16, 37]. Auger processes, if present with a high enough rate, would need to coexist with the e-ph scattering processes studied here, which are relevant at all carrier concentrations. Most notably, it has been found that the mechanism responsible for droop increases in strength at lower temperatures [38]. This behavior is in contrast with Auger scattering, since the dominant phonon-assisted Auger processes [15] would lead to stronger droop at higher temperatures. Note instead that e-ph scattering increases with increasing temperatures, so that lower temperatures are associated with longer hot carrier MFPs. Our model thus predicts that lower temperatures lead to longer electron MFPs and thus increased electron leakage and efficiency droop, consistent with experiment. The temperature dependence clearly suggests that e-ph scattering plays a key role in the efficiency droop.

Several authors have discussed HC effects and QW overfly as a potential source of droop [16, 39], showing that the use of electron blocking layers to stop carrier leakage and staircase injectors to lower carrier excess energy can drastically mitigate droop. Our first-principles calculations of e-ph scattering, HC cooling and MFPs provide a quantitative basis for understanding such HC effects. We conclude that the different cooling rates of hot electrons and holes found here, together with the longer electron MFPs compared to holes, can play an important role in GaN LEDs efficiency droop and deserve further experimental investigation.

In summary, we apply first-principles calculations to shed light on the microscopic HC dynamics in GaN, providing details beyond the reach of previously employed theoretical and experimental methods. Our key findings include a significant difference in hot hole and electron scattering and cooling, the origin of this asymmetry, and the non-negligible role of scattering mechanisms besides the polar LO mode for holes. A model is presented to explain droop as a consequence of hot electron cooling. Our results can be employed to include HC dynamics in GaN device scale modeling, which typically neglects HC effects. Future work will extend our calculations to InGaN and AlGaN. Taken together, our computational approach advances the design of GaN devices, and enables the engineering of novel lighting materials with microscopic insight.

2.6 Computational Methods

We carry out *ab initio* calculations on GaN in the wurtzite structure with relaxed lattice parameters of $a = 3.17\,\text{Å}$ and $c = 5.16\,\text{Å}$. The ground-state electronic structure is computed using the QUANTUM ESPRESSO code [40] within the local density approximation (LDA) [41] of DFT. We employ a plane-wave kinetic energy cutoff of 80 Ry and scalar-relativistic norm-conserving pseudopotentials [42] for both Ga and N. The pseudopotential of Ga includes a non-linear core correction [43] to account for the effect of the shallow $3d$ core states. The ground-state charge density is obtained using a $12 \times 12 \times 12$ **k**-point grid, following which a non-self-consistent calculation is employed to obtain the Kohn-Sham eigenvalues and wavefunctions on an $8 \times 8 \times 8$ **k**-point grid. We construct maximally localized Wannier functions (WFs) [44] using the Wannier90 code [45]. The Kohn-Sham wavefunctions are first projected onto four sp^3 orbitals on each Ga and N atom, for a total of 16 wannierized bands. The WF spread is then minimized, and the relevant energy windows [44] are adjusted until the interpolated bandstructure can smoothly reproduce the LDA result within ~ 10 meV throughout the BZ. The LDA eigenvalues are then corrected using the GW [46] quasiparticle energies of GaN computed in Ref. [47], by extracting an average energy dependent self-energy that is employed to apply a scissor shift of the conduction band minimum and a linear energy stretch of the valence and conduction band energies. Using the GW-corrected eigenvalues together with the WFs, interpolated GW quasiparticle energies with quality comparable to those in Ref. [47] are obtained, and employed in all calculations described below. The WF projected DOS in Fig. 2.6 of the Supplementary Materials (Section 2.7) is computed by projecting the Kohn-Sham wavefunctions $|\psi_{n\mathbf{k}}\rangle$ onto the WFs localized on the Ga and N atoms, respectively, using $\sum_{n\mathbf{k},\alpha \in \{\text{Ga, N}\}} \langle \psi_{nk}|\alpha \rangle \langle \alpha|\psi_{nk} \rangle \, \delta(E - E_{n\mathbf{k}})$.

Electron-phonon Scattering Calculations

We use density functional perturbation theory (DFPT) [26] to compute lattice dynamical properties and e-ph matrix elements $g_{nn'\nu}(\mathbf{k}, \mathbf{q})$ [2] on coarse $8 \times 8 \times 8$ **k**-point and $4 \times 4 \times 4$ **q**-point grids in the BZ. Here and in the following, the e-ph matrix elements [2] describe an electron in Bloch state $|n\mathbf{k}\rangle$, with quasiparticle

energy $E_{n\mathbf{k}}$, that scatters into the state $|n'\mathbf{k} + \mathbf{q}\rangle$ with quasiparticle energy $E_{n'\mathbf{k}+\mathbf{q}}$, due to a phonon with branch index ν, wavevector $\mathbf{q}$ and frequency $\omega_{\nu\mathbf{q}}$. The electron and phonon energies and the e-ph matrix elements are then interpolated on significantly finer grids using WFs [48]. Wannier interpolation of the matrix elements relies on the spatial localization of the e-ph interaction. In polar materials like GaN, however, the interaction of an electron with an LO phonon diverges as $\sim 1/q$ as predicted by the Fröhlich model [23, 27]. This singularity for $q \to 0$ results from the long-range field generated by the LO mode and is incompatible with Wannier interpolation. To overcome this issue, the e-ph matrix elements are separated into short- (S) and long-range (L) parts [27], $g_{nn'\nu}(\mathbf{k}, \mathbf{q}) = g_{nn'\nu}^S(\mathbf{k}, \mathbf{q}) + g_{nn'\nu}^L(\mathbf{k}, \mathbf{q})$, where g^S is computed by Wannier interpolation and g^L is evaluated using an analytical *ab initio* Fröhlich e-ph coupling based on the Vogl model [49]:

$$g_{nn'\nu}^L(\mathbf{k}, \mathbf{q}) = i\frac{4\pi}{\Omega}\frac{e^2}{4\pi\epsilon_0}\sum_{\kappa}\left(\frac{\hbar}{2\omega_{\nu\mathbf{q}}NM_\kappa}\right)^{\frac{1}{2}}\sum_{\mathbf{G}\neq-\mathbf{q}}\frac{(\mathbf{q}+\mathbf{G})\cdot Z_\kappa^* \cdot \mathbf{e}_{\kappa\nu}(\mathbf{q})}{(\mathbf{q}+\mathbf{G})\cdot\boldsymbol{\epsilon}^\infty\cdot(\mathbf{q}+\mathbf{G})} \quad (2.2)$$
$$\times \langle\Psi_{n'\mathbf{k}+\mathbf{q}}|e^{i(\mathbf{q}+\mathbf{G})\cdot(\mathbf{r}-\boldsymbol{\tau}_\kappa)}|\Psi_{n\mathbf{k}}\rangle,$$

where $\mathbf{G}$ is a reciprocal lattice vector, Ω is the volume of the unit cell, N is the number of points in the $\mathbf{q}$-grid, $\boldsymbol{\epsilon}^\infty$ is the high-frequency permittivity, and M_κ, $\boldsymbol{\tau}_\kappa$, and Z_κ^* are the mass, position, and Born effective charge tensor of atom κ in the unit cell, respectively, and $\mathbf{e}_{\kappa\nu}(\mathbf{q})$ is a vibrational eigenmode normalized in the unit cell. Note that we neglected a quadrupole moment contribution to polar phonon scattering due to the piezoelectric interaction [18, 49]; we have verified that this approximation has a negligible effect on the hot carrier dynamics. However, we found that it does play a non-negligible role in the carrier mobility, as discussed in Chapter 5.

The e-ph scattering rate $\Gamma_{n\mathbf{k}}$ for an electronic state with band n and crystal momentum $\mathbf{k}$ is obtained from the imaginary part of the lowest-order e-ph self-energy, using [1, 2]:

$$\Gamma_{n\mathbf{k}} = \frac{2\pi}{\hbar}\sum_{n'\mathbf{q}\nu}|g_{nn'\nu}(\mathbf{k}, \mathbf{q})|^2\times$$
$$[(N_{\nu\mathbf{q}} + 1 - f_{n'\mathbf{k}+\mathbf{q}})\,\delta(E_{n\mathbf{k}} - \hbar\omega_{\nu\mathbf{q}} - E_{n'\mathbf{k}+\mathbf{q}}) \quad (2.3)$$
$$+ (N_{\nu\mathbf{q}} + f_{n'\mathbf{k}+\mathbf{q}})\,\delta(E_{n\mathbf{k}} + \hbar\omega_{\nu\mathbf{q}} - E_{n'\mathbf{k}+\mathbf{q}})],$$

where $E_{n\mathbf{k}}$ and $\hbar\omega_{\nu\mathbf{q}}$ are the electron quasiparticle and phonon energies, respectively, and $f_{n\mathbf{k}}$ and $N_{\nu\mathbf{q}}$ the corresponding equilibrium occupations at 300

K. The scattering rate due to a given phonon mode is obtained by restricting the sum in Eq. 2.3 to the corresponding phonon branch index ν. Using an approach we recently developed [18], we compute and converge the scattering rate in Eq. (2.3) with an in-house developed code that can carry out, among other tasks, e-ph calculations analogous to the EPW code [50]. We split $|g|^2$ in Eq. (2.3) into the long-range part $|g^L|^2$ and the remainder $(|g|^2 - |g^L|^2)$, and separately compute and converge $\Gamma_{n\mathbf{k}}$ for these two contributions, which are then added up to obtain the total scattering rate. This approach leads to a dramatic speed-up compared to converging Eq. (2.3) with $|g|^2 = |g^S + g^L|^2$ directly [18]. The scattering rate is computed for $\mathbf{k}$ points on a fine $100{\times}100{\times}100$ grid in the BZ, using Gaussian broadening with a small parameter of 8 meV to approximate the δ function in Eq. (2.3). For each $\mathbf{k}$ point, we converge the long-range contribution with 10^6 random $\mathbf{q}$ points sampled from a Cauchy distribution [18], and the remainder contribution with 10^5 random $\mathbf{q}$ points from a uniform distribution. Convergence of all quantities is carefully verified.

Real-time Carrier Dynamics Simulations

We simulate HC cooling due to e-ph scattering in bulk GaN in the absence of external fields. The initial HC distribution is modeled with a narrow Gaussian centered at the initial HC energy. Separate calculations are carried out for electrons and holes, and for the two values of initial excess energy studied here (0.5 eV and 1 eV). The time evolution of the carrier distributions is obtained by solving the BTE [1, 2]:

$$\frac{\partial f_{n\mathbf{k}}(t)}{\partial t} = -\frac{2\pi}{\hbar} \sum_{n'\mathbf{q}\nu} |g_{nn'\nu}(\mathbf{k},\mathbf{q})|^2 [\delta(E_{n\mathbf{k}} - \hbar\omega_{\nu\mathbf{q}} - E_{n'\mathbf{k}+\mathbf{q}})F_{\text{em}}(t) \\ + \delta(E_{n\mathbf{k}} + \hbar\omega_{\nu\mathbf{q}} - E_{n'\mathbf{k}+\mathbf{q}})F_{\text{abs}}(t)], \tag{2.4}$$

where $f_{n\mathbf{k}}(t)$ is the time-dependent electron distribution, the e-ph matrix elements $g_{nn'\nu}(\mathbf{k},\mathbf{q})$ are computed in the ground state, and the phonon emission (F_{em}) and absorption (F_{abs}) terms are computed at each time step as [2]:

$$F_{\text{abs}} = f_{n\mathbf{k}}(1 - f_{n'\mathbf{k}+\mathbf{q}})N_{\nu\mathbf{q}} - f_{n'\mathbf{k}+\mathbf{q}}(1 - f_{n\mathbf{k}})(N_{\nu\mathbf{q}} + 1) \\ F_{\text{em}} = f_{n\mathbf{k}}(1 - f_{n'\mathbf{k}+\mathbf{q}})(N_{\nu\mathbf{q}} + 1) - f_{n'\mathbf{k}+\mathbf{q}}(1 - f_{n\mathbf{k}})N_{\nu\mathbf{q}}. \tag{2.5}$$

Phonon-phonon scattering and the change in phonon occupations are neglected in our simulations, where we fix $N_{\nu\mathbf{q}}$ to the equilibrium phonon occupations at

300 K. This approximation is justified in the low carrier concentration limit, in which hot phonon effects are negligible. We solve Eq. (2.4) numerically using the 4th-order Runge-Kutta method with a time step of 1 fs, using uniform fine grids of up to $100 \times 100 \times 100$ **k**- and **q**-points in the BZ. The BZ averaged energy-dependent carrier populations $\bar{f}(E, t)$ at energy E used in Fig. 2.3 are obtained as $\bar{f}(E, t) = \sum_{n\mathbf{k}} f_{n\mathbf{k}}(t)\delta(\epsilon_{n\mathbf{k}} - E)$ via tetrahedron integration. We developed an efficient scheme to speed up the solution of the BTE, to be detailed elsewhere, which combines MPI and OpenMP parallelizations to repeatedly compute the e-ph matrix elements and converge the scattering integral at each time step.

2.7   Supplementary Material
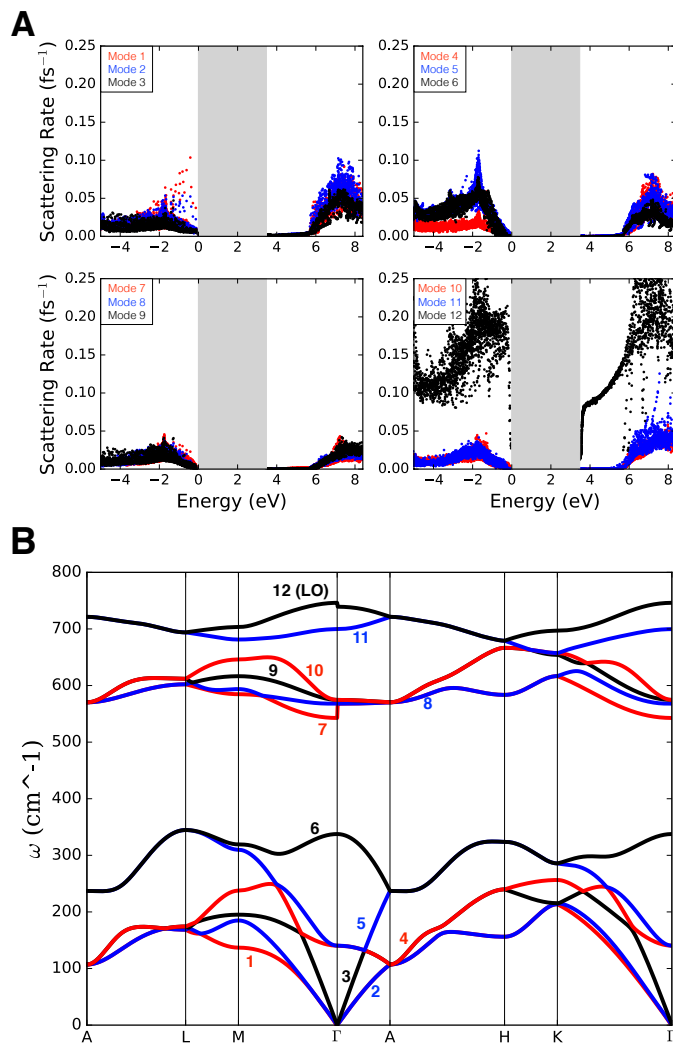
Figure 2.5: **Phonon mode-resolved electron-phonon scattering rates.**
(**A**) e-ph scattering rates due to each of the 12 phonon modes in a unit cell of
GaN at 300 K, shown for electrons and holes with energies within 5 eV of the
band edges. Except for mode 12, which is the LO mode, all other modes have
similar values of the scattering rate at each energy. The zero of the energy
axis is the valence band maximum, and the shaded area is the band gap. For
illustration purposes, modes are labeled according to increasing frequency at
each **q**-point, and thus according to their branch index, as color coded in panel
(**B**). (**B**) Phonon dispersions along high-symmetry lines, showing the phonon
branch labeling used in (**A**).

Section 2.7A. Origin of the stronger e-ph coupling for electrons compared to holes.

As discussed in the main text, the non-polar scattering rate $\Gamma^{(\mathrm{NP})}$ approximately follows the same energy trend as the electronic DOS, $D(E)$, multiplied by an average e-ph coupling strength $\langle g^2 \rangle$, so that $\Gamma^{(\mathrm{NP})}(E) \propto \langle g^2 \rangle D(E)$. The non-polar scattering rate and the DOS are shown in Fig. 2.6A. We find a stronger average e-ph coupling for electrons compared to holes, as seen by the greater ratio of the scattering rate to the DOS for electrons, which is more clearly visible in Fig. 2.6A at excess energies higher than 2 eV. Since the e-ph coupling strength $|g|^2$ is related to the overlap of initial and final states with roughly the same energy, we attribute this difference in the e-ph coupling strength to the different orbital characters in the valence and conduction bands. We quantify the wavefunction overlap by computing the Wannier function (WF) projected DOS (see Section 2.6), shown in Fig. 2.6B, and the spatial spread of the WFs centered on the N and Ga atoms, visualized in Fig. 2.6C. We find that the valence band character is dominated by WFs centered on N atoms with a spread of ~0.7 Å^2, while the conduction band character is dominated by WFs centered on Ga atoms with a spread of ~1.7 Å^2. The fact that the WFs on Ga are more extended than those on N makes them more sensitive to local potential perturbations due to ionic displacements, resulting in the stronger e-ph coupling seen in the conduction band. Note that this difference in spatial extent is related to the polar nature of GaN, suggesting that the stronger short-range e-ph coupling in the conduction band is likely present in other polar compounds.
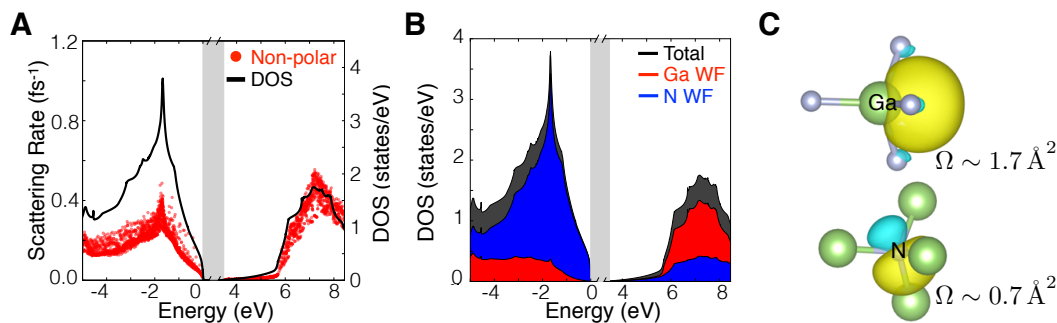
Figure 2.6: **Origin of the stronger electron-phonon coupling for electrons compared to holes.** (**A**) e-ph scattering rates due to all non-polar phonon modes. The electronic DOS is also shown. Note the higher scattering rate to DOS ratio (and thus the higher average e-ph coupling) in the conduction band. (**B**) Wannier functions (WFs) projected and total DOS. The projected DOS for WFs centered on N and Ga atoms are shown with blue and red filled curves, respectively. The total DOS, shown in black, is the sum of the two. In panels (**A**) and (**B**), the zero of the energy axis is the valence band maximum, and the band gap is shown as a shaded area. (**C**) Example WFs on N and on Ga are visualized, where the spread Ω of each WF is also indicated.
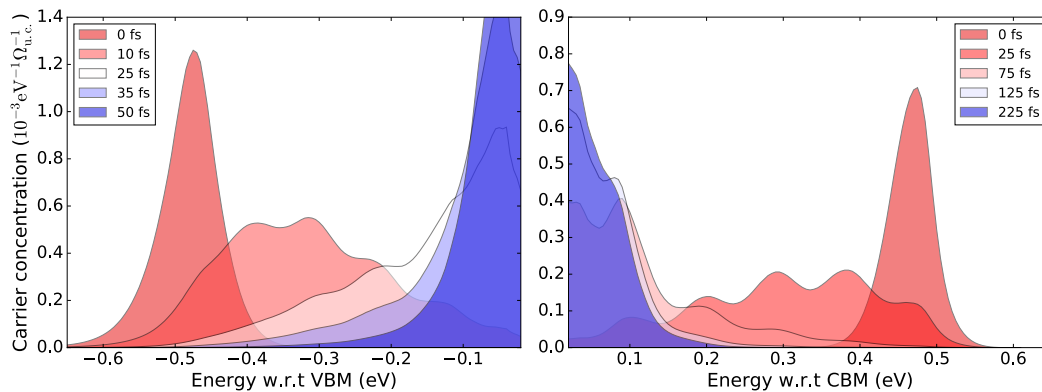
Figure 2.7: **Simulated hot carrier dynamics for 0.5 eV initial excess energy.** Holes (left) and electrons (right) are injected with a 0.5 eV excess energy with respect to the band edges, as modeled by creating initial Gaussian carrier distributions with a small energy width. The average carrier concentrations as a function of energy for electrons and holes are shown at various times. The asymmetry between the cooling times of holes (50 fs) and electrons (over 250 fs) is clearly visible, and so are the wiggles in the electron distributions, which are spaced apart by $\hbar\omega_0 \approx 100$ meV, as discussed in the main text.

References

[1] G. D. Mahan, *Condensed matter in a nutshell* (Princeton University Press, 2010).

[2] M. Bernardi, "First-principles dynamics of electrons and phonons", Eur. Phys. J. B **89**, 239 (2016).

[3] G. Meneghesso, G. Verzellesi, F. Danesin, F. Rampazzo, F. Zanon, A. Tazzoli, M. Meneghini, and E. Zanoni, "Reliability of GaN high-electron-mobility transistors: State of the art and perspectives", IEEE T. Device Mat. Re. **8**, 332–343 (2008).

[4] S. Chowdhury, B. L. Swenson, M. H. Wong, and U. K. Mishra, "Current status and scope of gallium nitride-based vertical transistors for high-power electronics application", Semicond. Sci. Tech. **28**, 074014 (2013).

[5] S. Dasgupta, Nidhi, A. Raman, J. S. Speck, and U. K. Mishra, "Experimental demonstration of III-nitride hot-electron transistor with GaN base", IEEE Electr. Device L. **32**, 1212–1214 (2011).

[6] H. Ye, G. W. Wicks, and P. M. Fauchet, "Hot electron relaxation time in GaN", Appl. Phys. Lett. **74**, 711 (1999).

[7] H. Ye, G. W. Wicks, and P. M. Fauchet, "Hot hole relaxation dynamics in p-GaN", Appl. Phys. Lett. **77**, 1185–1187 (2000).

[8] N. M. Stanton, A. J. Kent, A. V. Akimov, P. Hawker, T. S. Cheng, and C. T. Foxon, "Energy relaxation by hot electrons in n-GaN epilayers", J. Appl. Phys. **89**, 973–979 (2001).

[9] N. Balkan, M. C. Arikan, S. Gokden, V. Tilak, B. Schaff, and R. J. Shealy, "Energy and momentum relaxation of hot electrons in GaN/AlGaN", J. Phys.: Condens. Matter **14**, 3457 (2002).

[10] K. Wang, J. Simon, N. Goel, and D. Jena, "Optical study of hot electron transport in GaN: Signatures of the hot-phonon effect", Appl. Phys. Lett. **88**, 022103 (2006).

[11] S. Wu, P. Geiser, J. Jun, J. Karpinski, D. Wang, and R. Sobolewski, "Time-resolved intervalley transitions in GaN single crystals", J. Appl. Phys. **101**, 043701 (2007).

[12] S. K. Tripathy, G. Xu, X. Mu, Y. J. Ding, K. Wang, Y. Cao, D. Jena, and J. B. Khurgin, "Evidence of hot electrons generated from an al n/ ga n high electron mobility transistor", Appl. Phys. Lett. **92**, 013513 (2008).

[13] D. J. Suntrup, G. Gupta, H. Li, S. Keller, and U. K. Mishra, "Measurement of the hot electron mean free path and the momentum relaxation rate in GaN", Appl. Phys. Lett. **105**, 2014–2017 (2014).

[14]E. Kioupakis, P. Rinke, K. T. Delaney, and C. G. Van de Walle, "Indirect Auger recombination as a cause of efficiency droop in nitride light-emitting diodes", Appl. Phys. Lett. **98**, 161107 (2011).

[15]E. Kioupakis, D. Steiauf, P. Rinke, K. T. Delaney, and C. G. Van de Walle, "First-principles calculations of indirect Auger recombination in nitride semiconductors", Phys. Rev. B **92**, 035207 (2015).

[16]G. Verzellesi, D. Saguatti, M. Meneghini, F. Bertazzi, M. Goano, G. Meneghesso, and E. Zanoni, "Efficiency droop in InGaN/GaN blue light-emitting diodes: Physical mechanisms and remedies", J. Appl. Phys. **114**, 071101 (2013).

[17]J. I. Mustafa, M. Bernardi, J. B. Neaton, and S. G. Louie, "*Ab initio* electronic relaxation times and transport in noble metals", Phys. Rev. B **94**, 155105 (2016).

[18]J.-J. Zhou and M. Bernardi, "*Ab initio* electron mobility and polar phonon scattering in GaAs", Phys. Rev. B **94**, 201201(R) (2016).

[19]M. Bernardi, D. Vigil-Fowler, J. Lischner, J. B. Neaton, and S. G. Louie, "*Ab initio* study of hot carriers in the first picosecond after sunlight absorption in silicon", Phys. Rev. Lett. **112**, 257402 (2014).

[20]M. Bernardi, D. Vigil-Fowler, C. S. Ong, J. B. Neaton, and S. G. Louie, "*Ab initio* study of hot electrons in GaAs", Proc. Nat. Acad. of Sci. U.S.A **112**, 5291–5296 (2015).

[21]M. Bernardi, J. Mustafa, J. B. Neaton, and S. G. Louie, "Theory and computation of hot carriers generated by surface plasmon polaritons in noble metals", Nat. Commun. **6** (2015).

[22]M. Palummo, M. Bernardi, and J. C. Grossman, "Exciton radiative lifetimes in two-dimensional transition metal dichalcogenides", Nano Lett. **15**, 2794–2800 (2015).

[23]H. Fröhlich, "Electrons in lattice fields", Adv. Phys. **3**, 325–361 (1954).

[24]B. K. Ridley, *Quantum processes in semiconductors* (Oxford University Press, 2013).

[25]R. M. Martin, *Electronic structrure: basic theory and practial methods* (Cambridge University Press, 2008).

[26]S. Baroni, S. de Gironcoli, A. Dal Corso, and P. Giannozzi, "Phonons and related crystal properties from density-functional perturbation theory", Rev. Mod. Phys. **73**, 515–562 (2001).

[27]C. Verdi and F. Giustino, "Fröhlich electron-phonon vertex from first principles", Phys. Rev. Lett. **115**, 176401 (2015).

[28]J. Pankove, "Optical properties of GaN", RCA Rev. **36**, 163–176 (1975).

[29]V. Bougrov, M. Levinshtein, S. Rumyantsev, and A. Zubrilov, "Gallium nitride", in *Properties of advanced semiconductor materials: gan, AlN, inn, bn, sic, sige*, edited by M. E. Levinshtein, S. L. Rumyantsev, and M. S. Shur (John Wiley & Sons, New York, 2001) Chap. 1, pp. 1–30.

[30]N. Ashcroft and N. Mermin, *Solid state physics*, HRW international editions (Holt, Rinehart and Winston, 1976).

[31]S. Pimputkar, J. S. Speck, S. P. DenBaars, and S. Nakamura, "Prospects for LED lighting", Nat. Photon. **3**, 180–182 (2009).

[32]M. T. Hardy, D. F. Feezell, S. P. DenBaars, and S. Nakamura, "Group III-nitride lasers: a materials perspective", Mater. Today **14**, 408–415 (2011).

[33]J. R. Yates, X. Wang, D. Vanderbilt, and I. Souza, "Spectral and Fermi surface properties from Wannier interpolation", Phys. Rev. B **75**, 195121 (2007).

[34]A. A. Mostofi, J. R. Yates, G. Pizzi, Y.-S. Lee, I. Souza, D. Vanderbilt, and N. Marzari, "An updated version of Wannier90: A tool for obtaining maximally-localised Wannier functions", Comput. Phys. Commun. **185**, 2309–2310 (2014).

[35]S. Tanaka, Y. Zhao, I. Koslow, C.-C. Pan, H.-T. Chen, J. Sonoda, S. DenBaars, and S. Nakamura, "Droop improvement in high current range on PSS-LEDs", Electron. Lett. **47**, 335–336 (2011).

[36]N. F. Gardner, G. O. Müller, Y. C. Shen, G. Chen, S. Watanabe, W. Götz, and M. R. Krames, "Blue-emitting InGaN–GaN double-heterostructure light-emitting diodes reaching maximum quantum efficiency above 200 A / cm^2", Appl. Phys. Lett. **91**, 243506 (2007).

[37]J. Zhang, D. Zhang, D. Ye, C. Xu, and M. Huang, "Efficiency droop in III-nitride LEDs", in *Optoelectronics - materials and devices*, edited by S. L. Pyshkin and J. Ballato (Intech, 2015).

[38]J. Hader, J. V. Moloney, and S. W. Koch, "Temperature-dependence of the internal efficiency droop in gan-based diodes", Appl. Phys. Lett. **99**, 181127 (2011).

[39]X. Ni, X. Li, J. Lee, S. Liu, V. Avrutin, Ü. Özgür, H. Morkoç, and A. Matulionis, "Hot electron effects on efficiency degradation in InGaN light emitting diodes and designs to mitigate them", J. Appl. Phys. **108**, 033112 (2010).

[40]P. Giannozzi, S. Baroni, N. Bonini, M. Calandra, R. Car, C. Cavazzoni, D. Ceresoli, G. L. Chiarotti, M. Cococcioni, I. Dabo, et al., "QUANTUM ESPRESSO: a modular and open-source software project for quantum simulations of materials", J. Phys.: Condens. Matter **21**, 395502 (2009).

[41]J. P. Perdew and A. Zunger, "Self-interaction correction to density-functional approximations for many-electron systems", Phys. Rev. B **23**, 5048 (1981).

[42] N. Troullier and J. L. Martins, "Efficient pseudopotentials for plane-wave calculations", Phys. Rev. B **43**, 1993 (1991).

[43] S. G. Louie, S. Froyen, and M. L. Cohen, "Nonlinear ionic pseudopotentials in spin-density-functional calculations", Phys. Rev. B **26**, 1738–1742 (1982).

[44] N. Marzari, A. A. Mostofi, J. R. Yates, I. Souza, and D. Vanderbilt, "Maximally localized Wannier functions: Theory and applications", Rev. Mod. Phys. **84**, 1419–1475 (2012).

[45] A. A. Mostofi, J. R. Yates, Y.-S. Lee, I. Souza, D. Vanderbilt, and N. Marzari, "Wannier90: A tool for obtaining maximally-localised Wannier functions", Comput. Phys. Commun. **178**, 685–699 (2008).

[46] M. S. Hybertsen and S. G. Louie, "Electron correlation in semiconductors and insulators: band gaps and quasiparticle energies", Phys. Rev. B **34**, 5390–5413 (1986).

[47] A. Rubio, J. L. Corkill, M. L. Cohen, E. L. Shirley, and S. G. Louie, "Quasiparticle band structure of AlN and GaN", Phys. Rev. B **48**, 11810–11816 (1993).

[48] F. Giustino, M. L. Cohen, and S. G. Louie, "Electron-phonon interaction using Wannier functions", Phys. Rev. B **76**, 165108 (2007).

[49] P. Vogl, "Microscopic theory of electron-phonon interaction in insulators or semiconductors", Phys. Rev. B **13**, 694–704 (1976).

[50] J. Noffsinger, F. Giustino, B. D. Malone, C.-H. Park, S. G. Louie, and M. L. Cohen, "EPW: a program for calculating the electron–phonon coupling using maximally localized Wannier functions", Comput. Phys. Comm. **181**, 2140–2148 (2010).

C h a p t e r   3

AB INITIO CALCULATIONS OF EXCITON RADIATIVE LIFETIMES IN BULK CRYSTALS, NANOSTRUCTURES, AND MOLECULES

The content of this chapter is taken from the following work:

[1]H.-Y. Chen, V. A. Jhalani, M. Palummo, and M. Bernardi, "Ab initio calculations of exciton radiative lifetimes in bulk crystals, nanostructures and molecules", *Submitted.* arXiv preprint arXiv:1901.08747 (2019).

3.1 Introduction

Recall that excitons are neutral excitations consisting of an electron-hole pair bound by the Coulomb interaction. In bulk metals, where the Coulomb interaction is screened by the conduction electrons, electron-hole pairs can be regarded as effectively non-interacting, and thus excitons do not form. However, in semiconductors and insulators, and particularly in molecular and nanostructured materials, where electron-hole interactions are weakly screened, excitonic effects dominate the low-energy absorption spectrum and the radiative processes [1]. Excitons play a key role in regulating carrier dynamics and light emission processes in materials [2–5]. Yet, calculations of radiative lifetimes typically employ simplified empirical models that can only qualitatively explain or fit the experimental data [6–8], or are carried out in the independent-particle picture [9–11], neglecting excitons altogether. Over the last few years, first-principles approaches have become a new tool for accurately predicting exciton radiative lifetimes and light emission [12–14].

These approaches employ the *ab initio* Bethe-Salpeter equation (BSE) [15, 16] as a starting point to compute the exciton radiative lifetimes. A calculation of this kind was first proposed by Spataru *et al.* [12] to compute the radiative lifetimes in a one-dimensional (1D) system (carbon nanotubes). Recently, members of our group formulated the theory of exciton recombination and radiative lifetimes in two-dimensional (2D) materials [13, 14], where deriving the radiative lifetimes is more challenging, and computing and diagonalizing

the BSE Hamiltonian is more computationally expensive compared to the 1D case. This approach has enabled accurate predictions of the radiative lifetimes, as well as their temperature dependence and anisotropy, in novel 2D semiconductors [13, 14]. However, for the main light emitters of technological interest, including bulk crystals such as the III-V semiconductors (where the calculation is even more challenging than in 2D), molecules, single quantum emitters, quantum dots and other zero-dimensional (0D) systems, an *ab initio* approach for computing exciton recombination and the associated radiative lifetimes has not yet been rigorously derived.

In this work, we present a unified formulation of exciton radiative lifetimes in bulk crystals, 2D and 1D materials, and 0D isolated systems. The bulk and 0D cases are derived here from scratch, while the 2D and 1D cases, for which previous derivations exist, are briefly reviewed. As a validation, we further apply our approach to compute the radiative lifetimes in a GaAs crystal and in several gas phase organic molecules. Our work presents a broadly applicable approach to study light emission in materials, providing both the relevant equations and an *ab initio* workflow for computing radiative lifetimes in materials ranging from bulk crystals to nanostructures and molecules.

The chapter is organized as follows. In Sec. 3.2 we briefly review the *ab initio* BSE approach and derive the second quantization of light in materials. In Sec. 3.3 we present a general approach for computing exciton radiative lifetimes using Fermi's golden rule, and derive the radiative rate as a function of temperature for different cases, including bulk, 2D, 1D and 0D systems, each in a separate subsection. In Sec. 3.4 we present numerical calculations of radiative lifetimes in a GaAs crystal and in gas-phase organic molecules. We summarize the results and discuss future research in Sec. 3.5.

3.2 Theoretical Framework

In this section, we briefly review the *ab initio* BSE approach [15, 16] for studying excitons from first principles and derive the second quantization of light in anisotropic materials.

Excitons and the Bethe-Salpeter Equation

An exciton state can be represented in the so-called "transition space" using pairs of electron-hole states as a basis. In a periodic system, these states are Bloch wavefunctions characterized by the band index and crystal momentum. Within the Tamm-Dancoff approximation, which ignores antiresonant transition terms [17], an exciton state S with center-of-mass momentum $\mathbf{Q}$ can be written as a superposition of electron-hole states,

$$|S\mathbf{Q}\rangle = \sum_{vc\mathbf{k}} A_{vc\mathbf{k}}^{S\mathbf{Q}} |v\mathbf{k}\rangle_h |c\mathbf{k} + \mathbf{Q}\rangle_e \ , \qquad (3.1)$$

where v labels the valence and c the conduction bands, $\mathbf{k}$ is the electron crystal momentum, and the subscripts e and h denote electron and hole states, respectively. The expansion coefficients $A_{vc\mathbf{k}}^{S\mathbf{Q}}$ can be obtained by solving the BSE, which is shown diagrammatically in Fig. 3.1 and can be written as [15]

$$L(12; 1'2') = L_0(12; 1'2') + L_0(1\bar{4}; 1'\bar{3})K(\bar{3}\bar{5}; \bar{4}\bar{6})L(\bar{6}2; \bar{5}2'), \qquad (3.2)$$

where we use numbers for spacetime coordinates, *i.e.*, $1 = (\mathbf{r}_1, t_1)$, and the overlines denote dummy integration variables. Here, $L(12; 1'2')$ is the exciton correlation function and $L_0(12; 1'2') = G_1(1, 2')G_1(2, 1')$ its non-interacting counterpart, with G_1 the one-body Green's function. The key ingredient in the BSE is the kernel $K(\bar{3}\bar{5}; \bar{4}\bar{6})$, which encodes the interaction between the electron and hole. Within the GW approximation, it can be written as

$$K(35; 46) = -i\delta(3, 4)\delta(5^-, 6)v_c(3, 6) + i\delta(3, 6)\delta(4, 5)W(3^+, 4), \qquad (3.3)$$

where the first term is the exchange and the second the screened Coulomb interaction.

In the transition basis defined in Eq. (3.1), solving the BSE reduces to the eigenvalue problem [16]

$$(E_{c\mathbf{k}+\mathbf{Q}} - E_{v\mathbf{k}})A_{vc\mathbf{k}}^{S\mathbf{Q}} + \sum_{v'c'\mathbf{k}'} K_{vc\mathbf{k},v'c'\mathbf{k}'}A_{v'c'\mathbf{k}'}^{S\mathbf{Q}} = E_S(\mathbf{Q})A_{vc\mathbf{k}}^{S\mathbf{Q}} \qquad (3.4)$$

where $E_{c\mathbf{k}+\mathbf{Q}}$ and $E_{v\mathbf{k}}$ are the electron and hole quasiparticle energies, and kernel $K_{vc\mathbf{k},v'c'\mathbf{k}'}$ can be written in the electron-hole basis as [16]:

$$K_{vc\mathbf{k},v'c'\mathbf{k}'} = i\psi_{v\mathbf{k}}(\bar{4})\,\psi_{c\mathbf{k}+\mathbf{Q}}^*(\bar{3})\,K(\bar{3}\bar{5}, \bar{4}\bar{6})\,\psi_{v'\mathbf{k}'}^*(\bar{5})\,\psi_{c'\mathbf{k}'+\mathbf{Q}}(\bar{6})\,, \qquad (3.5)$$

where $\psi_{c(v)\mathbf{k}}$ are conduction (valence) single-electron Bloch wavefunctions. In
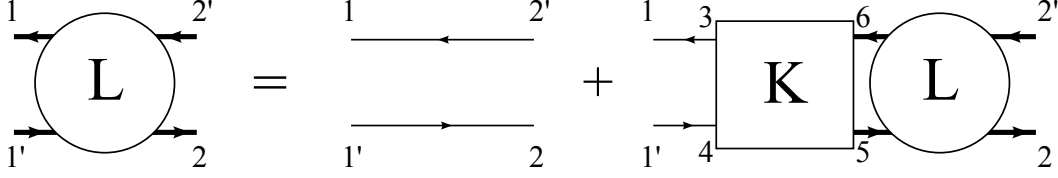
Figure 3.1: The Bethe-Salpeter equation in its Dyson form, shown using Feynman diagrams. For details, see Ref. [15].

practice, the *ab initio* BSE is solved by constructing the kernel (typically from the static RPA dielectric function) and diagonalizing Eq. (3.4) with a linear algebra package. Several codes implement this workflow, including YAMBO [18], ABINIT [19] and BERKELEYGW [20].

Quantization of Light in Anisotropic Materials

To derive the radiative lifetime in bulk crystals with general symmetry, we present the non-relativistic theory of second quantization of light in bulk materials. The theory for isotropic bulk materials is presented in Ref. [21], and extended here to anisotropic bulk materials. We write the dielectric tensor in diagonal form, $\boldsymbol{\epsilon}_r = \mathrm{diag}(\epsilon_x, \epsilon_y, \epsilon_z)$, and work in a generalized Coulomb gauge in which $\boldsymbol{\nabla} \cdot (\epsilon_0 \boldsymbol{\epsilon}_r \mathbf{E}) = 0$. The equation of motion for the vector potential $\mathbf{A}$ becomes

$$-\mu_0 \epsilon_0 \boldsymbol{\epsilon}_r \frac{\partial^2 \mathbf{A}}{\partial^2 t} = \boldsymbol{\nabla} \times (\boldsymbol{\nabla} \times \mathbf{A}) = \boldsymbol{\nabla}(\boldsymbol{\nabla} \cdot \mathbf{A}) - \boldsymbol{\nabla}^2 \mathbf{A}, \qquad (3.6)$$

using which we can construct the Lagrangian

$$\mathcal{L} = \frac{1}{2} \int d\mathbf{r} \left[\epsilon_0 \dot{\mathbf{A}}^T(\mathbf{r}) \boldsymbol{\epsilon}_r \dot{\mathbf{A}}(\mathbf{r}) - \frac{(\boldsymbol{\nabla} \times \mathbf{A})^2}{\mu_0} \right]. \qquad (3.7)$$

Since the conjugate momentum is $\boldsymbol{\Pi}(\mathbf{r}) = \epsilon_0 \boldsymbol{\epsilon}_r \dot{\mathbf{A}}(\mathbf{r})$, the Hamiltonian reads

$$\mathcal{H} = \int d\mathbf{r}\, \boldsymbol{\Pi} \dot{\mathbf{A}} - \mathcal{L} = \frac{1}{2} \int d\mathbf{r} \left[\frac{\boldsymbol{\Pi}^T \boldsymbol{\epsilon}_r^{-1} \boldsymbol{\Pi}}{\epsilon_0} + \frac{(\boldsymbol{\nabla} \times \mathbf{A})^2}{\mu_0} \right]. \qquad (3.8)$$

We can recover the Hamiltonian for the classical electromagnetic field in vacuum by setting $\boldsymbol{\epsilon}_r = \mathbf{I}$. To define creation and annihilation operators for second quantization, we solve Eq. (3.6) and obtain

$$\mathbf{A} = \sum_{\lambda \mathbf{q}} \sqrt{\frac{\hbar}{2V \omega_{\lambda \mathbf{q}} \epsilon_0}} \left(\hat{a}_{\lambda \mathbf{q}} \mathbf{e}_{\lambda \mathbf{q}} e^{i(\mathbf{q} \cdot \mathbf{r} + \omega_{\lambda \mathbf{q}} t)} + h.c. \right), \qquad (3.9)$$

where $h.\,c.$ stands for Hermitian conjugate, and the photon frequencies $\omega_{\lambda\mathbf{q}}$ and polarization vectors $\mathbf{e}_{\lambda\mathbf{q}}$ (where λ labels the mode, and $\mathbf{q}$ the photon wavevector) are obtained by solving Eq. (A.15) in Appendix A, with the polarization vectors satisfying the generalized orthogonality condition [22]

$$\mathbf{e}_{\lambda\mathbf{q}}^{\dagger}\boldsymbol{\epsilon}_r\mathbf{e}_{\lambda'\mathbf{q}} = \delta_{\lambda,\lambda'}. \tag{3.10}$$

This equation, together with Eq. (A.15) in Appendix A, provide the photon frequencies and polarization vectors needed to compute the radiative lifetime in bulk crystals. Using these results, the electromagnetic field Hamiltonian in Eq. (3.8) can be converted to the standard quantum oscillator form, $\mathcal{H} = \sum_{\lambda\mathbf{q}} \hbar\omega_{\lambda\mathbf{q}} \left(\hat{a}_{\lambda\mathbf{q}}^{\dagger}\hat{a}_{\lambda\mathbf{q}} + 1/2\right)$. Additional details are provided in Appendix A.

3.3 Exciton Radiative Lifetimes

General theory

We use the minimal coupling Hamiltonian to describe the interaction between electrons and photons, $H_{\text{int}} = -\frac{e}{m}\mathbf{A} \cdot \mathbf{p}$, where $\mathbf{p}$ is the momentum operator and $\mathbf{A}$ the vector potential in second quantized form (here and below, e and m are the electron charge and mass, respectively, and we use SI units) [23]. The radiative recombination rate at zero temperature for an exciton in state S with center-of-mass momentum $\mathbf{Q}$ can be written using Fermi's golden rule as

$$\gamma_S(\mathbf{Q}) = \frac{2\pi}{\hbar} \sum_{\lambda\mathbf{q}} |\langle G, 1_{\lambda\mathbf{q}}|H_{\text{int}}|S\mathbf{Q}, 0\rangle|^2 \, \delta\left(E_S(\mathbf{Q}) - \hbar\omega_{\lambda\mathbf{q}}\right)$$

$$= \frac{\pi e^2}{\epsilon_0 m^2 V} \sum_{\lambda\mathbf{q}} \frac{1}{\omega_{\lambda\mathbf{q}}} |\mathbf{e}_{\lambda\mathbf{q}} \cdot \mathbf{p}_S(\mathbf{Q})|^2 \, \delta\left(E_S(\mathbf{Q}) - \hbar\omega_{\lambda\mathbf{q}}\right),$$

$$\tag{3.11}$$

where the initial state $|S\mathbf{Q}, 0\rangle$ consists of an exciton and zero photons, and the final state $|G, 1_{\lambda\mathbf{q}}\rangle$ is the electronic ground state plus one emitted photon with polarization λ and wavevector $\mathbf{q}$; V is the volume of the system. The summation runs over the two photon polarizations and all possible wavevectors $\mathbf{q}$ of the emitted photon, which has energy $\hbar\omega_{\lambda\mathbf{q}}$, while the delta function imposes energy conservation. The transition dipole $\mathbf{p}_S(\mathbf{Q}) = \langle G|\mathbf{p}|S\mathbf{Q}\rangle$ is in general a vector with complex-valued components (in 2D and 1D systems, the

only nonzero components are those in the plane or line containing the material, respectively). In practice, we use the velocity operator and compute the transition dipole as $\mathbf{p}_S(\mathbf{Q}) = (-im/\hbar)\langle G|[\mathbf{x}, H_{\mathrm{KS}}]|S\mathbf{Q}\rangle$ to correctly include the nonlocal part of the Kohn-Sham Hamiltonian, H_{KS} [24]. For light emission, the values of $\mathbf{Q}$ compatible with energy conservation are very small. For this reason, we approximate the dipole of an exciton $|S\mathbf{Q}\rangle$ as $\mathbf{p}_S(\mathbf{Q}) \approx \mathbf{p}_S(0)$ by solving, as is standard, the BSE at $\mathbf{Q} = 0$.

The radiative lifetime at finite temperature T for a given exciton state S can be computed by assuming that the exciton momentum $\mathbf{Q}$ has a thermal equilibrium distribution, which is a good approximation when (as is common) the thermalization process is much faster than radiative recombination [25]. We can thus write the radiative rate of the exciton state S as the thermal average

$$\langle\gamma_S\rangle(T) = \frac{\int d\mathbf{Q}\, e^{-E_S(\mathbf{Q})/k_B T}\,\gamma_S(\mathbf{Q})}{\int d\mathbf{Q}\, e^{-E_S(\mathbf{Q})/k_B T}}. \tag{3.12}$$

The radiative lifetime is defined as the inverse of the radiative rate, $\langle\tau_S\rangle = \langle\gamma_S\rangle^{-1}$. We employ an isotropic effective mass approximation for the exciton dispersion,

$$E_S(\mathbf{Q}) = E_S(0) + \frac{\hbar^2 Q^2}{2M_S}, \tag{3.13}$$

where the exciton mass M_S is approximated as the sum of the electron and hole effective masses, $M_S = m_e^* + m_h^*$. Note that the exciton dispersion and effective mass tensor can also be computed (rather than assumed) by solving the BSE with a finite exciton momentum [26, 27]; this is particularly important in those cases in which a non-parabolic exciton dispersion is expected. For example, Cudazzo *et al.* [28] have shown that in 2D materials, the exciton dispersion can be either linear or parabolic, depending on the character of the exciton wavefunction at finite $\mathbf{Q}$, and Qiu *et al.* [27] have shown that of the two lowest-energy bright excitons in MoS_2, one has a linear and the other a parabolic dispersion. Here we focus on computing the radiative lifetime for excitons with a parabolic dispersion. For completeness, we leave the discussion on these cases to Appendix E while focusing on parabolic dispersion in the main text. In the following, we will assume that the exciton mass is large enough for us to set in the delta functions $E_S(\mathbf{Q}) - \hbar\omega_{\lambda\mathbf{Q}} \approx E_S(0) - \hbar\omega_{\lambda\mathbf{Q}}$.

When only the lowest-energy bright exciton contributes to the photolumi-

nescence, Eq. (3.12) is a good approximation for the radiative rate. When multiple exciton states are occupied, an additional average is needed to include the contributions from all occupied exciton states. Assuming that the exciton states are occupied according to a thermal equilibrium distribution, the effective radiative rate one expects to observe experimentally is:

$$\langle\gamma(T)\rangle_{\text{eff}} = \frac{\sum_S \langle\gamma_S\rangle e^{-E_S(0)/k_B T}}{\sum_S e^{-E_S(0)/k_B T}}. \tag{3.14}$$

Below, we derive the exciton radiative recombination rate as a function of temperature in materials with different dimensionality. The key quantities employed in the derivations, including the coordinates, the exciton momentum $\mathbf{Q}$ and transition dipole $\mathbf{p}_S$, and the photon polarization vectors $\mathbf{e}_{\lambda\mathbf{q}}$, are shown schematically in Fig. 3.2 for each case discussed below. The equations for the bulk and 0D cases are derived here from scratch, while the 2D and 1D cases, which have been previously investigated, are reviewed briefly for completeness.

Bulk (3D) materials

We consider a non-magnetic and non-absorbing[1] anisotropic bulk crystal, in which the static (zero-frequency) dielectric tensor can be written as

$$\boldsymbol{\epsilon}_r = \text{diag}(\epsilon_x, \epsilon_y, \epsilon_z). \tag{3.15}$$

In crystals with cubic, tetragonal, orthorhombic and hexagonal symmetry, we orient the crystallographic axes along the $\{x, y, z\}$ cartesian directions, and in the uniaxial (tetragonal and hexagonal) cases we additionally orient the principal axis along the z direction. In crystal classes with lower symmetry, including monoclinic and triclinic, we orient the principal axes (*i.e.*, the eigenvectors of $\boldsymbol{\epsilon}_r$) along the cartesian directions. With these choices, our treatment is general and can account for any crystal symmetry [29]. The photon energy in such an anisotropic material is modified according to the dielectric tensor. For a given photon wavevector $\mathbf{q} = (q_x, q_y, q_z)$, there are two propagating modes as solutions to Maxwell's equations; they correspond to the two photon polarizations [21], and their frequencies $\omega_{\pm\mathbf{q}}$ are the solutions of Eq. (A.15) in

---

[1]For the sake of studying light emission, this assumption has negligible effects as it amounts to neglecting re-absorption or other dynamical processes of the emitted photons.
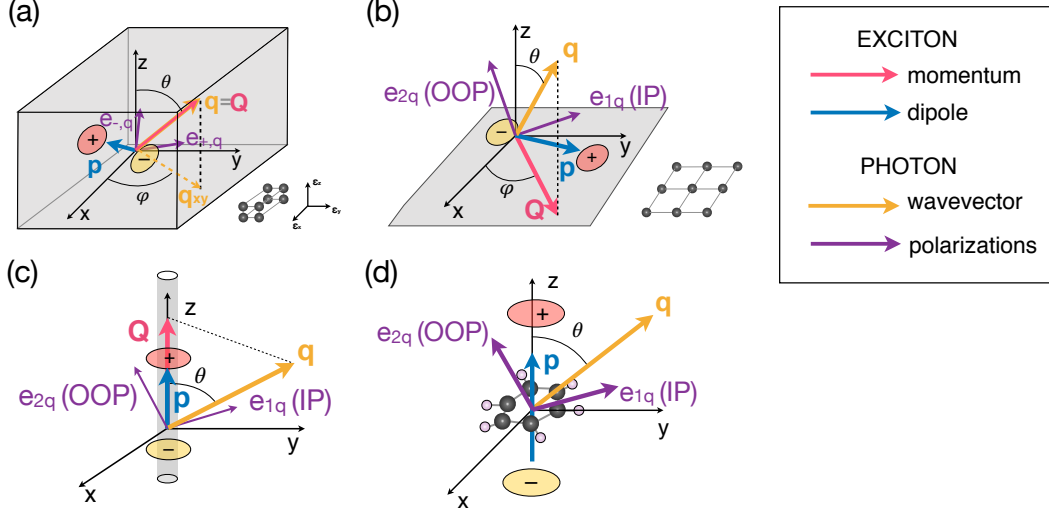
Figure 3.2: **Schematic of the exciton and photon quantities employed in this work.** Each panel corresponds to a different dimensionality. (a) Bulk (three-dimensional) anisotropic material, in which momentum conservation requires $\mathbf{q} = \mathbf{Q}$, and the photon polarizations are nondegenerate and specified by the solution of the Maxwell equations (see Eq. (A.15) in Appendix A). (b) Two-dimensional material, in which the exciton transition dipole $\mathbf{p}_S$ lies in the xy plane containing the material, and the in-plane projection of the emitted photon wavevector equals the exciton momentum, namely $\mathbf{Q} = (\mathbf{q} \cdot \hat{Q})\hat{Q}$. (c) One-dimensional material, where both the exciton momentum and transition dipole lie along the material direction z, and momentum conservation imposes $\mathbf{Q} = \mathbf{q} \cdot \hat{z}$. (d) Isolated (zero-dimensional) system, with no constraints on the exciton momentum, photon wavevector and transition dipoles. In all cases, when the two photon polarizations are degenerate, the polarization vectors $\mathbf{e}_{\lambda\mathbf{q}}$ are chosen as in-plane (IP) and out-of-plane (OOP), where the IP component is in the xy plane and the OOP in the $\mathbf{q} - \hat{z}$ plane.

Appendix A:

$$\omega^2_{\pm\mathbf{q}} = \frac{-\left(\frac{\bar{q}_x^2}{\epsilon_x} + \frac{\bar{q}_y^2}{\epsilon_y} + \frac{\bar{q}_z^2}{\epsilon_z}\right) \pm \tilde{\omega}^2_{\mathbf{q}}}{2\mu_0\epsilon_0}, \tag{3.16}$$

with

$$\tilde{\omega}^2_{\mathbf{q}} = \sqrt{\left(\sum_\alpha \frac{\bar{q}_\alpha^2}{\epsilon_\alpha}\right)^2 - 4q^2 \sum_\alpha \frac{q_\alpha^2 \epsilon_\alpha}{\epsilon_x \epsilon_y \epsilon_z}}, \tag{3.17}$$

where α denotes the cartesian coordinates $\{x, y, z\}$, and $\bar{q}_\alpha^2 = q_\alpha^2 - q^2$. The corresponding polarization vectors for the two modes are

$$\mathbf{e}_{\pm\mathbf{q}} = \frac{1}{\Lambda_q} \begin{pmatrix} q_x(\omega_{\pm\mathbf{q}}^2 \mu_0\epsilon_0\epsilon_x - q^2) \\ q_y(\omega_{\pm\mathbf{q}}^2 \mu_0\epsilon_0\epsilon_y - q^2) \\ q_z(\omega_{\pm\mathbf{q}}^2 \mu_0\epsilon_0\epsilon_z - q^2) \end{pmatrix} \tag{3.18}$$

up to a normalization constant Λ_q; for details, see Appendix A. This solution applies to photons propagating in anisotropic materials with $\epsilon_x \neq \epsilon_y \neq \epsilon_z$. For materials with axial or cubic symmetry, in which, respectively, two or three of the diagonal components of the macroscopic dielectric tensor are equal, the frequencies and polarization vectors have simpler expressions, which can be derived from the general case discussed here.

For an exciton in state $|S\mathbf{Q}\rangle$ with momentum $\mathbf{Q} = (Q_x, Q_y, Q_z)$, we obtain the radiative recombination rate by applying Fermi's Golden rule (see Eq. (3.11)). Momentum conservation fixes the emitted photon wavevector to $\mathbf{q} = \mathbf{Q}$ (see Fig. 3.2(a)), and the summation over λ adds together the contributions from the $\omega_{\pm\mathbf{q}}$ solutions. As mentioned before, we approximate the transition dipole by evaluating it at $\mathbf{Q} = 0$,

$$\langle G|\mathbf{p}|S(\mathbf{Q})\rangle \approx \langle G|\mathbf{p}|S(0)\rangle = p_{Sx}\hat{\mathbf{x}} + p_{Sy}\hat{\mathbf{y}} + p_{Sz}mat\hat{h}bfz, \tag{3.19}$$

with complex components $p_{S\alpha}$. Using these results, the exciton radiative recombination rate at zero temperature becomes

$$\gamma_S^{3D}(\mathbf{Q}) = \frac{\pi e^2}{\epsilon_0 m^2 V} \sum_{\lambda=\pm} \left| \sum_\alpha \frac{p_{S\alpha} q_\alpha(\omega_{\lambda\mathbf{Q}}^2 \mu_0\epsilon_0\epsilon_\alpha - q^2)}{\Lambda_q} \right|^2 \frac{\delta\left(E_S(\mathbf{Q}) - \hbar\omega_{\lambda\mathbf{Q}}\right)}{\omega_{\lambda\mathbf{Q}}}. \tag{3.20}$$

Next, we specialize our discussion to cubic or isotropic materials with a dielectric constant ϵ, i.e., with dielectric tensor $\boldsymbol{\epsilon}_r = \text{diag}(\epsilon, \epsilon, \epsilon)$. Radiative lifetime calculations for an anisotropic bulk crystal will be presented in Chapter 4. Due to symmetry, in the cubic or isotropic case the two modes in Eq. (3.16) become degenerate, with polarization vectors perpendicular to each other and to the direction of photon propagation. Following a convention we recently used in the 2D case [14], we orient one of the two polarization vectors to lie in the xy plane, and call this vector "in-plane" (IP). The other polarization

vector then has a nonzero z component, and is called "out-of-plane" (OOP). These two polarization vectors can be written in spherical coordinates as

$$\text{IP} \quad : \quad \mathbf{e}_{1\mathbf{q}} = \frac{1}{\sqrt{\epsilon}}(-\sin\varphi, \cos\varphi, 0)$$

$$\text{OOP} \quad : \quad \mathbf{e}_{2\mathbf{q}} = \frac{1}{\sqrt{\epsilon}}(-\cos\theta\cos\varphi, -\cos\theta\sin\varphi, \sin\theta), \qquad (3.21)$$

where θ is the polar and φ the azimuth angle of the photon wavevector $\mathbf{q}$ [see Fig. 3.2(a)]. Substituting in Eq. (3.20), we obtain the radiative rate at zero temperature for cubic or isotropic bulk materials (see Appendix B):

$$\gamma_S^{\text{3D, iso}}(\mathbf{Q}) = \frac{\pi e^2}{\epsilon_0 m^2 V c Q\sqrt{\epsilon}} \left\{ \left| \frac{p_{Sx}Q_y - p_{Sy}Q_x}{Q_{xy}} \right|^2_{\text{IP}} \right.$$

$$\left. + \left| \frac{Q_x p_{Sx} + Q_y p_{Sy}}{Q_{xy}} \frac{Q_z}{Q} - p_{Sz} \frac{Q_{xy}}{Q} \right|^2_{\text{OOP}} \right\} \delta\left(E_S(Q) - \frac{\hbar c Q}{\sqrt{\epsilon}} \right). \quad (3.22)$$

Compared to previous semi-classical formula [30] and the formula presented in a recent work [31] which inappropriately follows method for the single-walled carbon nanotubes, Eq. (3.22) correctly includes the full direction momentum conservation during radiative emission in extensive bulk.

The radiative recombination rate of a given exciton state S at temperature T, for isotropic bulk crystals under the assumption that the exciton momentum has a thermal equilibrium distribution, is obtained using Eq. (3.12) as (see Appendix B)

$$\langle \gamma_S^{\text{3D, iso}} \rangle(T) = \frac{8\sqrt{\pi\epsilon}\, e^2 \hbar p_S^2}{3\epsilon_0 m^2 V E_S(0)^2} \left(\frac{E_S(0)^2}{2M_S c^2 k_B T} \right)^{3/2}, \qquad (3.23)$$

where the exciton energy $E_S(0)$ and the transition dipole $\mathbf{p}_S$ (and $p_S^2 = |\mathbf{p}_S|^2$) are obtained by solving the BSE. The $T^{-3/2}$ temperature dependence of the radiative rate (and thus, the $T^{3/2}$ temperature dependence of the radiative lifetime) is consistent with previous semiempirical theoretical treatments [30] and with low-temperature experimental data [32].

For bulk crystals with a low exciton binding energy (< 0.1 eV), additional thermal effects include exciton dissociation and equilibration with free carriers [25]. This topic has been studied extensively experimentally; the net effect of the coexistence between excitons and carriers is an increase in the radiative

lifetime, which can be important near room temperature and can cause the radiative lifetime to deviate significantly from the $T^{3/2}$ trend [32]. Such coupled exciton-carrier dynamics can be treated with kinetic models, as in Chapter 4, but is still beyond the reach of first-principles calculations.

Two-dimensional materials

Novel 2D semiconductors, such as transition metal dichalcogenides and related layered materials, exhibit unique optical properties and strongly bound excitons that govern their light absorption and emission [33]. We have recently proposed a first-principles approach to compute the radiative lifetime in such 2D materials, as well as its angular and polarization dependence, which gives rise to anisotropic light emission [13, 14]. In our approach, exciton recombination is still described using the Fermi Golden rule in Eq. (3.11). However, due to the lower dimensionality, the transition dipole is restricted to the 2D plane containing the material:

$$\mathbf{p}_S = p_{Sx}\hat{\mathbf{x}} + p_{Sy}\hat{\mathbf{y}}, \tag{3.24}$$

with complex components p_{Sx} and p_{Sy}. Furthermore, since translation symmetry applies only in the plane containing the material, momentum conservation is imposed on the in-plane projection of the emitted photon wavevector, using $(\mathbf{q} \cdot \hat{Q})\hat{Q} = \mathbf{Q}$ [see Fig. 3.2(b)]. Unlike the bulk case, photons are emitted into the vacuum surrounding the 2D material (unless a substrate is present), and thus the emitted photons exhibit two degenerate polarizations. Following the same convention as in the isotropic bulk case, the IP and OOP polarizations are chosen as in Eq. (3.21) with $\epsilon = 1$. Upon integrating over all final photon states, we obtain the radiative recombination rate of an exciton S with momentum $\mathbf{Q}$ in a 2D material at zero temperature [14]:

$$\gamma_S^{2D}(\mathbf{Q}) = \gamma_S^{2D}(0) \cdot \left(\frac{E_S(0)}{\sqrt{E_S^2(Q) - \hbar^2 c^2 Q^2}} \right) \times$$

$$\left\{ \left| -\frac{p_{Sx}}{p_S}\sin\varphi + \frac{p_{Sy}}{p_S}\cos\varphi \right|_{\text{IP}}^2 + \frac{E_S(Q)^2 - \hbar^2 c^2 Q^2}{E_S(Q)^2} \left| \frac{p_{Sx}}{p_S}\cos\varphi + \frac{p_{Sy}}{p_S}\sin\varphi \right|_{\text{OOP}}^2 \right\} \tag{3.25}$$

where $\gamma_S^{2D}(0) = \frac{e^2 p_S^2}{\epsilon_0 m^2 c A E_S(0)}$ is the recombination rate for $\mathbf{Q} = 0$ and A is the area of the system in the xy plane. Note that due to momentum conservation there is an upper limit of Q_0 to the momentum of an exciton that can recom-

bine radiatively; this limit occurs when a photon is emitted in the plane of the material, in which case $E_S(\mathbf{Q}) = \hbar c Q_0$. Excitons with momentum $Q > Q_0$ cannot emit a photon, and their radiative recombination rate vanishes since energy and momentum cannot be simultaneously conserved upon photon emission.

At finite temperature T, the exciton radiative lifetime can be computed by assuming, similar to the bulk case, a parabolic exciton dispersion $E_S(\mathbf{Q}) = E_S(0) + \frac{\hbar^2 Q^2}{2M_S}$, where M_S is an in-plane isotropic exciton effective mass. Taking the thermal average in Eq. (3.12) of the 2D radiative rate in Eq. (3.25), we obtain the radiative lifetime [13]

$$\langle \tau_S^{2D} \rangle (T) = \gamma_S^{2D}(0)^{-1} \times \frac{3}{4} \left(\frac{2M_S c^2 k_B T}{E_S(0)^2} \right). \tag{3.26}$$

A similar formula for radiative lifetime was presented earlier in Ref. [28]. However, the used prefactor is not correct for 2D dimensionality. Eq. (3.26) then corrects this point and was applied in our recent work [13], giving temperature dependent radiative lifetimes in excellent agreement (within $5-10\%$) with experimental results obtained by transient photoluminescence.

One-dimensional materials

Excitons have been studied extensively in 1D materials, and first-principles calculations of exciton radiative lifetimes have been employed to investigate light emission in single-walled carbon nanotubes [12, 34]. Since defects and intertube interactions broaden and wash out the exciton spectrum, measuring exciton lifetimes is challenging in carbon nanotubes, and *ab initio* calculations have provided key microscopic insight into exciton recombination in carbon nanotubes [12].

In a 1D material, such as a nanotube or nanowire, the dimensionality constrains the exciton transition dipole to the direction of the material, which we take to be the z direction. The transition dipole can then be written as $\mathbf{p}_S = p_{Sz}\hat{\mathbf{z}}$, and momentum conservation along the z axis imposes a condition on the emitted photon wavevector, $\mathbf{q} \cdot \hat{\mathbf{z}} = \mathbf{Q}$, for the recombination of an exciton with momentum $\mathbf{Q}$ [see Fig. 3.2(c)]. Using Fermi's Golden rule in Eq. (3.11), the exciton decay rate in a 1D material at zero temperature can

be written as [12]:

$$\gamma_S^{1D}(\mathbf{Q}) = \gamma_S^{1D}(0) \cdot \frac{E_S(\mathbf{Q})^2 - \hbar^2 c^2 Q^2}{E_S(\mathbf{Q})^2}, \tag{3.27}$$

where $\gamma_S^{1D}(0) = \frac{e^2 p_{Sz}^2}{\epsilon_0 m^2 \hbar c^2 L_z}$ and L_z is the length of the system along the z direction. The radiative recombination rate decreases monotonically with Q, and is zero when $Q_0 = E_S(Q_0)/\hbar c$. Similar to the 2D case, $Q = Q_0$ is an upper limit to the exciton momentum for radiative recombination, and excitons with $Q > Q_0$ cannot recombine radiatively and emit light.

The finite temperature radiative rate is computed using the thermal average in Eq. (3.12). Assuming a parabolic exciton dispersion, the exciton radiative lifetime in a 1D material reads

$$\langle \tau_S^{1D} \rangle (T) = \gamma_S^{1D}(0)^{-1} \times \frac{3}{4} \left(\frac{\sqrt{2\pi M_S k_B T}}{E_S(0)/c} \right). \tag{3.28}$$

Using this equation, Spataru *et al.* obtained radiative lifetimes in carbon nanotubes in good agreement with experiment [12].

Atoms, molecules, and other isolated (0D) systems

We refer to an atom, molecule, quantum dot or other isolated light emitter as a 0D system [see Fig. 3.2(d)]. The approach presented here applies to both these isolated emitters and to atoms, ions or other single quantum emitters embedded in an isotropic material. Since there is no translation symmetry, the crystal momentum can be taken to be zero and ignored, and we keep only one quantum number to denote the discrete energy levels. Using these conventions, we write the exciton wavefunction in the Tamm-Dancoff approximation as

$$|S\rangle = \sum_{vc} A_{vc}^S |v\rangle_h |c\rangle_e \tag{3.29}$$

where v and c are quantum numbers associated with occupied and unoccupied orbitals, respectively. In general, when there are no symmetry constraints, the transition dipole is a complex vector, as in Eq. (3.19). When the system is embedded in an isotropic material with dielectric constant ϵ (for the 0D system in vacuum, one should set $\epsilon = 1$), Fermi's Golden rule gives the exciton recombination rate at zero temperature (see Appendix D):

$$\gamma_S^{0D} = \frac{\sqrt{\epsilon} e^2 p_S^2 E_S}{3\pi \epsilon_0 m^2 c^3 \hbar^2}. \tag{3.30}$$

In CGS units, in which $\epsilon_0 = 1/4\pi$, we recover the known result $\gamma_S^{\text{0D}} \propto 4/3\, p_S^2 E_S$ for the radiative rate of an isolated emitter or a defect embedded in a crystal [35], which is also known as the Einstein A coefficient, showing a convergence between semi-classical and quantum mechanics treatments. While the photon is second quantized in our formalism, we reproduce the same formula in [35] where the radiation is treated as electromagnetic wave. Due to the absence of crystal momentum for an isolated emitter, all the excitons satisfying the selection rules with nonzero transition dipole can undergo an optical transition and emit a photon. At finite temperature, since there is no momentum, we take a thermal average only over different exciton states [using Eq. (3.14)], and obtain for the effective radiative recombination rate:

$$\langle \gamma^{\text{0D}}(T) \rangle_{\text{eff}} = \frac{\sqrt{\epsilon}\, e^2}{3\pi \epsilon_0 m^2 c^3 \hbar^2} \frac{\sum_S p_S^2 E_S e^{-E_S/k_B T}}{\sum_S e^{-E_S/k_B T}}. \tag{3.31}$$

3.4 Numerical Calculations

To our knowledge, there are no examples in the literature of *ab initio* calculations of radiative lifetimes in bulk crystals and 0D isolated systems within the BSE framework. We apply our approach to compute from first principles the exciton radiative lifetimes in a bulk isotropic crystal of GaAs and in several small organic molecules in the gas phase.

To compute the radiative lifetimes, we first carry out density functional theory (DFT) calculations with the QUANTUM ESPRESSO code [36], using normconserving pseudopotentials [37] and a plane-wave basis set. We then carry out GW-BSE calculations with the YAMBO code [18], and compute the radiative lifetimes by post-processing the BSE results.

For GaAs, we perform DFT calculations on the relaxed zincblende structure, employing the PBEsol exchange-correlation functional [38]. We use fully relativistic normconserving pseudopotentials generated with Pseudo Dojo [39], and include spin-orbit coupling in all calculations. The BSE is solved on a $30 \times 30 \times 30$ **k**-point grid with a rigid scissor shift applied to the DFT band structure to match the experimental band gap [40]. We use a 6 Ry cutoff for the statically screened Coulomb interaction and the highest four valence
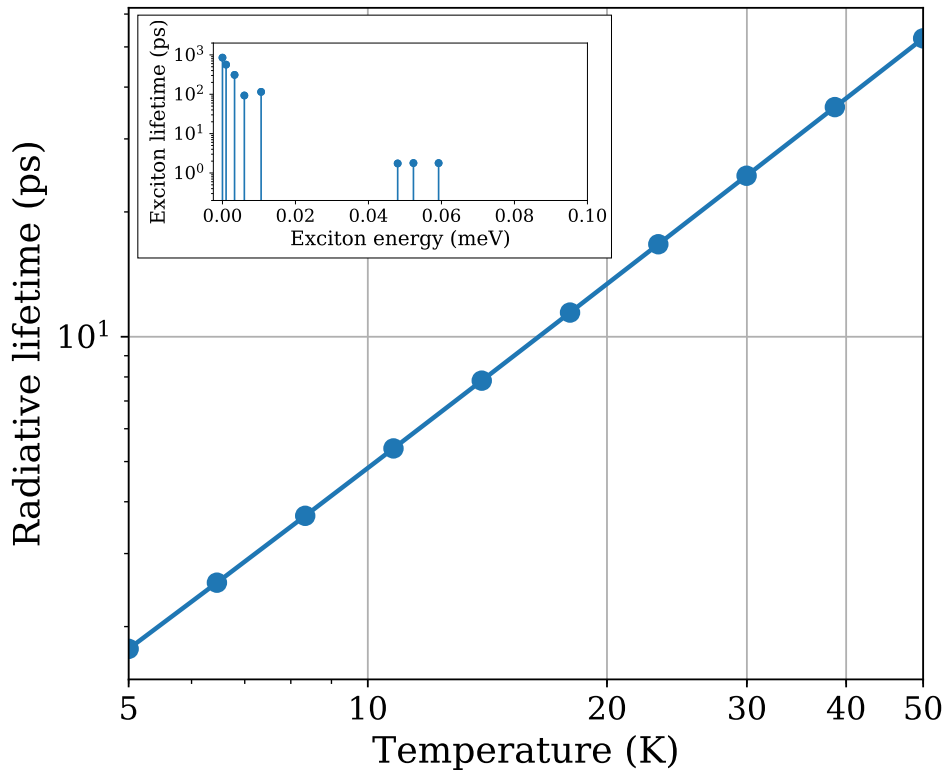
Figure 3.3: **Computed radiative lifetimes in a GaAs crystal.** Shown as a function of temperature up to 50 K. The lifetimes are obtained using the thermal average in Eq. (3.14). The inset shows the excitons contributing to the thermal average along with their individual lifetimes at 10 K. In the inset, the zero of the energy axis is taken to be the lowest exciton energy.

bands and lowest two conduction bands to converge the low-energy excitons. In the radiative lifetime calculations, for higher accuracy we use experimental values for the static dielectric constant and effective masses [40, 41]. Due to the light electron mass, which leads to a steep conduction band valley, fully converging the radiative lifetimes in GaAs requires very fine Brillouin zone grids with prohibitive computational cost. We estimate that the $30 \times 30 \times 30$ **k**-point grid employed here in the BSE calculation allows us to converge the radiative lifetime within a factor of five of its fully converged result with an ideal infinitely dense BZ grid.

The computed radiative lifetimes in GaAs as a function of temperature are shown in Fig. 3.3. They are obtained as the thermal average in Eq. (3.14) of the BSE exciton radiative rates for a bulk isotropic crystal in Eq. (3.23). The

inset of Fig. 3.3 shows the low-energy excitons contributing to this thermal average; the lowest five excitons are dark and associated with spin-forbidden transitions, and the three bright excitons at a slightly higher energy also contribute to the average. The dark states increase the average radiative lifetime by an order of magnitude compared to the average lifetime of the bright excitons alone.

The computed BSE radiative lifetimes are of order $1-50$ ps below 50 K, and exhibit the $T^{3/2}$ trend expected for bulk crystals at low temperature [32]. Comparing these results with experiment is not simple. In GaAs, the radiative processes are known to be affected by the coupling of excitons with phonons and free electron-hole pairs, resulting in an intricate nonequilibrium dynamics that is still the subject of debate [42–44]. The interaction with phonons is particularly important in GaAs, where exciton-phonon scattering is thought to provide the momentum needed by excitons to transition toward the radiative region [42, 43]. For this reason, the photoluminescence decay is expected to be much slower than the intrinsic exciton radiative lifetimes computed here. Consistent with this view, the measured photoluminescence decay times are a few ns at low temperatures [42–44], while our computed radiative lifetimes are a few ps in the same temperature range. This result confirms that the long lifetimes observed in GaAs by measuring the photoluminescence decay are the result of nonequilibrium exciton dynamics rather than an intrinsic exciton lifetime. Future work will investigate the coupled nonequilibrium dynamics of excitons and phonons, which will enable quantitative comparisons with photoluminescence data.

We additionally computed the radiative lifetimes in four small organic molecules − fluorobenzene, ethylene, thiophene and toluene. The computed radiative lifetimes, which are discussed in detail in Ref. [45], are within a factor of $\sim$2 of the measured values, and thus in excellent agreement with experiment. This result shows that the theoretical framework presented in this thesis can be adapted to investigating light emission at localized defects or ions and dopants, a topic of current interest for light emission and quantum technologies.

3.5 Conclusions

In summary, we present a general approach based on DFT and the *ab initio* BSE method to compute the radiative lifetimes in bulk crystals, 2D and 1D materials, and in 0D or isolated systems such as a molecule, quantum dot or single quantum emitter. Our radiative lifetime calculations are in practice a simple post-processing of BSE results that only adds a small computational overhead. The temperature dependence of the exciton radiative lifetime at low temperature is predicted to be proportional to $T^{3/2}$ in bulk, T in 2D and $T^{1/2}$ in 1D materials. The bulk crystal treatment is applied to an important III-V semiconductor − a GaAs crystal − where our computed intrinsic radiative lifetimes are shorter than the values measured by photoluminescence, but consistent with their interpretation in terms of nonequilibrium dynamics of excitons coupled to phonons and free carriers. Our work provides a framework for predicting the *intrinsic* exciton radiative lifetimes in materials with any dimensionality. Since the BSE is considered a gold standard for computing optical absorption and excitons [46], it is expected to also provide accurate results for radiative processes and light emission. These calculations can provide a benchmark for materials in which extrinsic effects due to impurities or interfaces dominate the ultrafast dynamics, such as layered semiconducting devices. They can also guide the interpretation of ultrafast spectroscopy measurements and the discovery of new quantum and solid-state emitters with long radiative lifetimes.

References

[1] R. S. Knox, *Theory of excitons (solid state phys. suppl. 5)*, Vol. 5 (Academic, 1963).

[2] Y. Park, C. Litton, T. Collins, and D. Reynolds, "Exciton spectrum of zno", Phys. Rev. **143**, 512 (1966).

[3] V. Agranovich and O. Dubovskii, *Effect of retarded interaction on the exciton spectrum in one-dimensional and two-dimensional crystals* (Springer, 1995), pp. 795–798.

[4] R. D. Schaller, V. M. Agranovich, and V. I. Klimov, "High-efficiency carrier multiplication through direct photogeneration of multi-excitons via virtual single-exciton states", in , Vol. 1, 3 (Nature Publishing Group, 2005), p. 189.

[5] O. V. Mikhnenko, P. W. Blom, and T.-Q. Nguyen, "Exciton diffusion in organic semiconductors", Energy Environ. Sci. **8**, 1867–1888 (2015).

[6] B. K. Ridley, *Quantum processes in semiconductors* (Oxford University Press, 2013).

[7] P. T. Landsberg, *Recombination in semiconductors* (Cambridge University Press, 1992).

[8] L. C. Andreani, F. Tassone, and F. Bassani, "Radiative lifetime of free excitons in quantum wells", Solid State Commun. **77**, 641–645 (1991).

[9] J. Proot, C. Delerue, and G. Allan, "Electronic structure and optical properties of silicon crystallites: application to porous silicon", Appl. Phys. Lett. **61**, 1948–1950 (1992).

[10] E. Kioupakis, Q. Yan, D. Steiauf, and C. G. Van de Walle, "Temperature and carrier-density dependence of auger and radiative recombination in nitride optoelectronic devices", New J. Phys. **15**, 125006 (2013).

[11] X. Zhang, J.-X. Shen, W. Wang, and C. G. Van de Walle, "First-principles analysis of radiative recombination in lead-halide perovskites", ACS Energy Lett. **3**, 2329–2334 (2018).

[12] C. D. Spataru, S. Ismail-Beigi, R. B. Capaz, and S. G. Louie, "Theory and ab initio calculation of radiative lifetime of excitons in semiconducting carbon nanotubes", Phys. Rev. Lett. **95**, 247402 (2005).

[13] M. Palummo, M. Bernardi, and J. C. Grossman, "Exciton radiative lifetimes in two-dimensional transition metal dichalcogenides", Nano Lett. **15**, 2794–2800 (2015).

[14] H.-Y. Chen, M. Palummo, D. Sangalli, and M. Bernardi, "Theory and ab initio computation of the anisotropic light emission in monolayer transition metal dichalcogenides", Nano Lett. **18**, 3839–3843 (2018).

[15] G. Strinati, "Effects of dynamical screening on resonances at inner-shell thresholds in semiconductors", Phys. Rev. B **29**, 5718 (1984).

[16] M. Rohlfing and S. G. Louie, "Electron-hole excitations and optical spectra from first principles", Phys. Rev. B **62**, 4927 (2000).

[17] A. L. Fetter and J. D. Walecka, *Quantum theory of many-particle systems* (Courier Corporation, 2012).

[18] A. Marini, C. Hogan, M. Grüning, and D. Varsano, "Yambo: an ab initio tool for excited state calculations", Comput. Phys. Commun. **180**, 1392–1403 (2009).

[19] X. Gonze, F. Jollet, F. A. Araujo, D. Adams, B. Amadon, T. Applencourt, C. Audouze, J.-M. Beuken, J. Bieder, A. Bokhanchuk, et al., "Recent developments in the abinit software package", Comput. Phys. Commun. **205**, 106–131 (2016).

[20] J. Deslippe, G. Samsonidze, D. A. Strubbe, M. Jain, M. L. Cohen, and S. G. Louie, "Berkeleygw: a massively parallel computer package for the calculation of the quasiparticle and optical properties of materials and nanostructures", Comput. Phys. Commun. **183**, 1269–1289 (2012).

[21] R. J. Glauber and M. Lewenstein, "Quantum optics of dielectric media", Phys. Rev. A **43**, 467 (1991).

[22] D. Kumar, "Photon states in anisotropic media", Pramana **59**, 329–336 (2002).

[23] R. Loudon, *The quantum theory of light* (OUP Oxford, 2000).

[24] D. Sangalli, J. Berger, C. Attaccalite, M. Grüning, and P. Romaniello, "Optical properties of periodic systems within the current-current response framework: pitfalls and remedies", Phys. Rev. B **95**, 155203 (2017).

[25] J. P. Wolfe, "Thermodynamics of excitons in semiconductors", Phys. Today **35**, 46–54 (1982).

[26] M. Gatti and F. Sottile, "Exciton dispersion from first principles", Phys. Rev. B **88**, 155113 (2013).

[27] D. Y. Qiu, T. Cao, and S. G. Louie, "Nonanalyticity, valley quantum phases, and lightlike exciton dispersion in monolayer transition metal dichalcogenides: theory and first-principles calculations", Phys. Rev. Lett. **115**, 176801 (2015).

[28] P. Cudazzo, C. Attaccalite, I. V. Tokatly, and A. Rubio, "Strong charge-transfer excitonic effects and the bose-einstein exciton condensate in graphane", Phys. Rev. Lett. **104**, 226804 (2010).

[29] R. E. Newnham, *Properties of materials: anisotropy, symmetry, structure* (Oxford University Press, 2005), p. 67.

[30] G. Lasher and F. Stern, "Spontaneous and stimulated recombination radiation in semiconductors", Phys. Rev. **133**, A553–A563 (1964).

[31] L. Hu, C. Xu, L. Peng, F. L. Gu, and W. Yang, "Photocatalytic activity and the radiative lifetimes of excitons via an ab initio approach", J. Mater. Chem. A **6**, 15027–15032 (2018).

[32] J. Im, A. Moritz, F. Steuber, V. Härle, F. Scholz, and A. Hangleiter, "Radiative carrier lifetime, momentum matrix element, and hole effective mass in gan", Appl. Phys. Lett. **70**, 631–633 (1997).

[33] M. Bernardi, C. Ataca, M. Palummo, and J. C. Grossman, "Optical and electronic properties of two-dimensional layered materials", Nanophotonics **6**, 479–493 (2017).

[34] P. Avouris, M. Freitag, and V. Perebeinos, "Carbon-nanotube photonics and optoelectronics", Nat. Photon. **2**, 341 (2008).

[35]D. Dexter, "Theory of the optical properties of imperfections in nonmetals", in *Advances in research and applications*, Vol. 6, edited by F. Seitz and D. Turnbull, Solid State Physics (Academic Press, 1958), pp. 353–411.

[36]P. Giannozzi, S. Baroni, N. Bonini, M. Calandra, R. Car, C. Cavazzoni, D. Ceresoli, G. L. Chiarotti, M. Cococcioni, I. Dabo, et al., "Quantum espresso: a modular and open-source software project for quantum simulations of materials", J. Phys. Condens. Matter. **21**, 395502 (2009).

[37]N. Troullier and J. L. Martins, "Efficient pseudopotentials for plane-wave calculations", Phys. Rev. B **43**, 1993–2006 (1991).

[38]J. P. Perdew, A. Ruzsinszky, G. I. Csonka, O. A. Vydrov, G. E. Scuseria, L. A. Constantin, X. Zhou, and K. Burke, "Restoring the density-gradient expansion for exchange in solids and surfaces", Phys. Rev. Lett. **100**, 136406 (2008).

[39]M. van Setten, M. Giantomassi, E. Bousquet, M. Verstraete, D. Hamann, X. Gonze, and G.-M. Rignanese, "The pseudodojo: training and grading a 85 element optimized norm-conserving pseudopotential table", Comput. Phys. Commun. **226**, 39–54 (2018).

[40]M. Levinshtein and S. Rumyantsev, "Galliumarsenide (gaas)", in *Handbook series on semiconductor parameters: volume 1: si, ge, c (diamond), gaas, gap, gasb, inas, inp, insb* (World Scientific, 1996), pp. 77–103.

[41]A. Dargys and J. Kundrotas, *Handbook on physical properties of ge, si, gaas and inp* (Science and Encyclopedia Publ., 1994).

[42]G. W. 't Hooft, W. A. J. A. van der Poel, L. W. Molenkamp, and C. T. Foxon, "Giant oscillator strength of free excitons in gaas", Phys. Rev. B **35**, 8281–8284 (1987).

[43]M. Gurioli, P. Borri, M. Colocci, M. Gulia, F. Rossi, E. Molinari, P. E. Selbmann, and P. Lugli, "Exciton formation and relaxation in gaas epilayers", Phys. Rev. B **58**, R13403–R13406 (1998).

[44]M. Beck, J. Hübner, M. Oestreich, S. Bieker, T. Henn, T. Kiessling, W. Ossau, and L. W. Molenkamp, "Thermodynamic origin of the slow free exciton photoluminescence rise in gaas", Phys. Rev. B **93**, 081204 (2016).

[45]H.-Y. Chen, V. A. Jhalani, M. Palummo, and M. Bernardi, "Ab initio calculations of exciton radiative lifetimes in bulk crystals, nanostructures and molecules", *Submitted.* arXiv preprint arXiv:1901.08747 (2019).

[46]D. Jacquemin, I. Duchemin, and X. Blase, "Is the bethe–salpeter formalism accurate for excitation energies? comparisons with td-dft, caspt2, and eomccsd", J. Phys. Chem. Lett. **8**, 1524–1529 (2017).

Chapter 4

FIRST-PRINCIPLES EXCITON RADIATIVE LIFETIMES IN GALLIUM NITRIDE

The content of this chapter is taken from the following work:

[1]V. A. Jhalani, H.-Y. Chen, M. Palummo, and M. Bernardi, "First-principles exciton radiative lifetimes in bulk GaN", *Submitted.* (2019).

4.1 Introduction

The ultrafast recombination dynamics play a key role in determining the radiative properties of GaN and GaN-based light emitting devices. Even though the exciton binding energy is rather weak in GaN (of order 10 meV), it is well known that accurately computing the absorption spectrum in GaN and other III-V semiconductors requires taking into account excitonic effects. One expects that predicting light emission properties and radiative lifetime similarly requires taking into account the bound states of electron-hole pairs (*i.e.*, the excitons) rather than just studying the recombination of independent electron-hole pairs. A complete understanding of the microscopic processes regulating exciton dynamics and their intrinsic radiative lifetimes is necessary to guide the design of devices. Spectroscopically determined exciton radiative properties are the subject of debate, due to both differences in experimental setups and type of experiments employed and because sample purity and quality affect the competing non-radiative processes that determine exciton dynamics [1]. As such, there is a strong need for accurate, *intrinsic* calculations of excitonic and radiative properties in GaN and related III-nitride materials, which can be used as benchmark for interpreting photoluminescence measurements and can guide microscopic understanding and device design.

First-principles calculations of radiative rates in bulk materials, including GaN, have existed for decades, but they typically neglect key factors like electron-hole interactions, the material anisotropy, the dynamical screening, or temperature dependence dictated by dimensionality [2, 3]. These elements are especially important when considering a material like GaN in which the

screening of the Coulomb interaction is relatively weak. In Chapter 3 we have developed a framework for computing radiative lifetimes in isotropic bulk materials for the first time. However, since GaN and related III-nitrides have a hexagonal wurtzite structure, their properties are anisotropic; the material is isotropic in the hexagonal basal plane, but the properties along c-axis direction are different. As a result, the approach presented in Chapter 3 for computing radiative lifetimes in isotropic material needs to be extended to uniaxial materials, namely in-plane isotropic materials, as with GaN.

Here, we extend to a material with hexagonal symmetry the approach for computing excitonic radiative recombination rates presented in Chapter 3, and derive the equation for the temperature dependent radiative lifetime within the *ab initio* BSE framework for the case of a uniaxial bulk crystal. We apply this scheme to wurtzite GaN, computing excitonic radiative lifetimes from first principles in a uniaxial bulk material for the first time. Our computed radiative lifetimes are in very good agreement (within a factor of two) with experiment. We also analyze the radiative lifetimes at low temperature regime where the intrinsic radiative lifetime dominates in experimental data and where the importance of including spin-orbit coupling (SOC) is essential to obtaining accurate intrinsic radiative lifetimes; a surprising result given that SOC is weak in GaN. We also investigate the high temperature regime in which the thermal equilibrium between bound excitons and free carriers raises the lifetimes significantly from the intrinsic value in experimental results. We develop a thermal exciton dissociation model to include exciton dissociation in our calculations and validate it against experimental results.

4.2   Theory and Methods

Theoretical Framework

The BSE framework we employ for computing radiative lifetimes from first principles is discussed in detail in Chapter 3, including the derivation for the bulk isotropic case. Here, we briefly review the approach and specific details relevant to a bulk anisotropic system. Similar to our discussion above, we apply the Tamm-Dancoff approximation and represent an exciton as a superposition of non-interacting electron-hole states as in Eq. (3.1). The radiative recombination rate for an exciton at zero temperature is given by Fermi's golden rule,

which we derive for the minimal electron-photon coupling Hamiltonian after second-quantizing the photons in a dielectric medium using Eq (3.11). As before, since the values of $\mathbf{Q}$ compatible with energy conservation for light emission are small, we approximate the dipole of an exciton $|S\mathbf{Q}\rangle$ as $\mathbf{p}_S(\mathbf{Q}) \approx \mathbf{p}_S(0)$ by solving the BSE at $\mathbf{Q} = 0$, as is standard. We still assume that the exciton momentum $\mathbf{Q}$ is in a thermal distribution, and thus that the radiative rate of an exciton S at finite temperature T is given by the thermal average in Eq. (3.12).

We then employ a 3D anisotropic effective mass approximation for the exciton dispersion,

$$E_S(\mathbf{Q}) = E_S(0) + \frac{\hbar^2}{2}\left(\frac{Q_x^2 + Q_y^2}{M_{xy}} + \frac{Q_z^2}{M_z}\right), \tag{4.1}$$

where the M_{xy} and M_z are the in-plane and out-of-plane exciton masses, respectively. As before, in the following we assume that the exciton mass is large enough to use the approximation $E_S(\mathbf{Q}) - \hbar\omega_{\lambda\mathbf{q}} \approx E_S(0) - \hbar\omega_{\lambda\mathbf{q}}$ in the delta functions of Eq. (3.11).

As is the case for wurtzite-GaN, we consider an anisotropic bulk crystal in which the static dielectric tensor can be written as

$$\epsilon_r = \text{diag}(\epsilon_{xy}, \epsilon_{xy}, \epsilon_z). \tag{4.2}$$

In the following, we orient the principal crystal axis along the z direction. For a given photon wavevector $\mathbf{q} = (q_x, q_y, q_z)$, there are two propagating modes as solutions to Maxwell's equations, each corresponding to one of the two photon polarizations [4]. Their frequencies are obtained by solving the equation of motion obtained from second quantizing Maxwell's equation in the dielectric material (see the derivation in Chapter 3). The two solutions for the uniaxial case are:

$$\frac{\omega_{\text{IP}}}{c} = \sqrt{\frac{q^2}{\epsilon_{xy}}}, \quad \mathbf{e}_{\text{IP}} = \frac{1}{\sqrt{\epsilon_{xy}}}\left(\frac{q_y}{q_{xy}}, -\frac{q_y}{q_{xy}}, 0\right) \tag{4.3}$$

and

$$\frac{\omega_{\text{OOP}}}{c} = \sqrt{\frac{\epsilon_{xy}q_{xy}^2 + \epsilon_z q_z^2}{\epsilon_{xy}\epsilon_z}} \tag{4.4}$$

with

$$\mathbf{e}_{\text{OOP}} =$$

$$\left(\frac{q_x}{q_{xy}} \sqrt{\frac{1/\epsilon_{xy}}{\left(1 + \frac{\epsilon_{xy}q_{xy}^2}{\epsilon_z q_z^2}\right)}}, \frac{q_y}{q_{xy}} \sqrt{\frac{1/\epsilon_{xy}}{\left(1 + \frac{\epsilon_{xy}q_{xy}^2}{\epsilon_z q_z^2}\right)}}, -\sqrt{\frac{1/\epsilon_z}{\left(1 + \frac{\epsilon_z q_z^2}{\epsilon_{xy}q_{xy}^2}\right)}} \right) \quad (4.5)$$

where c is the speed of light and we use the shorthand notation $q_{xy}^2 = q_x^2 + q_y^2$. We call the first solution the "in-plane" (IP) mode since its polarization vector sits in the xy-plane. Given that the plane is isotropic, this solution is identical to the IP mode for the 2D and isotropic 3D cases in Ref. [5] and Chapter 3. We call the second solution the "out-of-plane" (OOP) mode, which sees the anisotropy of the material and has a more complicated expression than the isotropic case.

For an exciton $|S\mathbf{Q}\rangle$ with momentum $\mathbf{Q} = (Q_x, Q_y, Q_z)$ we obtain the radiative rate by substituting the two photon polarization solutions and their respective frequencies [see Eqs. (4.3) - (4.5)] into Eq. (3.11). As in the bulk isotropic case, momentum conservation fixes the emitted photon wavevector to $\mathbf{q} = \mathbf{Q}$, and the summation over λ adds together the contributions from the IP and OOP solutions. As mentioned earlier, we approximate the transition dipole at $\mathbf{Q} = 0$ and expand it into complex components, $\mathbf{p}_S(\mathbf{Q}) \approx \mathbf{p}_S(0) = p_{Sx}\hat{\mathbf{x}} + p_{Sy}\hat{\mathbf{y}} + p_{Sz}\hat{\mathbf{z}}$. Using these results, we obtain the radiative rate at zero temperature for a uniaxial bulk material:

$$\gamma_S^{\text{3D,aniso}}(\mathbf{Q}) = \frac{\pi e^2}{\epsilon_0 m^2 V} \left[\frac{\sqrt{\epsilon_{xy}}}{cQ} \left| \frac{1}{\sqrt{\epsilon_{xy}}} \frac{p_{Sx}Q_y - p_{Sy}Q_x}{Q_{xy}} \right|_{\text{IP}}^2 \delta\left(E_S(Q) - \frac{\hbar c Q}{\sqrt{\epsilon_{xy}}}\right) \right.$$

$$+ \frac{\sqrt{\epsilon_{xy}\epsilon_z}}{c\sqrt{\epsilon_{xy}Q_{xy}^2 + \epsilon_z Q_z^2}} \left| \frac{Q_x p_{Sx} + Q_y p_{Sy}}{Q_{xy}} \sqrt{\frac{1/\epsilon_{xy}}{1 + \frac{\epsilon_{xy}Q_{xy}^2}{\epsilon_z Q_z^2}}} - p_{Sz}\sqrt{\frac{1/\epsilon_z}{1 + \frac{\epsilon_z Q_z^2}{\epsilon_{xy}Q_{xy}^2}}} \right|_{\text{OOP}}^2$$

$$\left. \times \delta\left(E_S(Q) - \frac{\hbar c\sqrt{\epsilon_{xy}Q_{xy}^2 + \epsilon_z Q_z^2}}{\sqrt{\epsilon_{xy}\epsilon_z}}\right) \right] \quad (4.6)$$

where $Q_{xy}^2 = Q_x^2 + Q_y^2$. The radiative recombination rate of an exciton S at finite temperature T in a uniaxial bulk crystal is then obtained by performing the thermal average in Eq. (3.12) using the effective mass approximation of

Eq. (4.1). We obtain (see Appendix C):

$$
\left\langle \gamma_S^{\text{3D,aniso}} \right\rangle (T) = \frac{\sqrt{\pi \epsilon_{xy}} e^2 \hbar \left[\left(\frac{2\epsilon_z}{3\epsilon_{xy}} + 2 \right) \left(p_{Sx}^2 + p_{Sy}^2 \right) + \frac{8}{3} p_{Sz}^2 \right]}{\epsilon_0 m^2 V E_S(0)^2}
$$
$$
\times \left(\frac{E_S(0)^2}{2 \sqrt[3]{M_{xy}^2 M_z} c^2 k_B T} \right)^{3/2} \quad (4.7)
$$

where the exciton energies $E_S(0)$ and the transition dipole components $p_{S\alpha}$ are obtained by solving the BSE. The exciton masses M_{xy} and M_z are approximated as the sum of the corresponding electron and hole effective masses *i.e.*, $M_z = m_{e_z}^* + m_{h_z}^*$. In GaN, we find from the BSE that the lowest exciton states are composed of transitions from the two heavy hole bands. We thus approximate the hole mass as the average of the two heavy hole masses, which we estimate from the GW quasiparticle band structure dispersion (see Computational Details in Sec. 4.2). By setting $\epsilon_z = \epsilon_{xy}$ and $M_{xy} = M_z$, one can recover the radiative rate for the bulk isotropic case in Eq. (3.23). Notably, we obtain again the $T^{-3/2}$ temperature dependence of the radiative rate (and therefore the $T^{3/2}$ dependence of the radiative lifetime) that is expected for a thermal exciton distribution in a bulk material (obtained in Chapter 3), consistent with previous semiempirical theoretical treatments [6].

Note also that Eq. (4.7) is a good approximation for the radiative rate when only the lowest-energy bright excitons contribute to the photoluminescence. We again take the additional thermal everage given in Eq. (3.14) to take into account that multiple exciton states are occupied, including dark states with small transition dipoles, as is the case in GaN.

Computational Details

We carry out *ab initio* calculations on a GaN unit cell in the wurtzite structure with relaxed lattice parameters. The ground state properties and electronic wavefunctions are calculated using density functional theory (DFT) with the QUANTUM ESPRESSO code [7]. For excitonic and optical properties, we start with DFT within the generalized gradient approximation [8]. Fully relativistic norm-conserving pseudopotentials [9, 10] generated by Pseudo Dojo [11] are employed, in which the shells treated as valence are the $3s$, $3p$, $3d$, $4s$, and $4f$ for Ga and the $2s$ and $2p$ for N. A non-linear core correction (NLCC)

[12] is included for all remaining core shells for both atoms. Using the Yambo code [13], the BSE is solved on a $24 \times 24 \times 18$ **k**-point grid after applying a scissor shift and stretch of the DFT eigenvalues to obtain quasiparticle energies consistent with GW (see below). We use a 6 Ry cutoff for the screened Coulomb interactions and the highest 6 valence bands and lowest 4 conduction bands to converge the low-energy exciton energies and transition dipoles.

The static dielectric tensor is computed using Yambo within the independent particle approximation on the same grid as the BSE. We converge the exciton binding energy by computing it with various **k**-point grids from $12 \times 12 \times 9$ to $24 \times 24 \times 18$ and extrapolating it to a vanishingly small **k**-point distance (*i.e.*, to an an infinitely dense grid) [14]. We find a converged binding energy of 19.7 meV, in excellent agreement with the experimental value of 20.4 meV [15].

For the quasiparticle band structure, to obtain scissor and stretch parameters and effective masses, we start with DFT within the local-density approximation [16] and employ scalar-relativistic norm-conserving pseudopotentials for both Ga and N. The $4s$ and $4p$ shells are treated as valence for Ga, and the $2s$ and $2p$ for N. The NLCC is included to account for the $3d$ core states in Ga. The *GW* self-energy is computed using the Yambo code, and employed to correct the LDA quasiparticle energies. Consistent with previous works [17], we employ the "one-shot" G_0W_0 approximation [18], a plasmon-pole model for the dielectric function in the self-energy, a 25 Ry cutoff energy for the dielectric matrix, 300 empty bands, and a $14 \times 14 \times 10$ **k**-point grid.

4.3 Results

We compute the radiative lifetimes in bulk wurtzite GaN using the thermal average in Eq. (3.14) of the exciton radiative rate for a uniaxial bulk anisotropic crystal given in Eq. (4.7). We first focus our discussion on the radiative lifetimes in the low temperature regime, where comparison with experimental data is straightforward. Our computed radiative lifetimes as a function of temperature from 50 to 150 K are shown in Fig. 4.1 along with experimental photoluminescence (PL) measurements from Ref. [19]. In this temperature range, our first-principles radiative lifetimes, with SOC included, are of order 200-900 ps and are in very good agreement (within a factor of two) with the
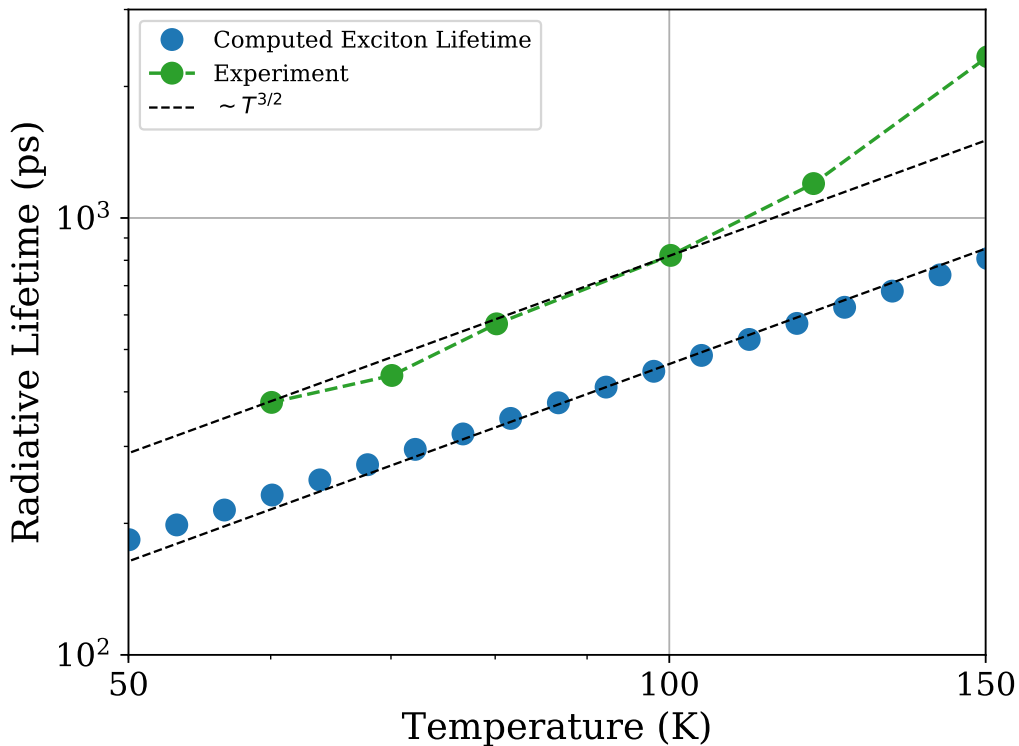
Figure 4.1: **Low temperature GaN radiative lifetime.** Comparison of our computed radiative lifetimes (blue) against experimental results from Ref. [19] (green) in a bulk wurtzite GaN crystal as a function of temperature up to 150 K. The lifetimes are obtained using the thermal average in Eq. (3.14) of excitonic radiative rates as given by Eq. (4.7) with SOC included. The black dashed lines represent the $T^{3/2}$ trend expected in the low temperature regime for both set of lifetimes.

experimental results. Our computed results additionally exhibit the $T^{3/2}$ trend expected for bulk crystals at low temperature as predicted by our theoretical treatment and observed in the experimental results.

As seen in Fig. 4.2, including SOC when computing the excitonic states increases the radiative lifetimes by a factor of $2-3$ and significantly improves the agreement with experimental results. Though SOC is weak in GaN $-$ the induced splitting at the Γ-point is roughly 5 meV in our calculations $-$ its inclusion is crucial for obtaining accurate excitonic states. The inset in Fig. 4.2 shows the individual radiative lifetimes and relative energies of the low-energy excitons contributing to the thermal average, for both the cases where SOC is included and neglected in the BSE. Without SOC, the exciton structure
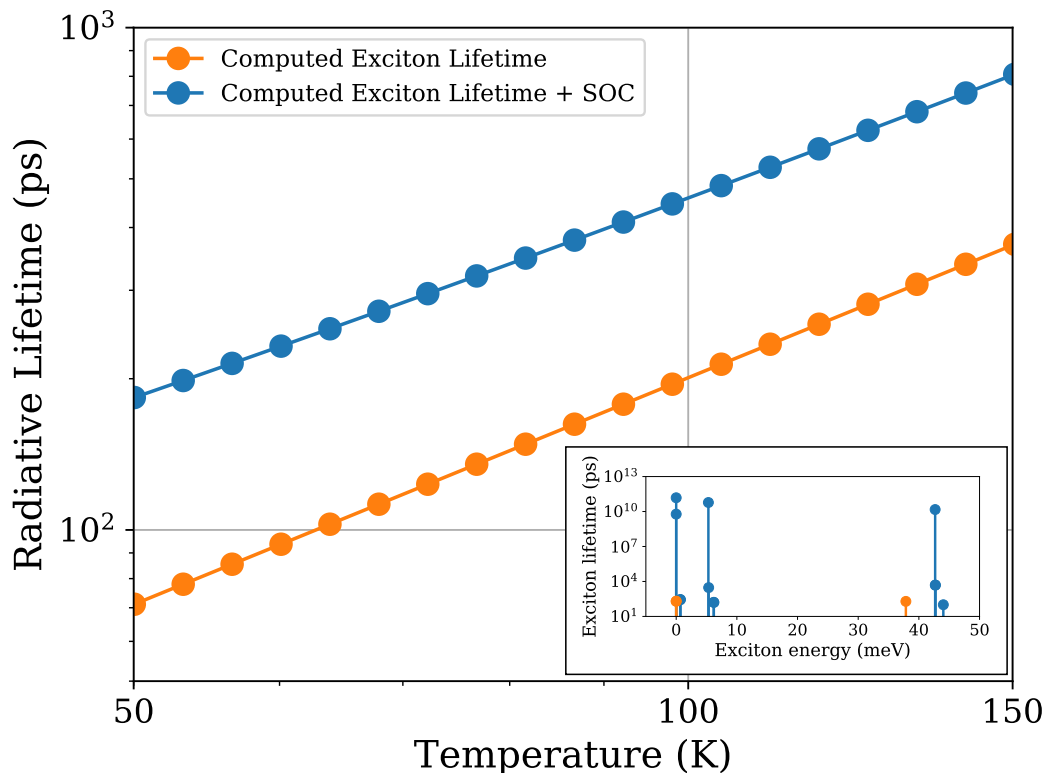
Figure 4.2: **Effect of including SOC in calculations of radiative lifetime in GaN.** Comparison of computed radiative lifetimes in a bulk wurtzite GaN crystal as a function of temperature for when the BSE is solved with SOC neglected (orange) and included (blue). The inset shows the excitons contributing to the thermal average along with their individual lifetimes at 100 K, with (blue) and without (orange) SOC. In the inset, the zero of the energy axis is taken to be the lowest exciton energy for each case.

consists of three bright excitons, two of which are degenerate. The lifetimes of all three exciton states are roughly identical, and their value determines the radiative lifetime for the calculation without SOC. The inclusion of SOC splits each exciton into four new states by doubling the number of valence and conduction states that compose the electron-hole pair basis states of the exciton. Some of these new states, which have lifetimes up to $7 - 11$ orders of magnitude longer than the excitons found without SOC, are dark states due to spin-forbidden transitions. When included in the thermal averge, these dark states increase the radiative lifetime compared to the average lifetime of the bright excitons alone. Therefore, the inclusion of SOC reveals important low-energy dark states in the excitonic spectrum that need to be taken into account in order to obtain an accurate radiative lifetime, even when SOC is

weak per se, as in GaN.

At higher temperature, the excitons may dissociate into free electrons and holes, which mainly recombine non-radiatively via defects in GaN, giving rise to a lower radiative recombination rate [19, 20]. This effect is observed as an increase in the radiative lifetime as a function of temperature at a rate greater than the intrinsic $T^{3/2}$ trend at temperatures above $100 - 150$ K. To account for the interactions between excitons and free carriers, since the radiative rate is much longer than the thermalization rate, we assume that bound excitons and free carriers are in thermal equilibrium and the carrier densities are given by the mass-action law [21]

$$\frac{n_e n_h}{n_x} = \frac{[n_0 + \delta n]\delta p}{\delta n_x} = n^*(T), \tag{4.8}$$

where n_e, n_h, and n_x are the free electron, hole, and exciton densities, respectively. n_0 is the background free electron density, and δn, δp, and δn_x are the excited (e.g. via optical pump) electron, hole, and exciton densities, respectively. Here, $n^*(T)$ is given by

$$n^*(T) = 2 \left(\frac{m_{red} k_B T}{2\pi \hbar^2} \right)^{3/2} e^{-E_b/k_B T}, \tag{4.9}$$

where $m_{red} = m_h m_e/(m_h + m_e)$ is the reduced mass of the exciton and E_b is the exciton binding energy.

Typically, the optically pumped excited electrons and hole densities, which are of order 10^{13} cm^{-3} [1], are much smaller than the sample donor concentrations, which are of order 10^{16} cm^{-3}. We assume that the extrinsic carrier concentration introduced by the donors dominates over the intrinsic electron density [19, 22]. Thus, since $\delta n \sim \delta p << n_0$, we have from Eq. 4.8 that $\delta n/\delta n_x = n^*(T)/n_0$. Assuming that the relative probabilities of recombination for free carriers and excitons are proportional to their respective densities, $P_{\text{carrier}}/P_{\text{exciton}} = \delta n/\delta n_x$, and using $P_{\text{carrier}} + P_{\text{exciton}} = 1$, we can obtain the probabilities for excitonic and free carrier recombination. The measured radiative rate will be a weighted average of the rates of the two recombination processes: $\Gamma_{\text{rad}} = \Gamma_{\text{carrier}} P_{\text{carrier}} + \Gamma_{\text{exciton}} P_{\text{exciton}}$. We assume that Γ_{carrier} vanishes because carriers recombine entirely via non-radiative channels, such as defect trapping, which is justified by the reported low quantum efficiencies
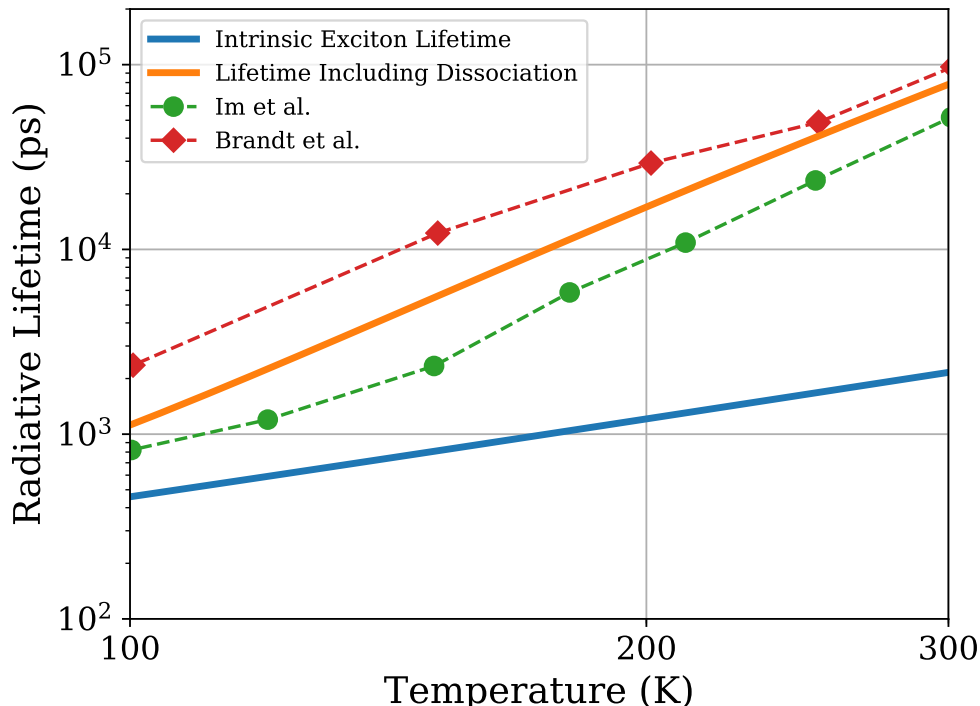
Figure 4.3: **Radiative lifetimes above 100 K with exciton dissociation included.** Our computed intrinsic excitonic radiative lifetimes (blue) and predicted lifetimes including exciton dissociation (orange) in bulk GaN as a function of temperature up to 300 K, compared with experimental data. The orange curve corresponds to $\Gamma_{\mathrm{rad}}^{-1}$ in Eq. (4.10) and is obtained by correcting for thermal exciton dissociation in the intrinsic lifetimes (including SOC). The green and red curves are taken from Refs. [19] and [22], respectively.

seen experimentally near room temperature [19]. The measured radiative rate Γ_{rad} at high temperatures becomes the intrinsic excitonic recombination rate, $\Gamma_{\mathrm{exciton}}$, suppressed by the probability that an electron-hole pair is in a bound exciton state (as opposed to a pair of free carriers):

$$\Gamma_{\mathrm{rad}} = \Gamma_{\mathrm{exciton}} P_{\mathrm{exciton}} = \frac{\Gamma_{\mathrm{exciton}}}{1 + \frac{n^*(T)}{n_0}} \qquad (4.10)$$

Using this result, we obtain the predicted measured radiative lifetime by correcting the excitonic radiative lifetimes computed with SOC. For the mass-action law in Eq. (4.9), we use our *ab initio* computed effective mass parameters and converged exciton binding energy (see Computational Details in Sec. 4.2). Since the background carrier density n_0 depends on the doping level of

the specific experimental sample, we use a typical value of 2.5×10^{16} cm^{-3}, taken from Ref. [19].

In Fig. 4.3 we show our computed intrinsic excitonic lifetime and the predicted measured lifetime as a function of temperature up to 300 K. We compare our lifetimes to PL measurements from from Refs. [19] and [22]. We find that when thermal dissociation is included, the radiative lifetimes are in excellent agreement with experiment even at temperatures above 150 K, where the experimental data deviates from the intrinsic exciton $T^{3/2}$ trend. This result confirms that the increase of the lifetime seen experimentally at higher temperatures in GaN is due to thermal dissociation of bound excitons into free carriers. We note that our radiative lifetimes deviate from the intrinsic trend at a lower temperature than they do in the experimental data. One possible cause may be a slight inaccuracy in our computed exciton binding energy − since its value is only 20 meV, accurately computing it is a challenge for the BSE approach. A deviation in the binding energy by ~ 10 meV, namely the typical accuracy for the BSE, can change the temperature at which dissociation effects become important by as much as 50 K.

4.4 Conclusions

We present an extension of an approach based on DFT plus the *ab initio* BSE method to compute the radiative lifetime in an anisotropic uniaxial bulk crystal as a function of temperature. We apply this approach to GaN, computing radiative lifetimes entirely from first principles in a uniaxial bulk material within this framework for the first time. Our results exhibit the $T^{3/2}$ trend expected for intrinsic excitonic radiative lifetimes in a bulk material, and we find excellent agreement with experimental measurements of intrinsic radiative lifetimes in GaN at low temperatures. We show the importance of including SOC for obtaining accurate exciton energies and transition dipoles, including the dark states, which are critical for obtaining accurate intrinsic radiative lifetimes. By accounting for thermal exciton dissociation, we obtain excellent agreement with experiment at high temperatures, where the interplay between excitons and carriers dominates over the intrinsic exciton dynamics. Future work will extend these calculations to study confinement effects on excitons and radiative lifetimes in GaN quantum wells, including the effect of confinement along different crystal axes, which can be done by modifying the exciton dispersion

equations. Our work adds to our general framework presented in Chapter 3, enabling predictions of intrinsic excitonic radiative lifetimes in an important class of materials for light emission and LED devices − in our case, the wurtzite III-nitrides. Our work also shows that these calculations can provide a benchmark for intrinsic radiative lifetimes as well as guide the interpretation of ultrafast spectroscopy measurements in light emitting materials where extrinsic effects, such as defects, play a role in the ultrafast carrier dynamics.

References

[1] J. P. Wolfe, "Thermodynamics of excitons in semiconductors", Phys. Today **35**, 46–54 (1982).

[2] X. Zhang, J.-X. Shen, W. Wang, and C. G. Van de Walle, "First-principles analysis of radiative recombination in lead-halide perovskites", ACS Energy Letters **3**, 2329–2334 (2018).

[3] E. Kioupakis, Q. Yan, D. Steiauf, and C. G. Van de Walle, "Temperature and carrier-density dependence of auger and radiative recombination in nitride optoelectronic devices", New J. Phys. **15**, 125006 (2013).

[4] R. J. Glauber and M. Lewenstein, "Quantum optics of dielectric media", Phys. Rev. A **43**, 467–491 (1991).

[5] H.-Y. Chen, M. Palummo, D. Sangalli, and M. Bernardi, "Theory and ab initio computation of the anisotropic light emission in monolayer transition metal dichalcogenides", Nano Lett. **18**, PMID: 29737164, 3839–3843 (2018).

[6] G. Lasher and F. Stern, "Spontaneous and stimulated recombination radiation in semiconductors", Phys. Rev. **133**, A553–A563 (1964).

[7] P. Giannozzi, S. Baroni, N. Bonini, M. Calandra, R. Car, C. Cavazzoni, D. Ceresoli, G. L. Chiarotti, M. Cococcioni, I. Dabo, et al., "QUANTUM ESPRESSO: a modular and open-source software project for quantum simulations of materials", J. Phys.: Condens. Matter **21**, 395502 (2009).

[8] J. P. Perdew, K. Burke, and M. Ernzerhof, "Generalized gradient approximation made simple", Phys. Rev. Lett. **77**, 3865–3868 (1996).

[9] D. R. Hamann, "Optimized norm-conserving vanderbilt pseudopotentials", Phys. Rev. B **88**, 085117 (2013).

[10] J. P. Perdew, A. Ruzsinszky, G. I. Csonka, O. A. Vydrov, G. E. Scuseria, L. A. Constantin, X. Zhou, and K. Burke, "Restoring the density-gradient expansion for exchange in solids and surfaces", Phys. Rev. Lett. **100**, 136406 (2008).

[11] M. van Setten, M. Giantomassi, E. Bousquet, M. Verstraete, D. Hamann, X. Gonze, and G.-M. Rignanese, "The pseudodojo: training and grading a 85 element optimized norm-conserving pseudopotential table", Comput. Phys. Commun. **226**, 39–54 (2018).

[12] S. G. Louie, S. Froyen, and M. L. Cohen, "Nonlinear ionic pseudopotentials in spin-density-functional calculations", Phys. Rev. B **26**, 1738–1742 (1982).

[13] A. Marini, C. Hogan, M. Grüning, and D. Varsano, "Yambo: an ab initio tool for excited state calculations", Comput. Phys. Commun. **180**, 1392–1403 (2009).

[14] F. Fuchs, C. Rödl, A. Schleife, and F. Bechstedt, "Efficient o (n 2) approach to solve the bethe-salpeter equation for excitonic bound states", Phys. Rev. B **78**, 085103 (2008).

[15] J. F. Muth, J. H. Lee, I. K. Shmagin, R. M. Kolbas, H. C. Casey, B. P. Keller, U. K. Mishra, and S. P. DenBaars, "Absorption coefficient, energy gap, exciton binding energy, and recombination lifetime of gan obtained from transmission measurements", Appl. Phys. Lett. **71**, 2572–2574 (1997).

[16] D. M. Ceperley and B. J. Alder, "Ground state of the electron gas by a stochastic method", Phys. Rev. Lett. **45**, 566 (1980).

[17] A. Rubio, J. L. Corkill, M. L. Cohen, E. L. Shirley, and S. G. Louie, "Quasi-particle band structure of aln and gan", Phys. Rev. B **48**, 11810–11816 (1993).

[18] G. Onida, L. Reining, and A. Rubio, "Electronic excitations: density-functional versus many-body green's-function approaches", Rev. Mod. Phys. **74**, 601–659 (2002).

[19] J. Im, A. Moritz, F. Steuber, V. Härle, F. Scholz, and A. Hangleiter, "Radiative carrier lifetime, momentum matrix element, and hole effective mass in gan", Appl. Phys. Lett. **70**, 631–633 (1997).

[20] H. W. Yoon, D. R. Wake, and J. P. Wolfe, "Effect of exciton-carrier thermodynamics on the gaas quantum well photoluminescence", Phys. Rev. B **54**, 2763–2774 (1996).

[21] N. Ashcroft and N. Mermin, *Solid state physics*, HRW international editions (Holt, Rinehart and Winston, 1976).

[22] O. Brandt, J. Ringling, K. H. Ploog, H.-J. Wünsche, and F. Henneberger, "Temperature dependence of the radiative lifetime in gan", Phys. Rev. B **58**, R15977–R15980 (1998).

C h a p t e r   5

INTRINSIC CARRIER MOBILITIES AND PIEZOELECTRIC ELECTRON-PHONON INTERACTIONS IN GALLIUM NITRIDE FROM FIRST PRINCIPLES

The content of this chapter is taken from the following work:

[1]V. A. Jhalani, J.-J. Zhou, and M. Bernardi, "Intrinsic carrier mobilities in GaN from first principles", *In Preparation.*

5.1   Introduction

Similar to hot carrier dynamics (discussed in detail in Chapter 2), charge carrier transport plays a key role in III-V semiconductor's electronic, opto-electronic, and photovoltaic device operations. Unlike hot carriers, which can have energies of up to a few eV from the band edges, charge transport at room temperature and at low fields is determined by carriers with energies within roughly 100 meV of the gap [1]. Understanding charge transport in GaN and predicting both the intrinsic (phonon-limited) mobility and the specific electron-phonon (e-ph) scattering mechanisms that regulate transport is critical for designing optoelectronic devices. However, in a similar vein as intrinsic radiative lifetimes, extracting intrinsic transport properties from experiment is non-trivial, as questions often arise related to the role of doping, impurities, and defects when interpreting transport measurements due to the challenges of fabricating pure samples of GaN.

Similar to hot carrier dynamics, carrier mobilities in GaN are typically investigated with semi-empirical models of the underlying scattering mechanisms, including defect scattering and different e-ph scattering processes [2–5]. This places *ab initio* computational approaches in a unique position to advance understanding of carrier transport, by computing the carrier scattering processes from first principles. Recently, calculations of carrier mobility employing *ab initio* band structures and phonon dispersions in similar wide bandgap polar semiconductors have been reported; however, these still rely on semi-empirical expressions for e-ph scattering or assumptions on the relative importance of

specific phonon modes [6–8]. In particular, as discussed in Chapter 2, the complexity of the valence band bandstructure and hole scattering in GaN has eluded capture by semi-empirical models and thus greatly limited microscopic understanding of hole transport, which is of particular relevance for GaN-based bipolar devices and LEDs [9]. One major challenge in computing transport in polar materials are long-range e-ph interactions, such as the Frölich interaction [10], namely the coupling between electrons and polar longitudinal optical (LO) phonons. The e-ph scattering due to LO modes is known to be a dominant scattering mechanism in polar semiconductors like GaN [1], but until recently it had yet to be properly treated in *ab initio* transport calculations.

Our recently developed workflow [11, 12] combining density functional perturbation theory (DFPT) [13], Wannier interpolation [14] and a generalized first-principles Frölich vertex [12] allows the calculation of accurate e-ph matrix elements on very fine grids in the Brillouin Zone (BZ) entirely from first principles in polar materials like GaN. This approach does not rely on empirical or analytical expressions of carrier scattering and treats all phonon modes on equal footing, enabling accurate calculations of relaxation times (RTs) and hot carrier dynamics in GaN, as we have shown above (see Chapter 2 and Ref. [15]). To investigate charge transport from first principles, the Boltzmann transport equation (BTE) within the relaxation time approximation (RTA) can be used to compute the conductivity and carrier mobility using *ab initio* e-ph scattering processes [16]. However, different from hot carriers, the calculation of phonon-limited carrier mobilities have the additional requirement of very fine BZ grids to converge the RTs at the low carrier energies that contribute to the mobility. Recently, we have developed a scheme that enables efficient calculation of large number of e-ph matrix elements, as is needed to converge the RTs and mobilities in polar materials in the presence of the Frölich interaction. Our group has recently applied this approach to GaAs, for which we computed electron mobilities in excellent agreement with experiment and provided detailed understanding of the contributions of different phonon modes to scattering electrons and controlling their mobility. [17].

Unlike GaAs, the III-nitrides have an additional polar phonon scattering mechanism, known as the piezoelectric (PZ) interaction, which can occur in materials that lack inversion symmetry [1, 16]. The PZ interaction couples electrons

with electric fields generated by strain induced by polar acoustic phonons. Both the transverse (TA) and longitudinal (LA) acoustic modes, depending on the phonon wavevector, can give rise to PZ scattering, which results from the quadrupole term in the e-ph interaction Hamiltonian [18, 19]. Unfortunately, the generalized first-principles Frölich coupling [12] neglects the quadrupole and higher order terms, resulting in an overestimation of the e-ph coupling strength when applied to acoustic modes. Though weak compared to the polar LO mode, the PZ interaction is important for accurately computing carrier scattering from acoustic modes and the mobility in PZ materials.

In this chapter, we discuss ongoing efforts to extend the methodology above to include PZ e-ph interactions derived from macroscopic theory in the interpolation scheme for obtaining accurate e-ph RTs at energies relevant for carrier mobility in GaN. Using a combination of the RTA-BTE and *ab initio* temperature- and state-dependent RTs, we compute electron and hole mobilities in wurtzite GaN at temperatures between 200-500 K. We compare our in-plane mobilities with Hall mobility experiments, obtaining very good agreement. Our calculations can also shed light on which phonon modes scatter electrons and holes more strongly in GaN as a function of temperature.

5.2   Computational Methods

We carry out density functional theory (DFT) ground state electronic structure calculations on GaN in the wurtzite structure with relaxed lattice parameters of $a = 3.17$ Å and $c = 5.16$ Å, using the local density approximation (LDA) [20] and a plane wave basis with the QUANTUM ESPRESSO code [21]. We employ a plane-wave kinetic energy cutoff of 80 Ry and scalar-relativistic norm-conserving pseudopotentials [22]. The pseudopotential of Ga includes a non-linear core correction [23] to account for the shallow $3d$ core states. Similar to the methodology of Sec. 2.6, we use DFPT [13] to compute lattice dynamical properties, such as phonon modes and dispersions, and the e-ph matrix elements [24] $g_{nm\nu}(\mathbf{k}, \mathbf{q})$, on coarse $8 \times 8 \times 8$ $\mathbf{k}$-point and $4 \times 4 \times 4$ $\mathbf{q}$-point BZ grids. The matrix elements are obtained at an arbitrary pair of $\mathbf{k}$- and $\mathbf{q}$-points by summing together the short-range part $g_{nm\nu}^S(\mathbf{k}, \mathbf{q})$, obtained by Wannier interpolation [14], and the long-range part $g_{nm\nu}^L(\mathbf{k}, \mathbf{q})$, computed

using the generalized Fröhlich vertex method of Ref. [12], which we implement independently [see Eq. (2.2)].

The band- and $\mathbf{k}$-dependent e-ph scattering rate $\Gamma_{n\mathbf{k}}$, which is the inverse of the RT, $\tau_{n\mathbf{k}}^{-1} = \Gamma_{n\mathbf{k}}$, is computed from the imaginary part of the lowest order e-ph self-energy [24], which was given earlier in Eq. (2.3). We compute the scattering rates with out in-house developed Perturbo code. We carefully converged the e-ph scattering rates using an approach we developed in Ref. [17]. We compute the scattering rates on a $200 \times 200 \times 200$ $\mathbf{k}$-point grid for electrons and a $100 \times 100 \times 100$ $\mathbf{k}$-point BZ grid for holes, using an 8 meV Gaussian broadening to approximate the δ functions. For each $\mathbf{k}$ point, and for both electrons and holes, the long-range contribution to the scattering rate was converged with 2×10^6 Cauchy-distributed $\mathbf{q}$ points. The remaining scattering rate contribution was converged with 1×10^5 and 2×10^5 uniformly distributed $\mathbf{q}$ points for electrons and holes, respectively.

The electrical conductivity tensor σ at temperature T is computed with the RTA-BTE [16] and is given by:

$$\sigma_{\alpha\beta}(T) = e^2 \int_{-\infty}^{+\infty} \mathrm{d}E \, (-\partial f/\partial E) \, \Sigma_{\alpha\beta}(E, T). \tag{5.1}$$

where f is the Fermi-Dirac distribution at temperature T, and $\Sigma_{\alpha\beta}(E,T)$ is the transport distribution function (TDF):

$$\Sigma_{\alpha\beta}(E,T) = \frac{2}{V_{\mathrm{uc}}} \sum_{n\mathbf{k}} \tau_{n\mathbf{k}}(T) \mathbf{v}_{n\mathbf{k}}^{\alpha} \mathbf{v}_{n\mathbf{k}}^{\beta} \delta(E - \varepsilon_{n\mathbf{k}}), \tag{5.2}$$

computed here using a tetrahedron integration method [25] with the *ab initio* relaxation times $\tau_{n\mathbf{k}}$ and interpolated [26, 27] band velocities $\mathbf{v}_{n\mathbf{k}}$; V_{uc} is the unit cell volume. The mobility is then obtained as $\mu = \sigma/ne$, where n is the intrinsic carrier concentration. An important consequence of Eqs. (5.1) and (5.2) is that the factors of $-\partial f/\partial E$ and $\mathbf{v}_{n\mathbf{k}}$ in the integrand restrict the non-negligible contributions to the conductivity to be from carriers within $\epsilon_{n\mathbf{k}} < 100$ meV of the band edges.

Fig. 5.1 shows the computed e-ph scattering rates using the standard Wannier interpolation plus Fröhlich correction scheme for both electrons and holes with energies within 0.2 eV of the band edges. The total scattering rate as
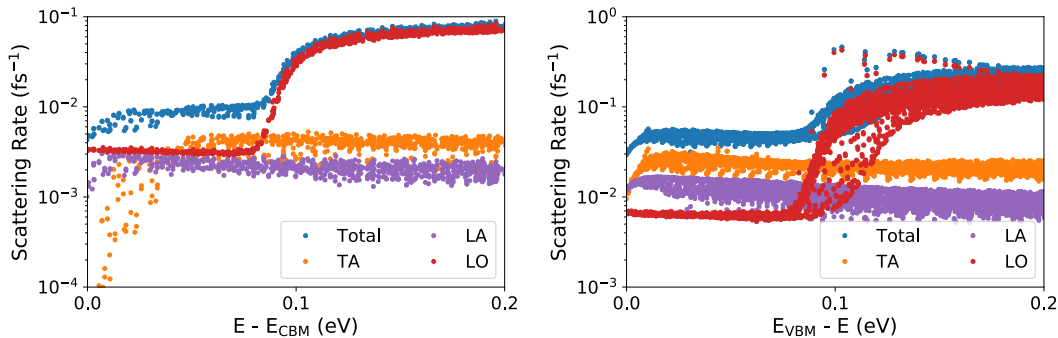
Figure 5.1: **E-ph scattering rates in GaN without piezoelectric interaction.** Electron (left) and hole (right) e-ph scattering rates as a function of carrier energy relative to the band edges, computed prior to adding piezoelectric interactions. Total carrier scattering rates are shown together with contributions from the LA, TA, and LO modes.

well as the contribution from the LO, LA, and TA phonon modes are shown. Below 0.1 eV, which corresponds to the LO phonon energy, the LO scattering rate is greatly suppressed due to LO phonon absorption being the only allowed scattering process. On the other hand, at this energy there is a large phase space for scattering with acoustic modes. Surprisingly, we find that for both electrons and holes the total scattering rate, and therefore the mobility, are not dominated by LO scattering. For electrons, LA and TA scattering provide a roughly equal contribution at energies between $\sim 10 - 90$ meV, whereas for holes both the LA and TA scattering rates are significantly higher than LO below ~ 90 meV. These results contradict the conventional wisdom of e-ph scattering in wurtzite III-nitrides, which assumes that LO scattering is dominant in III-V semiconductors due to their polar nature.

We verify the quality of the interpolation of the e-ph matrix elements by comparing the matrix elements interpolated from DFPT results on a coarse grid with those computed directly from DFPT The direct DFPT matrix elements can be used as a benchmark since they correctly capture long-range interactions, including the Fröhlich, PZ, and higher order terms [13]. Following Ref. [11], we define the deformation potential as a quantity proportional to the absolute value of the e-ph matrix element:

$$D_{nm}^{\nu}(\mathbf{k}, \mathbf{q}) = \frac{\sqrt{2M_{\mathrm{uc}}\omega_{\mathbf{q}\nu}}}{\hbar} \left| g_{nm\nu}(\mathbf{k}, \mathbf{q}) \right|, \qquad (5.3)$$

where M_{uc} is the mass of the unit cell. In the case of several initial and/or final electronic bands, the total deformation potential is defined as

$$D_{\text{tot}}^{\nu}(\mathbf{k}, \mathbf{q}) = \sqrt{\sum_{nm} \left(D_{nm}^{\nu}(\mathbf{k}, \mathbf{q})\right)^2} \tag{5.4}$$

In the following, we focus on comparing the interpolated and direct DFPT deformation potential $D_{\text{tot}}^{\nu}(\mathbf{k} = \Gamma, \mathbf{q})$, where the electron initial state is fixed to the Γ point, the phonon crystal momentum $\mathbf{q}$ is varied along the $M - \Gamma - A$ path, and the initial and final electronic bands are the two lowest conduction bands.

Fig. 5.2 shows deformation potentials comparing the accuracy of different approaches for including long-range e-ph matrix elements in the interpolation scheme. Notably, there are branches associated with acoustic modes with long-range interactions that are overestimated by the Fröhlich coupling, as can be seen by the blue points for branches approaching Γ from both the A and M directions. Furthermore, as shown by the purple points in Fig. 5.2, when one neglects the Fröhlich correction for all modes except the LO and only uses the short-range Wannier basis for interpolation, D_{tot}^{ν} vanishes as $\mathbf{q} \to 0$ instead of approaching a finite value as in the DFPT results (black circles). The specific $\mathbf{q} \to 0$ behavior seen in the DFPT results is due to the PZ interaction, which is missing in the Wannier plus Fröhlich correction interpolation scheme.

The PZ e-ph interaction is a long-range coupling between electrons and acoustic modes present in crystals without inversion symmetry, and to leading order it can be expressed as a quadrupole type interaction [19]. Developing a first-principles method to compute the quadrupole term and the PZ interaction is significantly more challenging than computing the Fröhlich interaction. One reason is that the microscopic PZ theory requires the calculation of quadrupole moment tensors for the ions, analogous to the Born effective charges for the dipole moments [18, 19]. While theoretically straightforward to obtain [19], the quadrupole moments are challenging to calculate in practice as they require computing $\mathbf{q}$-dependent Born charges, and are beyond state-of-the-art computational methods. However, for acoustic modes in the long-range ($\mathbf{q} \to 0$) limit where the lattice distortion corresponds to a uniform strain of the unit cell, the quadrupole term can be replaced with a macroscopic description that can potentially offer great improvement over neglecting the interaction altogether.
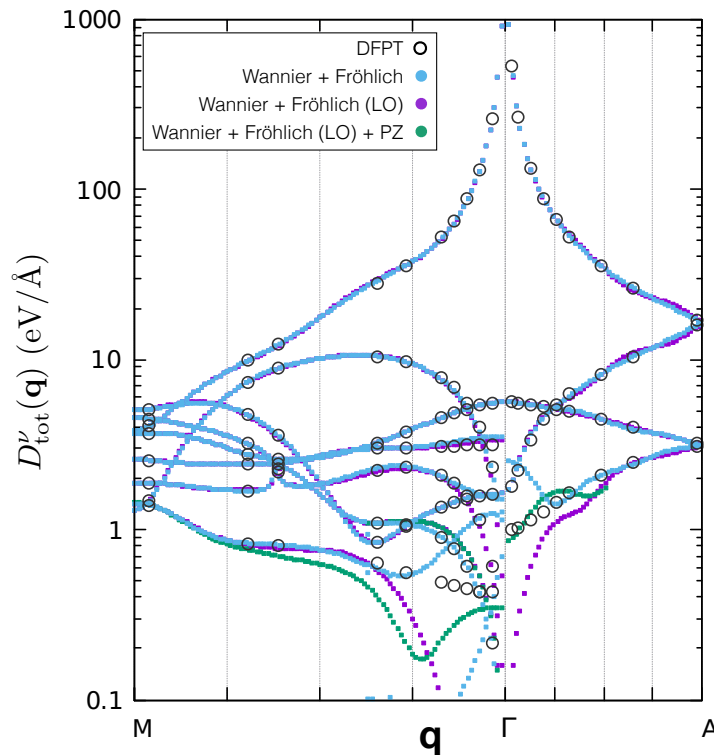
Figure 5.2: **Effect of piezoelectric correction on the interpolated e-ph matrix elements.** Mode-resolved deformation potentials as a function of $\mathbf{q}$ along high-symmetry lines comparing e-ph matrix elements computed from: DFPT benchmarks (black circles), Wannier interpolation and the generalized Fröhlich interaction applied to all modes (blue), Wannier interpolation and the Fröhlich interaction applied only to the LO mode (purple), and Wannier interpolation, Fröhlich interaction applied to LO only, and a PZ correction (green).

In this limit, the PZ coupling matrix elements can be expressed in terms of the piezoelectric constants, which relate strain to induced polarization and can be obtained from first principles within DFPT [28], using [16, 19]:

$$M_\nu(\mathbf{q}) = \frac{4\pi e}{\mathbf{q} \cdot \epsilon^0 \cdot \mathbf{q}} q_\alpha \mathrm{e}_{\alpha,\beta\gamma} q_\gamma \xi_\beta(\nu, \mathbf{q}) \left[\frac{\hbar}{2M_{uc}\omega_{\nu\mathbf{q}}} \right]^{\frac{1}{2}} \qquad (5.5)$$

where $\mathbf{q} = (q_x, q_y, q_z)$ is the phonon wavevector, $\mathrm{e}_{\alpha,\beta\gamma}$ are the components of the piezoelectric tensor, and $\xi_\beta(\nu, \mathbf{q})$ is a cartesian component of a vibrational eigenmode of a phonon normalized in the unit cell; summation over repeated indices is implied. We compute the piezoelectric tensors *ab initio* using the ABINIT code [29] from a charge density computed on a $18 \times 18 \times 18$ $\mathbf{k}$-point grid with an 80 Ry plane-wave cutoff.

We implement the PZ interaction by including the correction in Eq. (5.5) to the short-range acoustic mode matrix elements from Wannier interpolation. Technically, there are two components to the perturbation potential from a PZ mode [30]: the first term is from the internal strain of the atoms affecting the polarization and is proportional to the Born effective charges, and the second is the effect of the unit cell strain on the electronic structure, known as the clamped-ion term. The former is included in the Fröhlich coupling while the latter is not. The two terms have *nearly* equal but opposite contributions, corresponding to the previously mentioned cancellation of the dipole but not the quadrupole term in the PZ interaction. We elect to implement the PZ correction by using the total PZ tensor constants (summing both terms), which allows us to restrict the Fröhlich correction to the LO mode only. Lastly, one limitation is that in principle Eq. (5.5) is valid only in the $\mathbf{q} \to 0$ limit, where the vibrational eigenmodes are real-valued and correspond to a uniform translation of the ions. In contrast, in our work we deal with the $\mathbf{q} \neq 0$ case by using the complex eigenmodes obtained from DFPT and therefore obtain complex PZ coupling elements, similar to the Fröhlich case.

The green points in Fig. 5.2 show the results for the PZ correction. It is seen that by adding the complex coupling element of Eq. (5.5) to the interpolation scheme, we greatly improve the deformation potential for the LA mode with wavevector $\mathbf{q}$ along the $\Gamma - A$ direction (TA modes are not piezoelectric along this direction), which was overestimated with the Fröhlich correction and underestimated without it. While the result is not as good as for the $M - \Gamma$ direction (where only the TA modes are piezoelectric), our results are promising because we obtain much better agreement near $\mathbf{q} = 0$ compared to when only the Fröhlich correction is considered. We are corrently working to understand why the correction does not work as well for the in-plane phonon wavevectors. We believe that the Fourier transformation from reciprocal to Wannier space may be partially responsible for the discrepancy, resulting in the oscillations away from the DFPT points seen in Fig. 5.2 when the PZ coupling element is incuded. We are currently testing this and other hypotheses to improve the description of the PZ interactions.
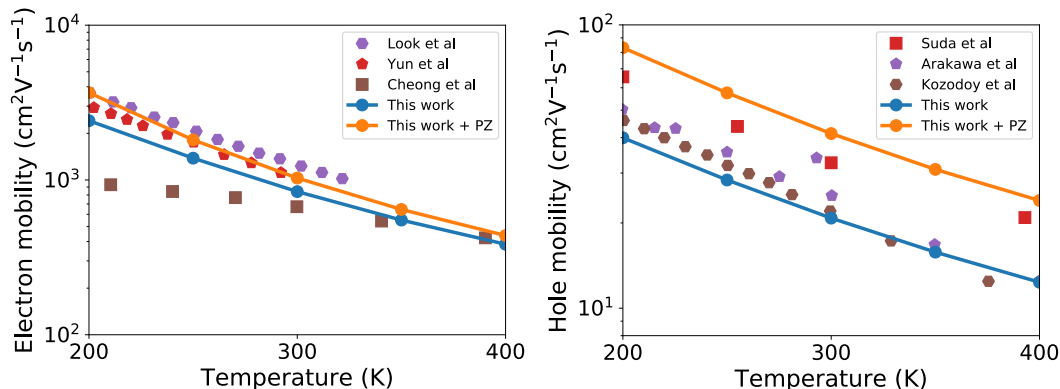
Figure 5.3: **Carrier mobilities in GaN as a function of temperature.** In-plane [1000] electron (left) and hole (right) mobilities in bulk GaN between 200-500 K. The electron experimental values, taken from Refs. [4, 31, 32], and holes values, from Refs. [33–35], are from van der Pauw Hall measurements and are compared to our ab initio results with and without the piezoelectric correction included (orange and blue, respectively).

5.3   Results

We now compute mobilities using RTs obtained from Eq. (2.3) in the RTA-BTE approximation given in Eqs. (5.1)-(5.2). We use both the typical Wannier plus Fröhlich interpolation scheme and the improved scheme including the PZ correction. Fig. 5.3 shows the in-plane [1000] component of our computed electron (left) and hole (right) mobilities using both interpolation methods along with experimental van der Pauw Hall mobility measurements of Refs. [4, 31–35] between 200-500 K. In these plots, the blue curve corresponds to using the original interpolation scheme which, for reference, produced the blue deformation potential in Fig. 5.2. The orange curve corresponds to restricting the Fröhlich correction to the LO mode and including the acoustic PZ correction of Eq. (5.5) in the interpolation scheme, corresponding to the green curve of Fig. 5.2. As expected, in both cases we see that the improved scheme increases the phonon-limited mobility, since the improvements resolved the overestimation of the coupling of non-longitudinal optical modes and polar acoustic modes to electrons. This results in *reduced* carrier scattering from TO and acoustic modes, and thus increased RTs and mobility. Notably, the change in the mobility is much more significant for holes. This is due to the greater number of inter-valley scattering channels and wider parabolic band dispersions in the valence band. By contrast, electrons have only a single, narrower, parabolic conduction band. This is further reflected by the fact that

in Fig. 5.1, the total electron scattering rate is only a factor of two greater than the LO rate, while for holes the discrepancy between the LO and total scattering rate is roughly an order of magnitude. Thus, by reducing the small-$\mathbf{q}$ coupling constants of acoustic modes with the improved scheme, the total scattering rate in holes is diminished to a much greater extent, as a significant proportion came from non-LO modes in the sub-100 meV energy range.

When comparing to experimental results, in both cases we find good agreement between our *ab initio* phonon-limited mobilities and the highest mobilities measured in samples with low doping concentrations ($\sim 10^{15}$ cm^{-3} for n-type [4] and $\sim 10^{16} - 10^{17}$ cm^{-3} for p-type [33, 34]). These correspond to the highest crystal quality samples, which guarantees that in the temperature range investigated here e-ph scattering dominates carrier transport. Notably, we find that the significant increase in mobility for holes using the improved scheme places it slightly above the experimental results. These trends are highly promising since our calculated intrinsic phonon-limited mobilities should correspond to an upper bound for the measurable mobility in pristine GaN samples, given that in any experimental sample there will always be additional scattering mechanisms from defects and interfaces.

5.4 Conclusion

Here, we have presented *ab initio* calculations of intrinsic phonon-limited carrier mobility in wurtzite GaN. By analyzing the deformation potentials, we found limitations in the interpolation scheme used as part of the typical workflow for state-of-the-art calculations to compute e-ph scattering rates and phonon-limited transport. We discussed our new method for interpolating the e-ph matrix elements while including a PZ correction in lieu of the challenging quadrupole moment of the e-ph interaction. We compute mobilities using our *ab initio* methodology without any empirical parameters, and find excellent agreement with experiment, which improves significantly when using our interpolation scheme. While the effort to improve PZ correction is still under way, these results are very promising for the calculation of intrinsic transport properties in polar wurtzite III-nitrides. In the future, these calculations will provide microscopic insight into various aspects of transport in III-nitride crys-

tals, including the transport properties of holes, the scattering mechanisms at play, and differences in transport along different crystal directions, all of which are important for bipolar GaN-based devices.

References

[1] B. K. Ridley, *Quantum processes in semiconductors* (Oxford University Press, 2013).

[2] B. K. Ridley, B. E. Foutz, and L. F. Eastman, "Mobility of electrons in bulk gan and $Al_xGa_{1-x}N$/GaN heterostructures", Phys. Rev. B **61**, 16862–16869 (2000).

[3] D. R. Anderson, N. A. Zakhleniuk, M. Babiker, B. K. Ridley, and C. R. Bennett, "Polar-optical phonon-limited transport in degenerate gan-based quantum wells", Phys. Rev. B **63**, 245313 (2001).

[4] D. C. Look and J. R. Sizelove, "Predicted maximum mobility in bulk GaN", Appl. Phys. Lett. **79**, 1133–1135 (2001).

[5] Y. Arakawa, K. Ueno, H. Imabeppu, A. Kobayashi, J. Ohta, and H. Fujioka, "Electrical properties of Si-doped GaN prepared using pulsed sputtering", Appl. Phys. Lett. **110**, 042103 (2017).

[6] A. Faghaninia, J. W. Ager, and C. S. Lo, "*Ab initio* electronic transport model with explicit solution to the linearized Boltzmann transport equation", Phys. Rev. B **91**, 235123 (2015).

[7] A. Prakash, P. Xu, A. Faghaninia, S. Shukla, J. W. Ager III, C. S. Lo, B. Jalan, J. W. Ager, C. S. Lo, and B. Jalan, "Wide bandgap BaSnO3 films with room temperature conductivity exceeding 104 S cm?1", Nat. Comm. **8** (2017).

[8] K. Krishnaswamy, B. Himmetoglu, Y. Kang, A. Janotti, and C. G. Van de Walle, "First-principles analysis of electron transport in $BaSnO_3$", Phys. Rev. B **95**, 205202 (2017).

[9] M. R. Krames, O. B. Shchekin, R. Mueller-Mach, G. O. Mueller, L. Zhou, G. Harbers, and M. G. Craford, "Status and future of high-power light-emitting diodes for solid-state lighting", J. Disp. Technol. **3**, 160–175 (2007).

[10] H. Fröhlich, "Electrons in lattice fields", Adv. Phys. **3**, 325–361 (1954).

[11] J. Sjakste, N. Vast, M. Calandra, and F. Mauri, "Wannier interpolation of the electron-phonon matrix elements in polar semiconductors: Polar-optical coupling in GaAs", Phys. Rev. B **92**, 054307 (2015).

[12] C. Verdi and F. Giustino, "Fröhlich electron-phonon vertex from first principles", Phys. Rev. Lett. **115**, 176401 (2015).

[13] S. Baroni, S. de Gironcoli, A. Dal Corso, and P. Giannozzi, "Phonons and related crystal properties from density-functional perturbation theory", Rev. Mod. Phys. **73**, 515–562 (2001).

[14] F. Giustino, M. L. Cohen, and S. G. Louie, "Electron-phonon interaction using Wannier functions", Phys. Rev. B **76**, 165108 (2007).

[15] V. A. Jhalani, J.-J. Zhou, and M. Bernardi, "Ultrafast hot carrier dynamics in GaN and its impact on the efficiency droop", Nano Lett. **17**, 5012–5019 (2017),

[16] G. D. Mahan, *Condensed matter in a nutshell* (Princeton University Press, 2010).

[17] J.-J. Zhou and M. Bernardi, "*Ab initio* electron mobility and polar phonon scattering in GaAs", Phys. Rev. B **94**, 201201(R) (2016).

[18] P. Vogl, "Microscopic theory of electron-phonon interaction in insulators or semiconductors", Phys. Rev. B **13**, 694–704 (1976).

[19] P. Vogl, "The electron-phonon interaction in semiconductors", in *Physics of nonlinear transport in semiconductors* (Springer, 1980), pp. 75–115.

[20] J. P. Perdew and A. Zunger, "Self-interaction correction to density-functional approximations for many-electron systems", Phys. Rev. B **23**, 5048 (1981).

[21] P. Giannozzi, S. Baroni, N. Bonini, M. Calandra, R. Car, C. Cavazzoni, D. Ceresoli, G. L. Chiarotti, M. Cococcioni, I. Dabo, et al., "QUANTUM ESPRESSO: a modular and open-source software project for quantum simulations of materials", J. Phys.: Condens. Matter **21**, 395502 (2009).

[22] N. Troullier and J. L. Martins, "Efficient pseudopotentials for plane-wave calculations", Phys. Rev. B **43**, 1993 (1991).

[23] S. G. Louie, S. Froyen, and M. L. Cohen, "Nonlinear ionic pseudopotentials in spin-density-functional calculations", Phys. Rev. B **26**, 1738–1742 (1982).

[24] M. Bernardi, "First-principles dynamics of electrons and phonons", Eur. Phys. J. B **89**, 239 (2016).

[25] P. E. Blöchl, O. Jepsen, and O. K. Andersen, "Improved tetrahedron method for brillouin-zone integrations", Phys. Rev. B **49**, 16223–16233 (1994).

[26] J. R. Yates, X. Wang, D. Vanderbilt, and I. Souza, "Spectral and fermi surface properties from wannier interpolation", Phys. Rev. B **75**, 195121 (2007).

[27] A. A. Mostofi, J. R. Yates, G. Pizzi, Y.-S. Lee, I. Souza, D. Vanderbilt, and N. Marzari, "An updated version of Wannier90: A tool for obtaining maximally-localised Wannier functions", Comput. Phys. Commun. **185**, 2309–2310 (2014).

[28] D. R. Hamann, X. Wu, K. M. Rabe, and D. Vanderbilt, "Metric tensor formulation of strain in density-functional perturbation theory", Phys. Rev. B **71**, 035117 (2005).

[29] X. Gonze, F. Jollet, F. A. Araujo, D. Adams, B. Amadon, T. Applencourt, C. Audouze, J.-M. Beuken, J. Bieder, A. Bokhanchuk, et al., "Recent developments in the abinit software package", Comput. Phys. Commun. **205**, 106–131 (2016).

[30] F. Bernardini, V. Fiorentini, and D. Vanderbilt, "Spontaneous polarization and piezoelectric constants of iii-v nitrides", Phys. Rev. B **56**, R10024–R10027 (1997).

[31] F. Yun, M. Reshchikov, K. Jones, P. Visconti, H. Morkoç, S. Park, and K. Lee, "Electrical, structural, and optical characterization of free-standing gan template grown by hydride vapor phase epitaxy", Solid State Electron. **44**, 2225–2232 (2000).

[32] M. G. Cheong, K. S. Kim, C. S. Oh, N. W. Namgung, G. M. Yang, C.-H. Hong, K. Y. Lim, E.-K. Suh, K. S. Nahm, H. J. Lee, D. H. Lim, and A. Yoshikawa, "Conductive layer near the GaN/sapphire interface and its effect on electron transport in unintentionally doped n-type GaN epilayers", Appl. Phys. Lett. **77**, 2557–2559 (2000).

[33] J. Suda and M. Horita, "Characterization of n-type and p-type GaN layers grown on free-standing GaN substrates", in 2016 compound semiconductor week (June 2016), pp. 1–2.

[34] Y. Arakawa, K. Ueno, A. Kobayashi, J. Ohta, and H. Fujioka, "High hole mobility p-type GaN with low residual hydrogen concentration prepared by pulsed sputtering", APL Mater. **4**, 086103 (2016).

[35] P. Kozodoy, H. Xing, S. P. DenBaars, U. K. Mishra, A. Saxler, R. Perrin, S. Elhamri, and W. C. Mitchel, "Heavy doping effects in mg-doped gan", J. Appl. Phys. **87**, 1832–1835 (2000).

Chapter   6

SUMMARY AND FUTURE DIRECTIONS

In summary, we present research that focuses on the investigation of ultra-fast carrier dynamics, light emission, and charge carrier transport using first-principles methods in GaN and related III-V semiconductors. In Chapter 2 we apply novel workflows for the efficient calculation of electron-phonon matrix elements to compute scattering rates and relaxation dynamics of hot carriers in GaN. These calculations provide details beyond the reach of previously employed theoretical and experimental methods, shedding light on the significant asymmetry in hot hole and electron scattering and thermalization rates, the origin of this asymmetry, and the non-negligible role of phonon scattering mechanisms besides the polar LO mode for holes. The microsopic insight gained by these calculations is also used to develop a model that can explain experimental observations of LED efficiency droop as a consequence of hot carrier cooling.

In Chapter 3 we present a general approach based on DFT and the first-principles BSE method to compute radiative lifetimes in bulk crystals, 2D, 1D materials and 0D isolated quantum light emitters with excitonic effects and thermal effects included. We present numerical results in GaAs, computing radiative lifetimes of excitons in a bulk material from first principles for the first time. Our results help interpret the unexpectedly long experimental photoluminescent decay times observed in GaAs by different groups and confirm these effects are not due to the intrinsic lifetimes but possibly nonequillibrium exciton dynamics. This approach in practice is a straightforward post-processing of transition dipole elements computed from the BSE and this is broadly applicable to a range of technologically relevant light emitters beyond bulk III-V semiconductors.

In Chapter 4 we extend the approach of Chapter 3 to uniaxial bulk crystals and apply it to wurtzite GaN. We present radiative lifetimes computed from first-principles in a uniaxial bulk crystal for the first time. Our results match the expected temperature trend for intrinsic lifetimes, and we find excellent

agreement with experimental measurements of intrinsic radiative lifetimes in GaN at low temperatures. We show the importance of including spin-orbit coupling for including dark exciton states and obtaining accurate intrinsic radiative lifetimes. Additionally, we obtain excellent agreement with experimental results at high temperature by accounting for the thermal dissociation of excitons into free carriers.

In Chapter 5 we present first-principles calculations of intrinsic phonon-limited carrier mobility in wurtzite GaN. We found limitations in the interpolation scheme used as part of the typical workflow for state-of-the-art calculations to compute electron-phonon scattering rates and phonon-limited transport. We discuss a new method for interpolating electron-phonon matrix elements while including a piezoelectric correction. We compute mobilities using our first-principles methodology free of empirical parameters and find excellent agreement with experiment, which improves significantly when using our improved interpolation scheme. Further refinement and improvement upon this interpolation scheme and the piezoelectric interaction are possible and ongoing.

Natural near-term extensions of the work presented here would focus on investigations of hot carrier dynamics, light emission, and transport in other III-nitrides of relevance to LED technology; namely AlN, InN, and alloyed compounds such as $Ga_xAl_{1-x}N$ and $Ga_xIn_{1-x}N$. One challenge will be the size of unit cells that accurately capture the structure of these alloys; some promising work has already begun on employing special quasi-random supercells which mimic the correlations of random binary solutions in the hexagonal close-packed structure using a minimal number of atoms [1]. These special structures have been used to generate unit cells of $Ga_xAl_{1-x}N$ and $Ga_xIn_{1-x}N$ alloys for $x = 0.25$, 0.5, and 0.75. The investigation of trends of hot carrier relaxation times and radiative lifetimes in these alloys may provide insight into ways GaN-based devices can be engineered such that electron leakage and efficiency droop are mitigated. Furthermore, with an improved interpolation scheme emplying piezoelectric interactions, investigations of transport properties of holes and differences in transport along different crystal directions in different III-nitrides are possible, all of which are critical for bipolar GaN-based devices like LEDs. By modifying the formulas, the radiative lifetimes formalism in Chapter 3 can be extended to study confinement effects on excitons and

radiative lifetimes in GaN and III-nitride quantum wells, including the effect of confinement along different crystal axes. Macroscopic device scale properties such as carrier diffusion lengths in LEDs can then also be calculated by combining electron-phonon mean free paths, real-time dynamics calculations, and radiative lifetimes in in LEDs and other GaN-based devices, such as power electronics [2, 3], opening a path to device-level simulations entire from first principles.

Hot carrier dynamics, carrier transport, and light emission are also relevant to a wide range of materials of technological relevance beyond III-nitrides and III-V semiconductors, providing interesting long-term applications of this work. LED technology has expanded significantly beyond GaN and III-V based technology, but the basic principle of injecting carriers into radiative recombination centers to efficiently emit light applies. Calculations of hot carrier dynamics, electron and hole transport properties, and intrinsic radiative lifetimes in organic molecules and polymers for OLED technology [4] can be of high interest. Recently, LEDs have also been demonstrated using hybrid organic/inorganic perovskites [5], a class of materials generating great interest as a photovoltaic due to promising, but puzzling, transport and light emission/absorption properties. Properties such as unusually high mobilitiies in the presence of defects and forgiving quantum efficiency at low crystal quality have been experimentally observed but are poorly understood [6]. First-principles methods have only recently begun to shed light on the mechanisms contributing to the intrinsic transport properties in perovskites [7], and extending the work presented here to compute mobilities, hot carrier relaxation, and exciton lifetimes could be of great interest. Beyond LEDs, in recent years a diverse set of solid-state single-photon emitters (SPE) for quantum information applications have emerged [8]. Currently in their early proof-of-concept stages, these SPEs have been realized using emission centers around defects in systems of all dimensionality, such as bulk crystals like diamond and SiC, 2D materials like BN and transition metal dichalcogenides, 1D carbon nanotubes, as well as 0D III-nitride and III-V quantum dots [8]. The framework developed in Chapter 3 could enable the investigation of intrinsic light emission properties of excitons in SPEs of interest and aid the realization of scalable quantum information processing technologies.

References

[1] D. Shin, R. Arróyave, Z.-K. Liu, and A. Van de Walle, "Thermodynamic properties of binary hcp solution phases from special quasirandom structures", Phys. Rev. B **74**, 024204 (2006).

[2] H. Okumura, "A roadmap for future wide bandgap semiconductor power electronics", MRS Bull. **40**, 439–444 (2015).

[3] S. Dimitrijev, J. Han, H. A. Moghadam, and A. Aminbeidokhti, "Power-switching applications beyond silicon: status and future prospects of SiC and GaN devices", MRS Bull. **40**, 399–405 (2015).

[4] N. T. Kalyani and S. Dhoble, "Organic light emitting diodes: energy saving lighting technology—a review", Renew. Sust. Energ. Rev. **16**, 2696–2723 (2012).

[5] Y.-H. Kim, H. Cho, J. H. Heo, T.-S. Kim, N. Myoung, C.-L. Lee, S. H. Im, and T.-W. Lee, "Multicolored organic/inorganic hybrid perovskite light-emitting diodes", Adv. Mater. **27**, 1248–1254 (2015).

[6] W.-J. Yin, J.-H. Yang, J. Kang, Y. Yan, and S.-H. Wei, "Halide perovskite materials for solar cells: a theoretical review", J. Mater. Chem. A **3**, 8926–8942 (2015).

[7] K. Frohna, T. Deshpande, J. Harter, W. Peng, B. A. Barker, J. B. Neaton, S. G. Louie, O. M. Bakr, D. Hsieh, and M. Bernardi, "Inversion symmetry and bulk rashba effect in methylammonium lead iodide perovskite single crystals", Nat. Comm. **9**, 1829 (2018).

[8] I. Aharonovich, D. Englund, and M. Toth, "Solid-state single-photon emitters", Nat. Phot. **10**, 631–641 (2016).

$$Appendix \ A$$

SECOND QUANTIZATION OF LIGHT IN ANISOTROPIC MATERIALS

Starting from Maxwell's equations in a material:

$$\boldsymbol{\nabla} \cdot \mathbf{D} = 0 \ , \qquad \frac{\partial \mathbf{D}}{\partial t} = \boldsymbol{\nabla} \times \mathbf{H} \ ; \ \mathbf{D} = \epsilon_0 \boldsymbol{\epsilon}_r \mathbf{E} \ ,$$

$$\boldsymbol{\nabla} \cdot \mathbf{B} = 0 \ , \qquad -\frac{\partial \mathbf{B}}{\partial t} = \boldsymbol{\nabla} \times \mathbf{E} \ ; \ \mathbf{B} = \mu_0 \mathbf{H} \ , \tag{A.1}$$

where ϵ_0 is the vacuum permittivity and μ_0 the vacuum susceptibility, we define the vector potential $\mathbf{A}$ and the scalar potential Φ:

$$\mathbf{B} = \boldsymbol{\nabla} \times \mathbf{A}, \quad \mathbf{E} = -\boldsymbol{\nabla}\Phi - \frac{\partial \mathbf{A}}{\partial t}. \tag{A.2}$$

We adopt a generalized Coulomb gauge, in which:

$$\Phi = 0, \quad \boldsymbol{\nabla} \cdot (\epsilon_0 \boldsymbol{\epsilon}_r \mathbf{E}) = 0 \ , \tag{A.3}$$

and write the equation of motion for $\mathbf{A}$ as

$$- \mu_0 \epsilon_0 \boldsymbol{\epsilon}_r \frac{\partial^2 \mathbf{A}}{\partial t^2} = \boldsymbol{\nabla} \times (\boldsymbol{\nabla} \times \mathbf{A}) = \boldsymbol{\nabla}(\boldsymbol{\nabla} \cdot \mathbf{A}) - \boldsymbol{\nabla}^2 \mathbf{A}. \tag{A.4}$$

From Eq. (A.4), we construct the Lagrangian

$$\begin{aligned} \mathcal{L} &= \frac{1}{2} \int d\mathbf{r} \left[\epsilon_0 \mathbf{E}^T(\mathbf{r}) \boldsymbol{\epsilon}_r \mathbf{E}(\mathbf{r}) - \frac{\mathbf{B}(\mathbf{r})^2}{\mu_0} \right] \\ &= \frac{1}{2} \int d\mathbf{r} \left[\epsilon_0 \dot{\mathbf{A}}^T(\mathbf{r}) \boldsymbol{\epsilon}_r \dot{\mathbf{A}}(\mathbf{r}) - \frac{(\boldsymbol{\nabla} \times \mathbf{A})^2}{\mu_0} \right]. \end{aligned} \tag{A.5}$$

The conjugate momentum of the vector potential is

$$\boldsymbol{\Pi}(\mathbf{r}) = \frac{\delta \mathcal{L}}{\delta \dot{\mathbf{A}}(\mathbf{r})} = \epsilon_0 \boldsymbol{\epsilon}_r \dot{\mathbf{A}}(\mathbf{r}), \tag{A.6}$$

and by performing a Legendre transformation, we write the Hamiltonian as

$$\mathcal{H} = \int d\mathbf{r} \, \boldsymbol{\Pi} \, \dot{\mathbf{A}} - \mathcal{L} = \frac{1}{2} \int d\mathbf{r} \left[\frac{\boldsymbol{\Pi}^T \boldsymbol{\epsilon}_r^{-1} \boldsymbol{\Pi}}{\epsilon_0} + \frac{(\boldsymbol{\nabla} \times \mathbf{A})^2}{\mu_0} \right]. \tag{A.7}$$

Note that the Hamiltonian for classical electromagnetic field in vacuum can be recovered by setting $\boldsymbol{\epsilon}_r = \mathbf{I}$.

To define the creation and annihilation operators for second quantization, we follow the standard procedure and expand the vector potential in terms of its eigenmodes, which are labeled by the index λ:

$$\mathbf{A}(\mathbf{r}, t) = \sum_{\lambda} q_{\lambda} \mathbf{f}_{\lambda}(\mathbf{r}) e^{i\omega_{\lambda} t}, \tag{A.8}$$

where q_{λ} are constants representing the amplitudes and $\mathbf{f}_{\lambda}(\mathbf{r})$ satisfy

$$\omega_{\lambda}^2 \mu_0 \epsilon_0 \boldsymbol{\epsilon}_r \mathbf{f}_{\lambda} - \boldsymbol{\nabla} \times (\boldsymbol{\nabla} \times \mathbf{f}_{\lambda}) = 0. \tag{A.9}$$

Since ω_{λ} enters the equation as a square, both $+\omega_{\lambda}$ and $-\omega_{\lambda}$ can have the same $\mathbf{f}_{\lambda}$ solution. However, since the vector potential is always real, we need $\mathbf{A}^{\dagger} = \mathbf{A}$, so that for each $q_{\lambda} \mathbf{f}_{\lambda}(\mathbf{r}) e^{i\omega_{\lambda} t}$ in Eq. (A.8), there must exists a corresponding term $q_{\lambda}' \mathbf{f}_{\lambda}'(\mathbf{r}) e^{-i\omega_{\lambda} t}$ such that

$$q_{\lambda}' \mathbf{f}_{\lambda}'(\mathbf{r}) = q_{\lambda}^* \mathbf{f}_{\lambda}^*(\mathbf{r}). \tag{A.10}$$

For convenience, we label this part of the solution as $-\lambda$:

$$q_{\lambda}' \mathbf{f}_{\lambda}'(\mathbf{r}) e^{-i\omega_{\lambda} t} = q_{-\lambda} \mathbf{f}_{-\lambda}(\mathbf{r}) e^{i\omega_{-\lambda} t}. \tag{A.11}$$

To obtain an orthogonality condition for the solutions, we substitute $\mathbf{f}_{\lambda}(\mathbf{r}) = \frac{\sqrt{\boldsymbol{\epsilon}_r}^{-1}}{\sqrt{\mu_0 \epsilon_0}} \mathbf{g}_{\lambda}(\mathbf{r})$ and get:

$$s\omega_{\lambda}^2 \mathbf{g}_{\lambda} - \frac{\sqrt{\boldsymbol{\epsilon}_r}^{-1}}{\sqrt{\mu_0 \epsilon_0}} \boldsymbol{\nabla} \times \left(\boldsymbol{\nabla} \times \frac{\sqrt{\boldsymbol{\epsilon}_r}^{-1}}{\sqrt{\mu_0 \epsilon_0}} \mathbf{g}_{\lambda} \right) = 0. \tag{A.12}$$

Now with ω_{λ}^2 as the eigenvalue, $\mathbf{g}_{\lambda}$ are eigenfunctions of a Hermitian operator and form an orthogonal solution set:

$$\int d\mathbf{r}\; \mathbf{g}_{\lambda}^{\dagger}(\mathbf{r}) \cdot \mathbf{g}_{\lambda'}(\mathbf{r}) = \int d\mathbf{r}\; \mu_0 \epsilon_0 \mathbf{f}_{\lambda}^{\dagger}(\mathbf{r}) \boldsymbol{\epsilon}_r \mathbf{f}_{\lambda'}(\mathbf{r}) = \delta_{\lambda, \lambda'}. \tag{A.13}$$

In the following, we take plane waves as our eigenmodes, and label them by their polarization and momentum by substituting $\lambda \to (\lambda, \mathbf{q})$, $-\lambda \to (-\lambda, -\mathbf{q})$. We also put

$$\mathbf{f}_{\lambda\mathbf{q}}(\mathbf{r}) = \frac{\mathbf{e}_{\lambda\mathbf{q}}}{\sqrt{\mu_0 \epsilon_0}} e^{i\mathbf{q}\cdot\mathbf{r}}. \tag{A.14}$$

The equation of motion becomes

$$\omega_{\lambda\mathbf{q}}^2 \mu_0 \epsilon_0 \boldsymbol{\epsilon}_r \mathbf{e}_{\lambda\mathbf{q}} + \mathbf{q}\left(\mathbf{q}\cdot\mathbf{e}_{\lambda\mathbf{q}}\right) - q^2 \mathbf{e}_{\lambda\mathbf{q}} = 0, \tag{A.15}$$

the orthogonality condition

$$\mathbf{e}_{\lambda\mathbf{q}}^{\dagger}\epsilon_r\mathbf{e}_{\lambda'\mathbf{q}} = \delta_{\lambda,\lambda'} \ , \tag{A.16}$$

and the relation connecting λ and $-\lambda$:

$$q_{\lambda\mathbf{q}}^*\mathbf{e}_{\lambda\mathbf{q}}^* = q_{-\lambda,-\mathbf{q}}\mathbf{e}_{-\lambda,-\mathbf{q}}. \tag{A.17}$$

Then the vector potential can be written as

$$\begin{aligned}\mathbf{A}(\mathbf{r},t) &= \sum_{\lambda\mathbf{q}} q_{\lambda\mathbf{q}}\frac{\mathbf{e}_{\lambda\mathbf{q}}}{\sqrt{\mu_0\epsilon_0}}e^{i(\mathbf{q}\cdot\mathbf{r}+\omega_{\lambda\mathbf{q}}t)} \\ &= c\sum_{\lambda>0,\mathbf{q}} q_{\lambda\mathbf{q}}\mathbf{e}_{\lambda\mathbf{q}}e^{i(\mathbf{q}\cdot\mathbf{r}+\omega_{\lambda\mathbf{q}}t)} + q_{\lambda\mathbf{q}}^*\mathbf{e}_{\lambda\mathbf{q}}^*e^{-i(\mathbf{q}\cdot\mathbf{r}+\omega_{\lambda\mathbf{q}}t)}\end{aligned} \tag{A.18}$$

and the conjugate momentum becomes:

$$\mathbf{\Pi}(\mathbf{r},t) = c\sum_{\lambda\mathbf{q}} iq_{\lambda\mathbf{q}}\omega_{\lambda\mathbf{q}}\epsilon_0\epsilon_r\mathbf{e}_{\lambda\mathbf{q}}e^{i(\mathbf{q}\cdot\mathbf{r}+\omega_{\lambda\mathbf{q}}t)}. \tag{A.19}$$

The Hamiltonian can be written as:

$$\begin{aligned}\mathcal{H} &= \epsilon_0 c^2 V \sum_{\lambda\mathbf{q}} \omega_{\lambda\mathbf{q}}^2 q_{\lambda\mathbf{q}}^* q_{\lambda\mathbf{q}} \\ &= \epsilon_0 c^2 V \sum_{\lambda>0,\mathbf{q}} \omega_{\lambda\mathbf{q}}^2 (q_{\lambda\mathbf{q}}^* q_{\lambda\mathbf{q}} + q_{\lambda\mathbf{q}} q_{\lambda\mathbf{q}}^*),\end{aligned} \tag{A.20}$$

where V is the volume of the system. Finally, we can define creation and annihilation operators for $\lambda > 0$:

$$\hat{a}_{\lambda\mathbf{q}} = c\sqrt{\frac{2V\omega_{\lambda\mathbf{q}}\epsilon_0}{\hbar}}q_{\lambda\mathbf{q}}, \quad \left[\hat{a}_{\lambda\mathbf{q}}, \hat{a}_{\lambda'\mathbf{q}'}^{\dagger}\right] = \delta_{\mathbf{q},\mathbf{q}'}\delta_{\lambda,\lambda'} \tag{A.21}$$

using which the vector potential operator becomes:

$$\mathbf{A}(\mathbf{r},t) = \sum_{\lambda\mathbf{q}} \sqrt{\frac{\hbar}{2V\omega_{\lambda\mathbf{q}}\epsilon_0}}\left(\hat{a}_{\lambda\mathbf{q}}\mathbf{e}_{\lambda\mathbf{q}}e^{i(\mathbf{q}\cdot\mathbf{r}+\omega_{\lambda\mathbf{q}}t)} + h.c.\right) \tag{A.22}$$

and the Hamiltonian:

$$\mathcal{H} = \sum_{\lambda\mathbf{q}} \hbar\omega_{\lambda\mathbf{q}}\left(\hat{a}_{\lambda\mathbf{q}}^{\dagger}\hat{a}_{\lambda\mathbf{q}} + \frac{1}{2}\right). \tag{A.23}$$

$Appendix\ \ B$

DERIVATION OF THE RADIATIVE LIFETIME IN ISOTROPIC 3D MATERIALS

We provide additional details for the derivation of the radiative recombination rate in isotropic 3D materials, Eq. (3.23). In an isotropic bulk material with dielectric constant ϵ, the photon vector potential is given by Eq. (3.9) with frequency $\omega_{\mathbf{q}} = c\,|\mathbf{q}|/\sqrt{\epsilon}$, and the IP and OOP polarization vectors are those in Eq. (3.21). Due to momentum conservation, the summation over all possible final photon wavevectors in Eq. (3.11) is restricted to $\mathbf{q} = \mathbf{Q}$. As a result, we can write the radiative rate as

$$
\begin{aligned}
\gamma_S^{\text{3D, iso}}(\mathbf{Q}) = \frac{\pi e^2}{\epsilon_0 m^2 V c Q \sqrt{\epsilon}} &\left\{ |-p_{Sx}\sin\varphi + p_{Sy}\cos\varphi|_{\text{IP}}^2 \right. \\
&+ |p_{Sx}\cos\theta\cos\varphi + p_{Sy}\cos\theta\sin\varphi - p_{Sz}\sin\theta|_{\text{OOP}}^2 \Big\} \\
&\times \delta\left(E_S(\mathbf{Q}) - \frac{\hbar c Q}{\sqrt{\epsilon}} \right).
\end{aligned}
\tag{B.1}
$$

By setting $\cos\varphi = Q_x/Q_{xy}$, where $\mathbf{Q}_{xy}$ is the projection of $\mathbf{Q}$ onto the xy plane, and $\cos\theta = Q_z/Q$, we obtain Eq. (3.22). To obtain the radiative rate at finite temperature T, we plug Eq. (3.22) into Eq. (3.12) along with the parabolic dispersion in Eq. (3.13). The denominator, due to lack of angular dependence, reduces to a Gaussian integral of the kind $\int_0^\infty dx\, x^2 \exp(-x^2) = \sqrt{\pi}/4$, and gives

$$
\begin{aligned}
\int dQ_x dQ_y dQ_z\, &e^{-E_S(Q)/k_B T} \\
&= \int d\Omega \int_0^\infty dQ\, Q^2\, e^{\frac{-\hbar^2 Q^2}{2M_S k_B T}} = \left(\frac{2\pi M_S k_B T}{\hbar^2} \right)^{3/2}
\end{aligned}
\tag{B.2}
$$

where $d\Omega = \sin\theta d\theta d\varphi$ is the differential solid angle, and we leave out the factor $e^{-E_S(0)/k_B T}$, which is present both in the numerator and denominator and cancels out in the final result. For the numerator, we note that the exciton parabolic dispersion can be approximated as flat within the light cone, so that

we can put $E_S(\mathbf{Q}) \approx E_S(0)$. As a result, we get

$$
\int dQ_x dQ_y dQ_z \, e^{-E_S(Q)/k_B T} \, \gamma_S^{\text{3D, iso}}(\mathbf{Q}) = \int d\Omega \int_0^\infty dQ \, Q^2 e^{-E_S(Q)/k_B T} \, \gamma_S^{\text{3D, iso}}(\mathbf{Q})
$$

$$
\approx \frac{\pi e^2}{\epsilon_0 m^2 V c \sqrt{\epsilon}} \int d\Omega \int dQ \, Q \left\{ |-p_{Sx} \sin \varphi + p_{Sy} \cos \varphi|^2 \right.
$$

$$
\left. + |p_{Sx} \cos \theta \cos \varphi + p_{Sy} \cos \theta \sin \varphi - p_{Sz} \sin \theta|^2 \right\} \delta \left(E_S(0) - \frac{\hbar c Q}{\sqrt{\epsilon}} \right)
$$

$$
= \frac{\pi e^2}{\epsilon_0 m^2 V c \sqrt{\epsilon}} \int d\varphi \, d\theta \, \sin \theta \int dQ \, Q \left\{ |p_{Sx}|^2 \sin^2 \varphi + |p_{Sy}|^2 \cos^2 \varphi \right.
$$

$$
\left. + |p_{Sx}|^2 \cos^2 \theta \cos^2 \varphi + |p_{Sy}|^2 \cos^2 \theta \sin^2 \varphi + |p_{Sz}|^2 \sin^2 \theta \right\} \delta \left(E_S(0) - \frac{\hbar c Q}{\sqrt{\epsilon}} \right)
$$

$$
= \frac{8\pi^2 e^2 p_S^2}{3\epsilon_0 m^2 V c \sqrt{\epsilon}} \int dQ \, Q \cdot \delta \left(E_S(0) - \frac{\hbar c Q}{\sqrt{\epsilon}} \right) = \frac{8\pi^2 \sqrt{\epsilon} e^2 p_S^2 E_S(0)}{3\epsilon_0 \hbar^2 c^3 m^2 V}. \tag{B.3}
$$

After dividing the numerator by the denominator, we obtain

$$
\langle \gamma_S^{\text{3D, iso}} \rangle(T) = \frac{8\sqrt{\pi \epsilon} \, e^2 \, \hbar \, p_S^2}{3 \, \epsilon_0 m^2 V E_S(0)^2} \left(\frac{E_S(0)^2}{2 M_S c^2 k_B T} \right)^{3/2} \tag{B.4}
$$

namely the finite temperature radiative lifetime in Eq. (3.23).

$$A\ p\ p\ e\ n\ d\ i\ x\quad C$$

DERIVATION OF THE RADIATIVE LIFETIME IN ANISOTROPIC 3D MATERIALS

Here we provide the derivation of the radiative recombination rate in anisotropic 3D materials, given in Eq. (4.7). In the anisotropic case, the dielectric constant is given by Eq. (4.2) and the photon polarizations and frequencies are given by Eqs. (4.3) - (4.5). We obtain the radiative rate by substituting the photon solutions into Eq. (3.11), and, as in the bulk isotropic case, momentum conservation fixes the emitted photon wavevector to $\mathbf{q} = \mathbf{Q}$, and the summation over λ adds together the contributions from the IP and OOP solutions, resulting in the radiative rate at zero temperature given in Eq. (4.6). To obtain the radiative rate at finite temperature T, we plug Eq. (4.6) into Eq. (3.12) with the dispersion relation in Eq. (4.1). Similar to the isotropic case, the denominator is given by a Gaussian integral and gives

$$\int dQ_x dQ_y dQ_z e^{\frac{-\hbar^2}{2}\left(\frac{Q_x^2+Q_y^2}{M_{xy}}+\frac{Q_z^2}{M_z}\right)} = \left(\frac{2\pi\sqrt[3]{M_{xy}^2 M_z}k_B T}{\hbar^2}\right)^{3/2} \tag{C.1}$$

where we leave out the factor $e^{-E_S(0)/k_B T}$, which is present both in the numerator and denominator and cancels out in the final result. For the numerators we again note that the exciton parabolic dispersion can be approximated as flat within the light cone such that $E_S(\mathbf{Q}) \approx E_S(0)$. As a result, the final expression for the IP term in the numerator we have:

$$\frac{\pi^2 e^2 (p_{Sx}^2 + p_{Sy}^2) E_S(0)\sqrt{\epsilon_{xy}}}{\epsilon_0 m^2 V c^3 \hbar^2} \int_{-1}^{1} d\cos\theta \exp\left[-\left(\frac{\cos^2\theta}{2M_{xy}} + \frac{\sin^2\theta}{2M_z}\right)\frac{\epsilon_{xy}E_S(0)^2}{k_B T c^2}\right] \tag{C.2}$$

For the OOP term of the numberator, we define a change of variables:

$$k_x = \sqrt{\epsilon_{xy}}Q_x, \quad k_y = \sqrt{\epsilon_{xy}}Q_y, \quad k_z = \sqrt{\epsilon_z}Q_z \tag{C.3}$$

such that the delta function will be simplified into a form with only radius dependence. Thus the integral becomes:

$$\frac{\pi e^2}{m^2 V} \int \frac{k^2 dk \sin\theta d\theta d\phi}{\epsilon_0 \epsilon_{xy}\sqrt{\epsilon_z}} \exp\left[E_S(0) + \hbar^2 k^2 \left(\frac{\epsilon_{xy}\sin^2\theta}{2M_{xy}} + \frac{\epsilon_z \cos^2\theta}{2M_z}\right)\right]$$

$$\times \frac{\sqrt{\epsilon_{xy}\epsilon_z}}{ck} \left|(p_{Sx}\cos\phi + p_{Sy}\sin\phi)\sqrt{\frac{1/\epsilon_{xy}}{1+\tan^2\theta}} - p_{Sz}\sqrt{\frac{1/\epsilon_z}{1+\cot^2\theta}}\right|^2_{OOP} \delta\left(E_S(0) - \frac{\hbar ck}{\sqrt{\epsilon_{xy}\epsilon_z}}\right)$$

$$(C.4)$$

The final analytic expression is:

$$\frac{\pi^2 e^2 E_S(0)\epsilon_z \sqrt{\epsilon_{xy}}}{\epsilon_0 m^2 V c^3 \hbar^2} \int_{-1}^{1} d\cos\theta \left[\frac{p_{Sx}^2 + p_{Sy}^2}{\epsilon_{xy}}\cos^2\theta + \frac{2p_{Sz}^2}{\epsilon_z}\sin^2\theta\right]$$

$$\times \exp\left[-\left(\frac{\epsilon_{xy}\cos^2\theta}{2M_{xy}} + \frac{\epsilon_z \sin^2\theta}{2M_z}\right)\frac{\epsilon_z \epsilon_{xy} E_S(0)^2}{k_B T c^2}\right] \quad (C.5)$$

Eq. (C.2) and Eq. (C.5) both have the form of an error function which can be computed numerically for a given temperature T. However, since $E_S(0)^2 \ll k_B T M_S c^2$, we can take the lowest order in T and thus obtain:

$$\left\langle \gamma_S^{\text{3D,aniso}} \right\rangle (T) = \frac{\sqrt{\pi\epsilon_{xy}}e^2\hbar\left[\left(\frac{2\epsilon_z}{3\epsilon_{xy}} + 2\right)\left(p_{Sx}^2 + p_{Sy}^2\right) + \frac{8}{3}p_{Sz}^2\right]}{\epsilon_0 m^2 V E_S(0)^2}$$

$$\times \left(\frac{E_S(0)^2}{2\sqrt[3]{M_{xy}^2 M_z}c^2 k_B T}\right)^{3/2} \quad (C.6)$$

This is the finite temperature radiative rate for an anisotropic bulk crystal in Eq. (4.7).

A p p e n d i x   D

DERIVATION OF THE RADIATIVE LIFETIME IN 0D SYSTEMS

We provide additional details for the derivation of the radiative recombination rate in 0D systems, Eq. (3.30). As discussed above, in the 0D case there is no constraint from momentum conservation on the emitted photon wavevector. Therefore, we replace the summation in Eq. (3.11) by an integration over the full momentum space and write

$$\gamma_S^{0D} = \frac{\pi e^2}{\epsilon_0 m^2} \sum_\lambda \int \frac{d\Omega \, dq \, q^2}{(2\pi)^3} \frac{|\mathbf{e}_{\lambda\mathbf{q}} \cdot \mathbf{p}_S(\mathbf{Q})|^2}{\omega_{\lambda\mathbf{q}}} \delta\left(E_S - \hbar\omega_{\lambda\mathbf{q}}\right) \qquad (D.1)$$

which comes from rewriting the summation along each cartesian component α as $\sum_{q_\alpha} = \int L_\alpha dq_\alpha/2\pi$, and $L_x L_y L_z = V$. In the 0D case, we can apply the photon quantization solutions used in the 3D case, so that $\lambda = \text{IP}$ or OOP, and $\mathbf{e}_{\lambda\mathbf{q}}$ are in the form of Eq. (3.21) with $\omega_{\lambda\mathbf{q}} = c|\mathbf{q}|/\sqrt{\epsilon}$. Note that this approach applies both to isolated emitters, such as quantum dots and molecules, as well as to atoms, ions or other single quantum emitters embedded in an isotropic material. Combining these results, we can write

$$\gamma_S^{0D} = \frac{\pi e^2}{8\epsilon_0 m^2 \pi^3 c\sqrt{\epsilon}} \times$$
$$\int d\varphi \, d\theta \sin\theta \int dq \, q \left\{ |-p_{Sx}\sin\varphi + p_{Sy}\cos\varphi|^2 \right.$$
$$\left. + |p_{Sx}\cos\theta\cos\varphi + p_{Sy}\cos\theta\sin\varphi - p_{Sz}\sin\theta|^2 \right\}$$
$$\times \delta\left(E_S - \frac{\hbar cq}{\sqrt{\epsilon}}\right)$$
$$(D.2)$$

and finally obtain Eq. (3.30),

$$\gamma_S^{0D} = \frac{\sqrt{\epsilon}e^2 p_S^2 E_S}{3\pi\epsilon_0 m^2 c^3 \hbar^2}. \qquad (D.3)$$

A p p e n d i x   E

RADIATIVE LIFETIMES OF EXCITONS WITH NON-ANALYTIC DISPERSIONS

In this section, we provide an additional discussion for exciton with non-analytic dispersion:

$$E_S(\mathbf{Q}) = E_S(0) + B|\mathbf{Q}|. \tag{E.1}$$

The radiative lifetimes at finite temperature in this case still follow Eq. (3.12). When the lowest order dependence of temperature is considered, using different exciton dispersion only changes the phase space integral, *i.e.* the denominator in Eq. (3.12), compared to the derivation for parabolic dispersion. This integral in different dimension can be summarized within a single formula, written as:

$$I(n) = \int d\Omega_n \int dQ Q^{n-1} \exp\left[\frac{-BQ}{k_B T}\right] \tag{E.2}$$

where n is the dimension of the material and Ω_n is the $n-$dimensional differential solid angle, while

$$I(n) = \begin{cases} 8\pi(k_B T/B)^3 & n = 3 \\ 2\pi(k_B T/B)^2 & n = 2 \\ 2(k_B T/B) & n = 1 \end{cases} . \tag{E.3}$$

As a result, we obtain the radiative lifetimes of excitons in isotropic 3-, 2- and 1-dimensional materials:

$$\langle \gamma_S^{\text{nD,iso}} \rangle_{\text{non-ana}}(T) = \begin{cases} \frac{\pi\sqrt{\epsilon}e^2 \hbar p_S^2}{3\epsilon_0 m^2 V E_S(0)^2} \left(\frac{BE_S(0)}{ck_B\hbar T}\right)^3 & n = 3 \\ \gamma_S^{\text{2D}}(0) \times \frac{2}{3}\left(\frac{BE_S(0)}{ck_B\hbar T}\right)^2 & n = 2 \\ \gamma_S^{\text{1D}}(0) \times \frac{2}{3}\frac{BE_S(0)}{ck_B\hbar T} & n = 1 \end{cases} . \tag{E.4}$$

where $\gamma_S^{\text{2D}}(0)$ and $\gamma_S^{\text{1D}}(0)$ are intrinsic radiative rate in 2D and 1D system respectively defined in the main text which are independent from the dispersion relation. Compared to the lifetime of exciton with parabolic dispersion, the lifetimes of exciton with non-analytic dispersion have stronger temperature dependence. $\langle \gamma_S^{\text{nD,iso}} \rangle_{\text{non-ana}}(T) \propto T^n$ while $\langle \gamma_S^{\text{nD,iso}} \rangle_{\text{parabolic}}(T) \propto T^{n/2}$.